UNIVERSITY OF COPENHAGEN
FACULTY OF SCIENCE

PhD Thesis

Beyond Single Molecules: The Importance of Accurate Modeling for Molecular Junctions

Louise Oxen Høgh Hyllested

Academic advisor: Gemma C. Solomon
Submitted on: January 2025

This thesis has been submitted to the PhD School of The Faculty of Science, University of Copenhagen

Careful. We don't want to learn from this.

— Bill Watterson, "Calvin and Hobbes"

ABSTRACT

Molecular electronics is transforming our understanding of electronic devices by offering a promising alternative to traditional silicon-based technologies. It has the potential to overcome the size limitations of current approaches by utilizing the unique properties of molecules. Understanding these properties is crucial to design and develop molecular-scale components that can function reliably in electronic circuits. The most reliable use of molecules involves using ensembles of molecules. However, molecules are complex and can interact with one another, affecting the properties observed in measurements. By using computational methods and incorporating molecules into an electrode–molecule–electrode junction while increasing the number of molecules in the junction, we can observe how molecular interactions influence molecular properties. However, understanding the effect of molecular interactions is only one part of the challenge. To achieve the goal of using molecules in electronics, the impact of electrode choice must also be considered. In molecular electronics, electrodes can be made from different materials, making the careful selection of electrodes in both experiments and computations crucial. Here, we show that when simulating molecules in junctions, intermolecular interactions and the choice of top electrodes significantly influence the observed molecular properties. These findings emphasize the need for accurate modeling of molecular junctions to effectively use computational methods for understanding molecular properties.

RESUME

Molekylær elektronik ændrer vores forståelse af elektroniske enheder ved at introducere et lovende alternativ til traditionelle siliciumbaserede teknologier. Denne tilgang har potentiale til at overvinde størrelsesbegrænsningerne ved de nuværende metoder ved at udnytte molekylers unikke egenskaber. Forståelse af disse egenskaber er afgørende for at designe og udvikle komponenter på molekylært niveau, der kan fungere pålideligt i elektroniske kredsløb. Den mest pålidelige anvendelse af molekyler indebærer brug af grupper af molekyler. Dog er molekyler komplekse og kan interagere med hinanden, hvilket påvirker de egenskaber, der observeres i målinger. Ved at bruge beregningsmetoder og inkorporere molekyler i en elektrode-molekyle-elektrode-forbindelse, mens antallet af molekyler i forbindelsen øges, kan vi observere, hvordan molekylære interaktioner påvirker de molekylære egenskaber. Forståelsen af molekylære interaktioner er dog kun en del af udfordringen. For at opnå målet om at anvende molekyler i elektronik skal valget af elektroder også overvejes. I molekylær elektronik kan elektroder fremstilles af forskellige materialer, hvilket gør valget af elektroder afgørende i både eksperimenter og beregninger. Her viser vi, at når molekyler simuleres i en elektrode-molekyle-elektrode-forbindelse, påvirker intermolekylære interaktioner og valget af elektroder i betydelig grad de observerede molekylære egenskaber. Disse resultater understreger behovet for nøjagtig modellering af molekylære forbindelser for effektivt at anvende beregningsmetoder til at forstå molekylære egenskaber.

LIST OF PUBLICATIONS

[P1] L. O. H. Hyllested, I. Prestholm, and G. C. Solomon. "Intermolecular Interactions and Quantum Interference Effects in Molecular Junctions." In: *ACS Nanoscience Au* 4.6 (2024), pp. 426–434. DOI: 10.1021/acsnanoscienceau.4c00041. URL: https://doi.org/10.1021/acsnanoscienceau.4c00041.

[P2] S. Soni et al. "Frontier Orbital Gating of Rectification and Conductance in Tunneling Junctions Comprising Pyridine-terminated Molec- ular Wires." *In preparation.*

THESIS STATEMENT

This thesis is based on the following manuscripts:

Chapter 3 is based on the following published article:

• L. O. H. Hyllested, I. Prestholm, and G. C. Solomon. "Intermolecular Interactions and Quantum Interference Effects in Molecular Junctions." In: ACS Nanoscience Au 4.6 (2024), pp. 426–434. doi: 10.1021/acsnanoscienceau.4c00041.

Chapter 4 is based on the following article in preparation:

• S. Soni, L. O. H. Hyllested, S. Kumar, M. Carlotti, J. Kardula, A. G. M. Uiterwijk, R. W. A. Havenith, Olle Hellman, María Camarasa Gómez, Leeor Kronik, G. C. Solomon, and R. C. Chiechi. "Frontier Orbital Gating of Rectification and Conductance in Tunneling Junctions Comprising Pyridine-terminated Molecular Wires." In preparation.

ACKNOWLEDGEMENTS

First, I would like to thank my supervisor, Professor Gemma Solomon, for welcoming me into her group during my bachelor's studies, encouraging me to explore the experimental side of science in my master's, and finally, for giving me the incredible opportunity to pursue a PhD. I am deeply grateful for your belief in me throughout this journey.

I would also like to thank the Solomon and Hansen group members. It has been a pleasure working with all of you, and I truly appreciate the office discussions, support, and help you've provided along the way. I am especially grateful to Susanne and Lea for the great discussions and proofreading of my thesis—your help has been invaluable in completing this work.

A special thanks goes to the coffee team, Emil and Patrick. Even though you left me behind, you still helped me get off to a good start in the PhD life. If you could do it, then of course I can too!

Thank you to my family and friends for being there for me, offering support and encouragement throughout my PhD journey. Your belief in me, patience, and understanding have made all the difference, and I couldn't have made it through without you. A special thanks to Louise Nikolajsen for taking the time to proofread my work, even though it lies far outside her own field.

Lastly, and probably my biggest acknowledgement, is to you, Lasse Nikolajsen. You have given me the will to pursue this PhD, even though I knew it would be hard. You always know that I can do anything, even when I am sure I will fail. For that, I am forever thankful. Thank you for being the rock in my life, and thank you for Emma. She is the perfect break and the biggest gift I could get.

Copenhagen, January 2025,

Louise Oxen Høgh Hyllested

CONTENTS

1

MOTIVATION

Molecular electronics has long been of interest because it offers a new method for building electronic devices. Most electronics today are silicon-based and follow a top-down approach, where a substrate is taken and material is added or removed from the surface to create components. However, some believe we are reaching a limit in how much we can reduce the size of electronics with this approach.[1] Molecular electronics has been proposed as the next step in creating smaller and better-performing components by using a bottom-up approach, building devices from the molecular level upwards. [2, 3]

If successful, this could lead to devices with improved performance and lower power consumption, enabling the development of more powerful and efficient electronic technologies.[4, 5] Another key advantage of using molecules instead of traditional semiconductor materials is sustainability. Organic molecules, which are often used in molecular electronics, can be designed and modeled to be more environmentally friendly.[6] This is a significant benefit if we aim to reduce the environmental impact associated with the production and disposal of electronic devices today. Additionally, some molecules possess unique functionalities that standard materials lack. These include properties like switching capabilities[7, 8], sensing[9, 10], or insulators[11, 12], which can be incorporated into electronics.

To achieve this, we must first understand the fundamental properties of molecules. In molecular electronics, molecules serve as active elements in circuits, functioning as wires[13], switches[14], or transistors[15]. Therefore, understanding their behavior is crucial. The most promising approach to integrating molecules into electronics involves using ensembles of molecules. While the properties of individual molecules have been

thoroughly studied, our understanding of intermolecular effects—how molecules interact and influence one another—remains incomplete.

However, understanding the molecules themselves is only part of the challenge. Another important factor to consider is the choice of electrodes. In molecular electronics, a molecule is typically connected to two electrodes. If the ultimate goal is to incorporate organic molecules into electronic circuits with different materials like silicon, graphene, or gold, it is essential not to overlook the influence of the electrodes or substrate on the molecular properties.

This thesis aims to demonstrate how molecular interactions and electrode choice influence molecular properties, emphasizing the importance of considering these factors when using computational methods to screen molecules for potential applications in molecular electronics. The discussion begins in Chapter 2 with a brief overview of the state-of-the-art computational methods used in the presented papers, along with a short introduction to some fundamental molecular properties. Chapter 3 focuses on the effects of intermolecular interactions, highlighting key results from Paper 1. Chapter 4 explores the impact of electrode choice, drawing on findings from Paper 2. Chapter 5 reflects on the projects that, despite considerable progress, did not reach their intended outcomes or contribute directly to the final results of this work. Finally, the main points from Chapters 3 and 4 are brought together in a conclusion, accompanied by an outlook on future directions.

2

MOLECULAR ELECTRONICS COMPUTATIONS

Without diving too deeply into the history of computational chemistry and its evolution—though it is a long and fascinating one—this chapter aims to give a brief introduction to the state-of-the-art theories used in Paper 1 and Paper 2. It explains how they have been applied in the following chapters and highlights their limitations. It is important to note that many different methods are available in this field, and only a few are discussed in this chapter.

2.1 INTRODUCTION

Before computing power and theory reached the level we have today, it was not straightforward to use theory and calculations to investigate molecules. One of the simpler theories that came first was the Hückel theory, also known as the tight-binding model. This model calculates the electronic structure of primarily conjugated molecules. Since it focuses only on the pi-electrons of the molecule, and conjugated molecules have pi-electrons as their dominant electronic property, its applications are somewhat limited. Additionally, the model simplifies the molecular system by neglecting interactions between non-neighboring atoms and assuming a uniform overlap of atomic orbitals. Despite these limitations, the model is still used today as a simple tool for preliminary calculations of larger and more complex systems.

Later came density functional theory (DFT).[16] Instead of using the wavefunction of all electrons and solving complex, time-consuming calculations, DFT uses the electronic density. This simplified the calculations somewhat and made it possible to investigate larger and more complex systems.

With DFT establised, the NEGF (Non equilibrium Green's function) and the Landauer formalism followed, paving the way for calculating the transport properties and current of molecules in junctions.[17] As these theories became well established, various software programs, such as QuantumATK, Gaussian, and Siesta, emerged, making molecular calculations more user-friendly and accessible to a broader range of scientists. In the papers discussed in this thesis, DFT, together with NEGF and the Landauer formalism, has been used for all calculations, with QuantumATK as the primary software.[18, 19]

2.2 CHALLENGES WITH DENSITY FUNCTIONAL THEORY

Even though DFT has expanded the range of systems that can be calculated, it has not come without limitations. One of the biggest challenges in DFT is the approximation of the exchange-correlation (XC) functional, which governs how electron interactions are approximated. The better the functional, the more accurately the total energy of the system is approximated. Different functionals exist, each covering more or fewer aspects of these interactions.

The simplest functional is the Local Density Approximation (LDA)[16], which depends only on the electron density at each point in space. The next improvement over the LDA functional is the Generalized Gradient Approximation (GGA). This functional enhances the LDA by incorporating the gradient of the electron density, allowing it to better capture variations in density across a molecule or material. One of the more popular GGA-based functionals is the Perdew-Burke-Ernzerhof (PBE) functional.[20] It works well for predicting the structural and electronic properties of molecules and materials.

More advanced XC functionals have been developed, such as Hybrid Functionals and Meta-GGA, though these also increase computational cost. Every time we increase complexity, the computational cost rises, so it becomes a trade-off between what the more complex functional captures compared to a simpler functional.

In this thesis, the calculations were carried out using GGA-PBE with a double-zeta polarized basis set and the Grimme DFT-D3[21] dispersion correction. This choice was made to minimize computational cost while still capturing the relevant interactions. The basis set is used to approximate atomic and molecular orbitals (which will be explained later). The decision to use a double-zeta basis set over single-zeta was primarily to achieve higher accuracy when covering more complex systems, at the expense of increased computational cost. Dispersion forces are weak, long-range interactions between atoms and molecules, that play an important role in non-covalent bonding. The Grimme DFT-D3 is a dispersion correction that includes van der Waals forces, which are otherwise underestimated in standard DFT.

There are several other limitations to DFT. To mention a few, it underestimates the HOMO-LUMO gap,[22] suffers from a self-interaction error where the electron interacts with the entire electron density resulting in the electron interacting with its own density,[23] and does not scale well with larger systems.[24] This makes it challenging to balance the use of more expensive functionals and basis set choices.

Even though DFT can be used to calculate larger systems compared to Hückel, the approximations and limitations presented above constrain its applicability and the accuracy of the calculations. These limitations should not discourage us from using DFT; rather, we need to interpret the results accordingly, focusing on qualitative insight rather than quantitative values and emphasizing trends rather than exact results. We must accept that, unless we use enormous amounts of computational power, there will always be limits to our theoretical calculations.

2.3 TRANSMISSION AND CURRENT

With the theory established, we now dive into the NEGF approach and the Landauer formula, which are used to calculate the transmission and current of molecular junctions. The NEGF is a method used to study electron flow (quantum transport) in molecular systems consisting of a molecule connected to two electrodes. An illustration of a molecular system is shown in Figure 2.1. In this kind of system, the electrodes act as a reservoirs of electrons, and through this as source and drain for the current.

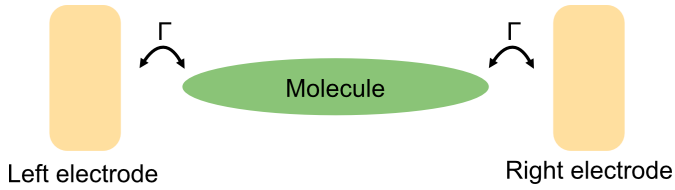

Figure 2.1: Illustration of a molecular system consisting of two electrodes with a molecule in between, where Γ is the coupling strength between the molecule and each electrode.

To calculate the transmission, we first need to understand how electrons propagate through a molecular system. This is described by the Green's function, G, as shown below.

$$G(\varepsilon) = [\varepsilon \mathbf{I} - \mathbf{H} + \frac{i}{2}\mathbf{\Sigma}^{L} + \frac{i}{2}\mathbf{\Sigma}^{R}]^{-1}. \tag{2.1}$$

Here, I is the identity matrix and H is the Hamiltonian of the central region alone as illustrated as the molecule between the two electrodes in Figure 2.1. This hamiltonian is typically obtained from DFT. Σ is the self-energy of the left and right electrodes and accounts for the interaction between the electrodes and the central region with interation to the electrode.

Once the Green's function is calculated it can be used to calculate the transmission function, that represents the likelihood of electron transport at different energies.

$$T(\varepsilon) = \mathrm{Tr}\{\mathbf{\Gamma}^L \mathbf{G}(\varepsilon)\mathbf{\Gamma}^R \mathbf{G}^\dagger(\varepsilon)\}. \tag{2.2}$$

Here, Γ is the broadening matrix, related to the imaginary part of the self-energy, and captures the coupling to the left and right electrodes, as illustrated in Figure 2.1 by the arrows on each side of the molecule. The term G denotes the Green's function from Equation 2.1. Equation 2.2 illustrate the probability of an electron going from one electrode across the molecule to the other electrode at a certain energy ϵ. By varying the energy (ϵ) we can get a spectrum with energy on the x-axis and transmission probability on the y-axis. An example of this are shown in Figure 2.2.

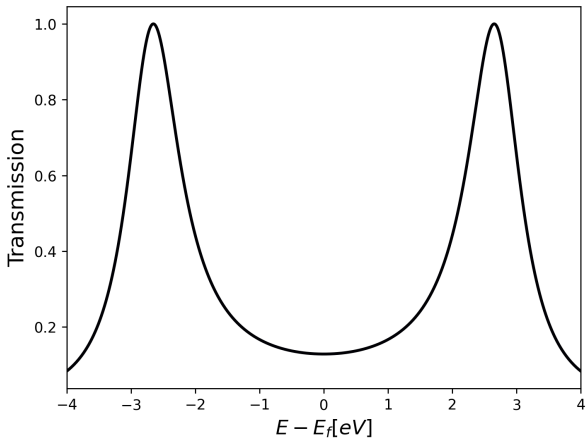

Figure 2.2: Example of a transmission spectrum, with transmission probability on the y-axis and energy (E-Ef (eV)) on the x-axis.

As shown in Figure 2.2, two peaks are present at approximately -2.5 eV and +2.5 eV. These correspond to the energies of the highest occupied molecular orbital (HOMO) at -2.5 eV and the lowest unocupied molecular orbital (LUMO) at +2.5 eV. As the names suggest, the HOMO is the molecular orbital containing electrons that can contribute to transport,

while the LUMO is the molecular orbital capable of transmitting incoming electrons.

The HOMO and LUMO, also known as the frontier orbitals, are located on either side of the Fermi level at 0 eV. The Fermi level represents the energy level that separates occupied and unoccupied electronic states in the electrodes. To illustrate why this is important, an example of the single-level model for electron transport is shown in Figure 2.3.

In this model, the energy levels of the molecule are positioned between the two electrodes (left and right). The HOMO lies below the Fermi level, while the LUMO lies above it. The red line in the figure illustrates the transmission spectrum from Figure 2.2 rotated 90 degrees. Based on the figure, we would expect little to no electron transmission at this configuration. The closer the Fermi level is to either the HOMO or the LUMO, the greater the transmission we would expect. The energy difference between the frontier orbitals and the Fermi level represents the energy barrier that must be overcome when the Fermi level does not align with the frontier orbitals.

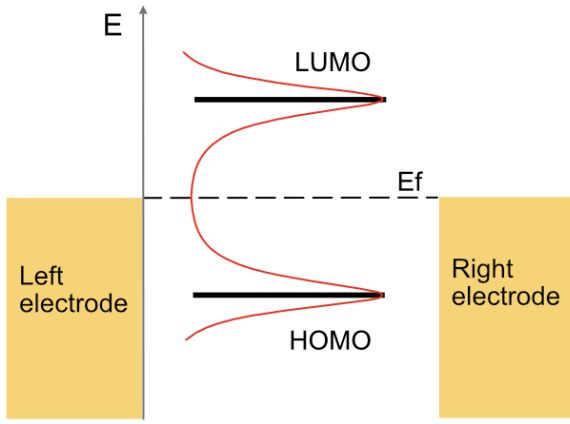

Figure 2.3: Schematic of the single-level model for electron transport at zero bias. The left and right electrodes share the same chemical potential. Ef corresponds to the Fermi level, and E represents the energy scale. The red graph shows the transmission spectrum, while the two black lines indicate the HOMO and LUMO levels.

The width of each peak in the transmission spectrum is correlated to the coupling strength (Γ) between the molecule and the electrodes. If there is direct overlap with one of the frontier orbitals and a strong coupling to the electrodes, resonant transport occurs. In this scenario, electrons can move through the orbital as a conduction channel.

However, this situation is often not the case for molecular junctions. Instead, the coupling strength to the electrodes can vary depending on how the molecule binds to the electrode. In such cases, we observe off-resonant tunneling transport. Here, the electron must overcome or tunnel through the energy barrier created by the difference between the frontier orbital energy and the Fermi level. This mechanism leads to the lower transmission observed between the two peaks in Figure 2.2.

Everything up untill now has been at zero bias. Once we add a bias across the junction, we can calculate the current. As mentioned previously, the current can be calculated using the Landauer formula.

$$I = \frac{2e}{h} \int_{-\infty}^{\infty} d\varepsilon \, [f_L - f_R] T(\varepsilon), \tag{2.3}$$

The formula calculates the current by integrating the tranmission function weighted by the difference in the Fermi-Dirac distributions of the left and right electrodes(f_L and f_R, respectively).

$$f_{(L/R)}(\varepsilon) = \frac{1}{exp(\frac{\varepsilon - \mu_{(L/R)}}{k_B T_{(L/R)}}) + 1}, \tag{2.4}$$

Here, k_B is the boltzman distribution and T is the absolut temperature. The Fermi-Dirac distribution is a distribution of electrons in the electrode at a given chemical potential and temperature. If the system is in equilibrium i.e. at no applied bias, the Fermi level and the chemical potential are the same. By changing the applied bias voltage across the junction, the chemical potentials/Fermi level of each individual electrode are shifted. This shift of the chemical potentials is what is driving the current. To illustrate this, the single level model with an applied bias is shown in Figure 2.4. In contrast to figure 2.3 the left electrode is shifted upwards.

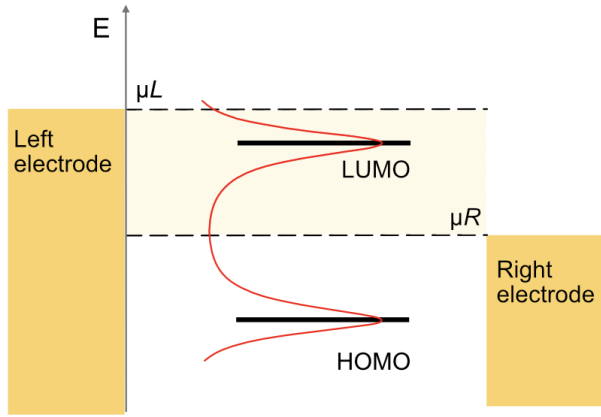

Figure 2.4: Schematic of the single-level model for electron transport at finite bias. The left and right electrodes have different chemical potential. E represents the energy scale and the red graph shows the transmission spectrum, while the two black lines indicate the HOMO and LUMO levels. The yellow shaded area between the chemical potential of the electrode correponds to the bias window.

This shift results in the opening of a bias window, represented by the shaded area between the two electrodes. Within this window, current can flow because there are occupied states in the left electrode and unoccupied states in the right electrode. In this example, the LUMO peak lies inside the bias window. As mentioned earlier, aligning the Fermi level with the frontier orbitals results in higher transmission. The same principle applies to current, as the Landauer formula integrates the transmission spectrum over the range of the bias window. It is important to note that this is a simplified model, intended solely to illustrate the basic concepts of electron transport.

The reason for the interest in what happens around the Fermi level is that this is what we can expect to observe in experiments. Since the HOMO and LUMO often play a central role in electron transport, other molecular states do not contribute significantly to physical processes. This is because the Fermi level separates the filled and unfilled states in the electrodes, so states below the HOMO do not participate as they cannot easily be excited or moved. Experiments primarily probe electrons

that actively participate in physical processes, and these are mainly the electrons near the Fermi energy.

2.4 MOLECULAR PROPERTIES

With the theoretical methods now established, we move on to the molecular properties. As mentioned earlier, molecules can possess many different properties. In Paper 1 and Paper 2, the two properties in focus are Destructive quantum interference (DQI) and rectification. To understand these properties, we first need to explore some general principles of molecules. For example, considering water (H_2O), which consists of two hydrogen (H) atoms and one oxygen (O) atom. Each atom has an atomic orbital (AO), which describes the most probable locations of its electrons. When atoms combine to form a molecule, such as water, the atomic orbitals of the individual atoms merge to form a molecular orbital (MO). These MOs describe the behavior and distribution of electrons across the entire molecule rather than being confined to a single atom. In the case of water, there would be more molecular orbtial on the oxygen since this has more electrons available for making bonds.

An interesting thing about molecules is that we can tailor them to our interest. Most molecules can be synthezied as long as some basic chemical rules are fufilled. One type of molecules is known as conjugated molecules. This simply means that they have alternating single and double(triple) bonds. This results in a delocalized pi-electron system, that makes them more stable than a their non-conjugated counterparts. Taking this one step further, they can be either linear or cross - conjugated. In Figure 2.5 three examples of conjugated molecules are shown. Butadiene and benzene are linearly conjugated, with the alternating double and single bonds. Benzophenone, on the other hand, is cross conjugated. This happens when two conjugated systems, like the benzene rings, are connected by a group, here a carbonyl group (C=O), that can participate in the conjugation of each ring, whereas the two benzene rings are not a part of the same conjugated system due to the two single bonds separating the benzene rings. In this case the pi-electrons are delocalized

to one of the rings and the carbonyl group at a time, and not spreading across the entire molecule as butadiene and benzene. This results in a "broken" channel/system that can make it more difficult for an electron to go across the molecule.

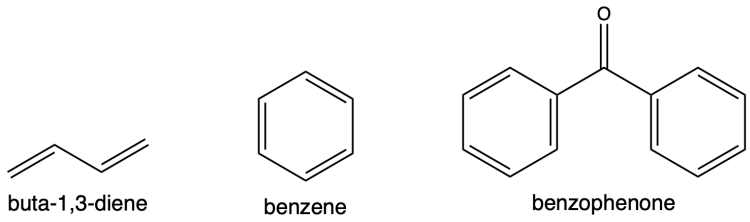

Figure 2.5: Molecular structures of two linear conjugated molecules, butadiene and benzene, and one cross-conjugated molecule, benzophenone.

What has been described until now in this section has been intramolecular, meaning that it occurs within a single molecule. However, molecules can experience both intramolecular (interactions in the molecule iself) and intermolecular (molecule-to-molecule) interactions. Various types of interactions can occur between molecules, as well as within molecules. These include Van der Waals forces, such as dipole-dipole interactions, where the dipole of one molecule aligns with the opposite dipole of another. Another example is hydrogen bonding, where a hydrogen atom in one molecule binds non-covalently to an electronegative atom, such as oxygen, in another molecule. In general, it is not easy to determine which specific type of interaction is influencing a molecular system. Different types of interactions can overlap and affect the system simultaneously, making it difficult, or even impossible, to distinguish them.

2.4.1 *Destructive Quantum Interference*

To understand destructive quantum interference it is useful to first understand electrons. Electrons exhibit wave-particle duality, meaning they can behave like particles and waves.[25] This can be explained by the double slit experiment for electrons that Richard Feynman explained in his lecture in 1965.[26] In Figure 2.6 an illustration of the double slit

experiment is shown. On the leftmost side is an electron gun, in the

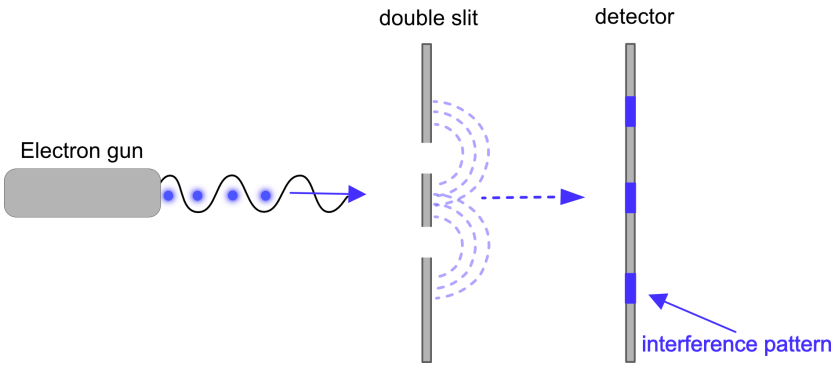

Figure 2.6: Illustration of the double-slit experiment for electrons. On the left is the electron gun, which emits electrons toward a wall with two slits. On the right is the detector, displaying the interference pattern observed when electrons pass through the double-slit wall.

middle is a wall with two slits, and on the rightmost side is a detector that indicates when an electron hits. First, we can think of electrons as bullets. If we were to shoot bullets toward a detector, we would expect them to travel in a straight line and hit the detector. If we then added a wall with two slits between the gun and the detector, only bullets fired in specific directions would pass through the slits, resulting in a normal distribution in front of each slit. The total number of bullets hitting the detector would then be the sum of the two distributions.

If we instead think of electrons as waves, similar to water waves, and send a wave toward the wall with the two slits, the wave would travel through the slits and continue as two waves, one emerging from each slit, on the other side of the wall. When the two waves interfere, they can either interfere constructively, amplifying each other, or interfere destructively, where the crest of one wave meets the trough of another and cancels out, leaving the surface flat. This interference results in a pattern observed at the detector instead of a single distribution.

The interesting thing about electrons is that when there is no wall in the middle, the detector records a single spot where the electron hits, just like a bullet i.e. a particle behavior. With one slit open, a normal distribution is observed. However, when both slits are open, an

interference pattern appears, similar to what we observe with waves. This phenomenon demonstrates wave-particle duality. Richard Feynman famously illustrated this concept, and several experiments have since confirmed this behavior.[27–30]

This is important when we look at electron transport in molecular junctions, where the movement of electrons generates the current. This movement resembles wave behavior. When electron waves interfere constructively, they amplify each other, leading to enhanced transmission. In contrast, when electron waves interfere destructively and cancel each other out, the transmission is reduced or even entirely canceled. This phenomenon is known as DQI. This can (as an example) happen if a molecule has multiple pathways for electron transport and the phases of the electron waves traveling along different paths interfere destructively.[31] Another example is cross conjugated molecules. These have been found to possess destructive quantum interference, resulting in very low transmission and current.[32, 33]

2.4.2 *Rectification*

In a regular electric circuit a rectifier is a device that converts alternating current (AC) into direct current (DC), meaning that they only allow current to flow in one direction. One example of this is a diode. These are often used in the converters we use in the charger for different electronics devices, since these need DC.

The first step towards molecular recitfiers was made by Aviram and Ratner that proposed that a single molecule could act as a rectifier if it had a specific structure, namely a donor-bridge-acceptor system.[34] In the following years different molecules with different recitifying mechainsms have been ivestigated showing this property of blocking current in one direction and conduncting current in the other. [35–37]

A way to recognize a rectifying molecule in a junction is to calculate (or measure) the current across the junction at forward (postive voltage) and reverse (negtaive voltage) bias. Here the Landauer formula comes in handy. As explained earlier the Landauer formula can be used to

calculate the current at different bias. By choosing a range of bias points we can calculate the current and plot it as a function of Voltage. This results in an current vs voltage (IV) curve as the ones illustrated in Figure 2.7. Here, the blue curve illustrates a molecule with no special

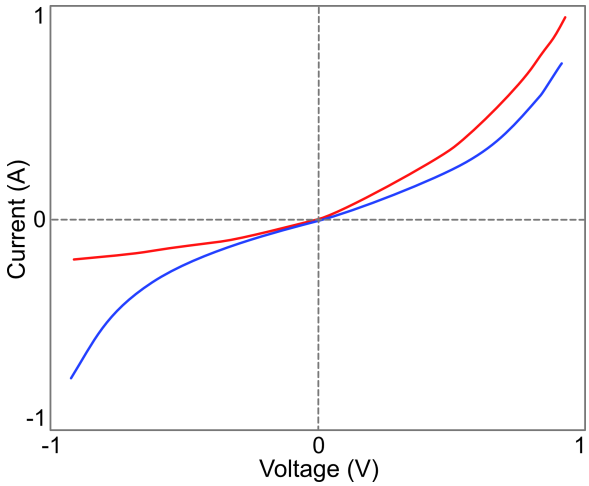

Figure 2.7: Example of two IV curves representing a non-recitifiying molecule (blue) and a recitifying molecule (red), with voltage (V) on the x-axis and Current (A) on the y-axis.

properties between two electrodes. This curve is symmetric, we have the same amount of current at negative and positive voltage. The red curve instead illustrates a molecule that is rectifying. Here, we observe more current at positive voltage than at negative voltage, resulting in an assymmetric curve and therefore a rectification towards positive bias. From an IV curve it can be difficult to determine the amount of recitification, therefore the rectification ratio are often calculated as the difference between the forward current and the reverse current at each bias.

3

THE EFFECT OF INTERMOLECULAR INTERACTIONS

This chapter aims to explain how the results from Paper 1 illustrate the importance of simulating molecular interactions in molecular junctions. It demonstrates how these interactions can affect the properties of a single molecule due to the influence of the molecular environment, when additional molecules are introduced, forming an ensemble within the junction. Paper 1 with the title "Intermolecular Interactions and Quantum Interference Effects in Molecular Junctions" is included in Appendix A.

3.1 HOW DQI IS AFFECTED BY INTERMOLECULAR INTERACTIONS

Various molecular properties have been investigated throughout the years. One of specific interest is destructive quantum interference (DQI).[38–40] As mentioned earlier this molecular property results in an insulating effect, since the destructive interference reduce the electron transmission. In experiments, this would results in little to no current, as we would imagine for an insulator.

In paper 1 we investigated a group of molecules that posses DQI. Specifically, we examined a group of linear and cross-conjugated molecules, where the cross-conjugated molecules exhibited DQI while the linear molecules did not. The molecules can be seen in Figure 3.1. Our choice of molecules was based on an observation made by Guédon et al.[41], who observed DQI in the cross-conjugated molecule anthraquinone-monothiol (AQ-MT), while no DQI was observed in the linear conjugated molecule anthracene-dithiol (AC-DT). They stated that DQI is linked to the molecular orbitals, indicating that the molecule itself possesses DQI due to its

cross-conjugated nature. While their measurements focused on ensemble junctions, the inherent DQI of the molecule suggests that single-molecule measurements should also exhibit DQI. However, in general, DQI has previously only been observed in ensemble junctions[41–47] or gated single molecules[48, 49], not in single molecule measurements without gating. The interesting question in the context of this chapter is: why?

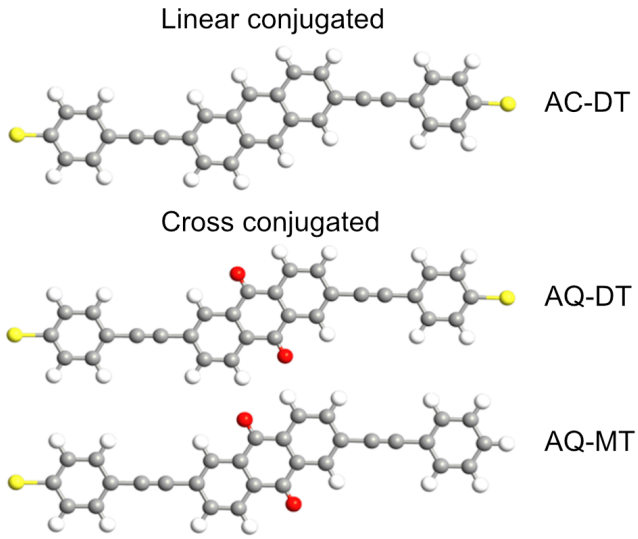

Figure 3.1: The molecules investgated in paper 1. Two cross-conjugated molecules: dithiolated anthraquinone and monothiolated anthraquinone (AQ- DT, AQ-MT) and one linearly conjugated molecule: dithiolated anthracene (AC-DT). Reproduced from Hyllested et al. [P1]

To understand this, it is important to first recognize how DQI is observed in both calculations and experiments. In caculations, DQI is seen as a dip in the transmission spectrum. Figure 3.2a, shows a transmission spectrum with a DQI signature, where energy is on the x-axis (in eV), the Fermi energy is at 0 eV, and transmission is on the y-axis. At 0 eV, a dip is evidnet in the curve; this dip is what is referred to when discussing DQI in transmission spectra. In experiments, DQI is often observed as a similar dip in the differential conductance (dI/dV). This is illustrated in Figure 3.2c with Voltage(V) on the x-axis and dI/dV on the y-axis.

As mentioned in Chapter 2 what we observe around the Fermi energy (0 eV) in the transmission spectrum (Figure 3.2a) is what we expect to see in experiments. If, as shown in Figure 3.2a, there is a dip at the Fermi energy, we would expect to see a similar dip in the dI/dV (Figure 3.2c). Though, if, for some reason, this dip occurs away from the Fermi energy, as in Figure 3.2b, the dip dissapears in the dI/dV plot (Figure 3.2d), leading us to conclude that this molecule does not exhibit DQI. We refer to these two scenarios as the direct and indirect signatures of DQI.

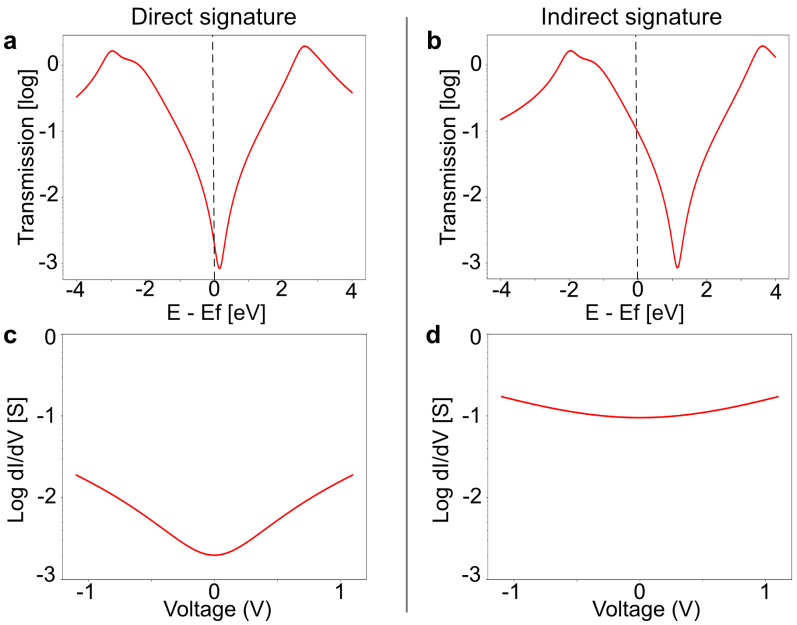

Figure 3.2: Illustration of transmission for the direct (a) and indirect (b) signatures of DQI. The shift is caused by a change in the onsite energies, from 0 eV in (a) to 1 eV in (b). (c, d) Corresponding dI/dV graph for the direct (c) and indirect (d) signatures of DQI, respectively. a - d, was calculated using a Hückel model. Reproduced from Hyllested et al. [P1]

Until now, the focus has been on what we expect to obeserve when discussing DQI. Another important aspect to understand is how molecules interact. This can be either intramolecular or intermolecular. As explained in Chapter 2, intramolecular interactions occur within a single molecule, helping to hold the atoms in place, such as in covalent bonds,

whereas intermolecular interactions occur between molecules. Depending on the molecules involved, different types of interactions can affect the environment that the molecules experience. If the molecules have no effect on one another (i.e., no intermolecular interactions), they would not be influenced by the surrounding molecules. If the molecule is affected by its molecular environment, the interactions could cause a shift in energy, moving the interference feature (the dip, illustrated in Figure 3.2) either up or down in energy, and thus bringing the dip closer to or further away from the Fermi energy.

With this in mind, we calculated the transmission for a series of different junction geometries, ranging from a single molecule to increasingly larger clusters and monolayers. The junction configurations can be seeen in Figure 3.3. The electrodes used in these calculations consists of Au. For clarity, the top electrode is removed in Figure 3.3. The black dots represent the location of the molecule on the electrode surface and the dotted/solid lines illustrate the electrode size. In Figure 3.3a, the solid red line represents the electrode size for a dense monolayer, whereas the dotted red line represents the electrode size for a sparse monolayer. Both the dense and sparse monolayers are calculated with periodic boundary conditions, meaning the unit cell is repeated a certain number of times to simulate a monolayer of molecules. This approach saves computational time since the calculations are relatively small.The dense and sparse monolayers consist of electrodes with 2x2 and 3x3 Au atoms, respectively, while the 9-molecule cluster junction is calculated on a 9x9 Au electrode. In addition to the clusters and sparse/dense monolayers, we also calculated a monolayer with 4 molecules on a 5x5 Au electrode. This configuration was chosen to investigate the difference between the single molecule monolayer (dense and sparse monolayers) and a 4-molecule monolayer. The 4-molecule monolayer was calculated with periodic boundary conditions, similar to the sparse monolayer, but with a larger electrode and unit cell, allowing for four molecules to be placed on the electrode. We will refer to this 4-molecule monolayer as the C4 monolayer. The choice of electrode size for the C4 monolayer was made to mimic the density of the sparse monolayer.

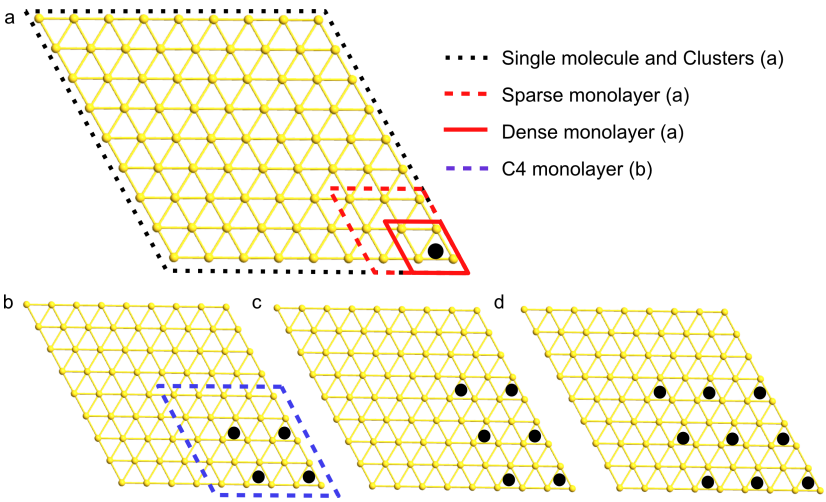

Figure 3.3: Illustration of the different junction configurations. The top gold electrode is removed for clarity. The black dots represent a molecule location, while the dotted/solid lines represent the different electrode size. If no line is present the electrode is the size of the entire Au surface. The single molecule and clusters are all added to a 9×9 Au electrode. The following configurations are depicted: (a) Single molecule (SM) and dense (DM) / sparse (M) monolayer. The single molecule electrode is the dotted black line. The dense and sparse monolayer electrode are the solid and dotted red line, respectively. The single molecule is on a 9×9 Au electrode, whereas the sparse and dense monolayer consist of a single molecule on a 2×2 and 3×3 Au electrode, respectively. (b) 4 molecule cluster (C4) and 4 molecule monolayer (C4M): The electrode of the C4 monolayer is indicated by a dotted line (5×5 Au electrode). (c) 6 molecule cluster (C6). (d) 9 molecule cluster (C9). Adapted from Hyllested et al. [P1]

The transmission for the different junctions is shown in Figure 3.4. The various junction configurations were calcualted for all three molecules shown in Figure 3.1. The transmission spectra of the linear (AC-DT) is show in Figure 3.4a, and the two cross conjugated, AQ-DT and AQ-MT in Figure 3.4b and 3.4c, respectively. As expected, for the linear conjugated molecule (AC-DT) no DQI dip is observed in the tranmission. However, both cross conjugated molecules exhibit the DQI dip for both single molecules (black) and ensemble junctions. This agrees with the inherent DQI due to the cross conjugation of the molecule.

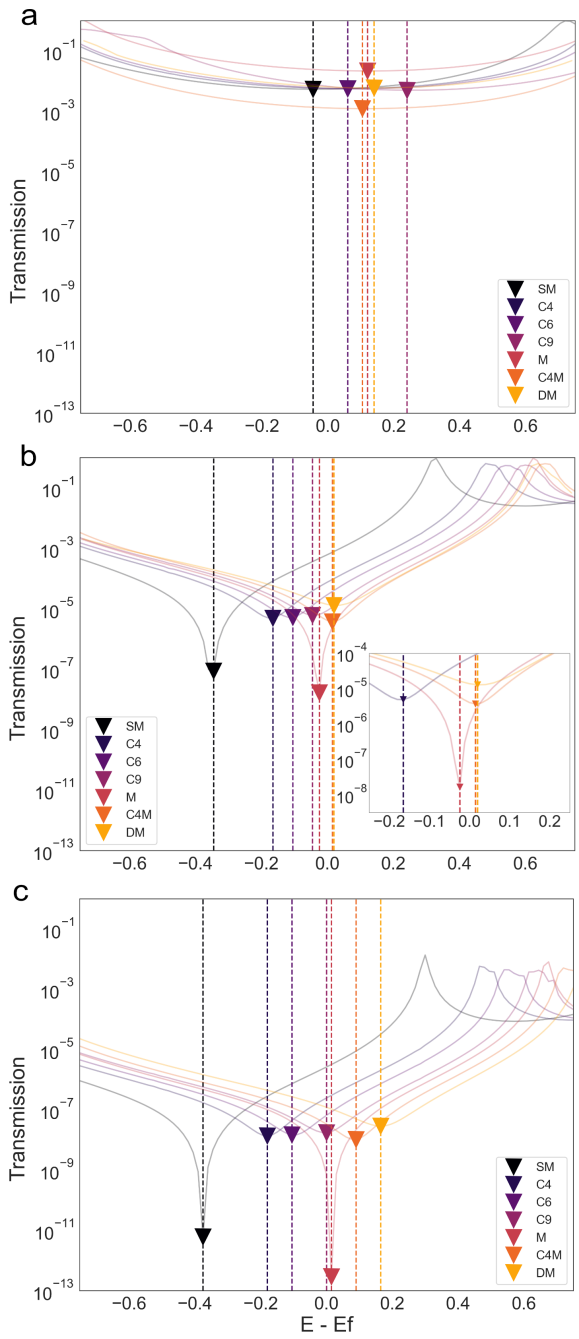

Figure 3.4: Energy-dependent zero-bias transmission spectra for each molecule: AC-DT (a), AQ-DT (b), and AQ-MT (c), calculated with DFT. In each spectrum, the marks highlight the lowest point of transmission. Additionally, the shifts in the transmission features are emphasized by vertical dashed lines, providing visual cues for the changes in the transmission characteristics. Reproduced from Hyllested et al. [P1]

Interestingly, the DQI dip shifts up in energy as we move from the single molecule to the monolayers. This indicate that the molecular interactions caused by the surrounding molecules affect the energy of the dip. With each step towards the monolayer, the dip shifts higher in energy. In Figure 3.4c, the dip for the single molecule is at approximately -0.4 eV, whereas the cluster of four molecules on the same electrode size (9x9 Au electrode) is at approximately -0.2 eV. This upshift in energy with the increase in the number of molecules appears to continue throughout the series.

Another important point to note is the shape of the dip. The single molecule exhibit a sharp dip, whereas the cluster junctions and dense monolayer show a less sharp dip. In comparison, the sparse monolayer appears to have a similar shape to the single molecule, albeit at a higher energy. This indicates that even though the sparse monolayer is calculated to simulate an ensemble of molecules, the shape of the transmission spectrum resembles that of the single molecule, rather than that of an actual ensemble of molecules. This is further demonstrated by examining the C4 monolayer, where the sharpness of the dip decreases from the sparse monolayer to the C4 monolayer.

From these results one could then argue that the dense monolayer is better than the sparse monolayer to simulate the molecular interactions so why would we need to use a bigger electrode with more molecules, when we can simply just use a single molecule on a 2x2 electrode with periodic boundary conditions. In these calculations the difference between the dense monolayer and the C4 monolayer is not extreme. Though, there are differences both in Figure 3.4b and c, where the sparse monolayer has a dip at a higher energy (Figure 3.4c) or more transmission at the same energy (Figure 3.4b). In some cases molecules can be affected by the orientation of the molecules surronding them, and if we use a single molecule on a 2x2 electrode, we cannot control how the other molecules around are oriented. Another point to make is the molecular distance. When we use the small unitcell with the 2x2 electrode, we might unknowingly force the molecules closer together than what is their natural distance. This show that we really need to be careful

with the approach we choose to determine properties of molecules with intermolecular interactions.

3.2 SUMMARY

The findings in Paper 1 indicate that when considering molecules capable of strong intermolecular interactions in calculations, it is essential not to overlook how the molecular environment can affect the results. For example, if we compare the transmission of a cross conjugated single molecule with that of the C4 monolayer, we would not observe DQI for the single molecule in experiments, but we would for the C4 monolayer. This difference arises solely due to the effect of the molecular environment, as the increase in molecular interactions seems to shift the interference feature closer to the Fermi level. We are not suggesting that all calculations necessarily need to be conducted on large electrodes with many molecules. Instead, we emphasize the importance of exercising caution and suggest that preliminary test calculations may be useful to ensure all relevant interactions are accounted for.

4

THE EFFECT OF ELECTRODE CHOICE

This chapter aims to show how the computational results from Paper 2 illustrate that, when simulating experiments with top electrodes alternative to gold, the choice of electrode in the calculations has a greater impact than expected. It highlights that gold electrodes cannot be assumed to cover all scenarios. Paper 2 with the title "Frontier Orbital Gating of Rectification and Conductance in Tunneling Junctions Comprising Pyridine-terminated Molecular Wires" is included in Appendix B.

4.1 INTRODUCTION

Molecules have been measured in various ways: as single molecules in a mechanically controlled break junction with gold electrodes[50], as monolayers on a gold surface with either a gold-coated[51] or platinum-coated[52] top electrode, as monolayers on graphene with a gold top electrode[53], and as monolayers on gold with an eutectic Ga-In(EGaIn) top electrode.[40] Every possible approach has been tested.

To aid the explanation of these types of experiments, theoretical calculations have often been employed. In most cases, the choice of electrodes for the calculations has been straightforward: if the experiments use gold electrodes, the calculations use gold electrodes. However, as mentioned above, some experiments have explored other electrodes. Here, the question becomes how important the shift from gold electrodes used in the calculations to the experimentally chosen electrode is. We know there are limitations in calculations, and some are difficult or even impossible to perform. Meanwhile, Au electrodes are well-known and easy to calculate.

In the literature, many different approaches have been used, and some papers have carried out experiments where the choice of electrodes for the

calculations does not match the electrodes used in the experiment.[54–56] There can be different reasons for this choice. One argument is that the experimental electrode is difficult to calculate, and in this case, it could be argued that changing the Fermi level in the Au-Au junction is sufficient as theoretical support for the experiments.[56] Another argument could be that the effect observed in the experiments is caused by the interaction between the Au substrate and the molecule, meaning the top electrode plays a less significant role.[55] Some papers simply ignore this change and do not argue for their choice of an alternative electrode.[54]

4.2 AU VS AL AS TOP ELECTRODE

In Paper 2, p-oligo(phenylene ethynylene)pyridine (OPPy) compounds with an increasing number of aromatic rings, were measured in an Au-molecule-EGaIn junction to determine the influence of spatially separated frontier orbitals and their coupling to the electrodes on molecular rectification. EGaIn is a liquid metal electrode made of eutectic gallium-indium. It is highly conductive and remains in a liquid state at room temperature. Its flexibility makes it ideal to use as a top electrode in molecular electronics, as it minimizes damage to the molecular structure.[57]

To support the results of these measurements and better understand the cause of rectification, we performed calculations on the measured molecules with aromatic rings ranging from 2 to 5 (the calculated molecules are shown in Figure 4.1). Since EGaIn is a difficult electrode to simulate, we were interested in understanding whether Au electrodes could substitute for EGaIn electrodes in our calculations, or if a metal more similar to EGaIn is necessary for accurate simulations. It is challenging to find a metal with the exact same properties as EGaIn, but one parameter that can be similar is the work function. The work function is the minimum energy that is required to move an electron from the surface into vacuum. It basically gives an indication of how strongly the surface holds onto its electrons. Recently, Kang et al.[58] showed that aluminum can be used as an approximation for EGaIn, based on the similar work functions of Al and EGaIn: 4.1-4.2 eV for EGaIn and

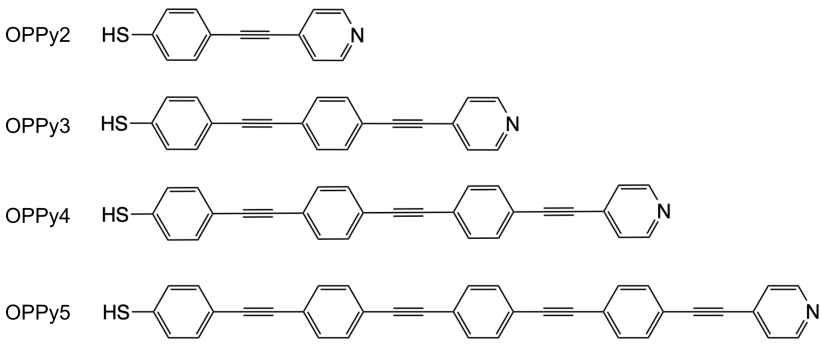

Figure 4.1: Molecular configuration of OPPy2, OPPy3, OPPy4 and OPPy5.

4.25 eV for Al.[59, 60] Additionally, the crystal structures of Al and Au are both face-centered cubic (FCC), and their lattice constants are very similar (Al: 4.046 Å, Au: 4.065 Å).[61] Therefore, following Kang et al., we simply replaced the Au atom with Al atoms in the electrode and calculated all molecules in both Au-molecule-Al and Au-molecule-Au junctions, as shown in Figure 4.2.

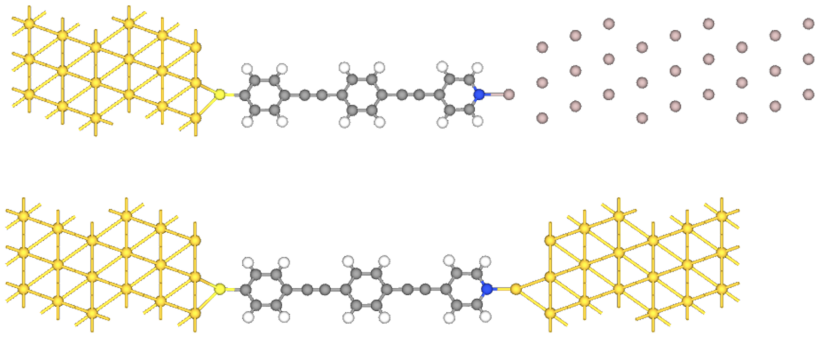

Figure 4.2: Illustration of the Au-OPPy3-Al(top) and Au-OPPy3-Au(bottom) junctions.

Before caculating the junctions, the distance between the nitrogen of the molecule and the top electrode (the right electrode in Figure 4.2) was chosen after optimizing an Al/Au surface, similar to the right electrode (i.e., with an adatom) and the molecule. This resulted in different distances for N-Au (1.99 Å) and N-Al (2.11 Å), as expected

due to the different metals. We purposely did not optimize the junction afterwards, to avoid any charge transfer that would generally happen with two different electrodes.

To compare the two junctions with experimental results, we calculated the IV curves for all molecules in both the Au-Al and Au-Au junctions. These are shown in Figure 4.3. Both IV curves were calculated at 21

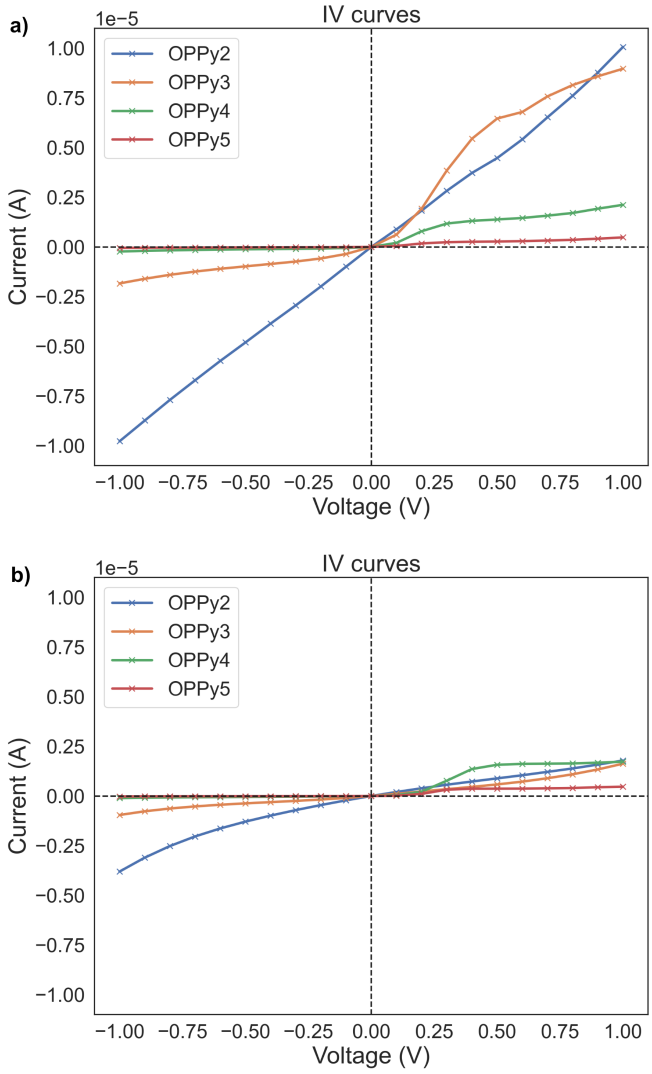

Figure 4.3: Calculated IV curves of OPPy2 (blue), OPPy3(orange), OPPy4(green) and OPPy5(red) for Au-Al junction (a) and the Au-Au junction (b). Reproduced from Soni et al. [P2]

points, spanning from -1 V to +1 V. At each bias step, the transmission was recalculated with the new bias difference and the current was determined from the updated transmission spectrum. This approach is important because the current is calculated as the area under the transmission spectrum, which changes with the applied bias (see equation 2.3).

In Figure 4.3a, the IV curve of the Au-Al junctions is shown, while Figure 4.3b presents the IV curve of the Au-Au junctions. In both cases, the voltage (V) is plotted on the x-axis and the current (A) on the y-axis. A clear difference between the two top electrodes is observed, particularly for OPPy2 (blue) and OPPy3 (orange). The current is higher in the Au-Al junctions for both molecules, and OPPy2 appears to rectify in the opposite direction than expected when placed in the Au-Au junctions (Figure 4.3b). Among the two molecules, OPPy3 is the most interesting to investigate in regard to rectification, as it demonstrates a pronounced difference between the forward bias (+1 V) and reverse bias (-1 V) in the Au-Al junction.

The current observed in the IV curves provides limited information about the degree of rectification. For this, we need the rectification ratio, calculated as the current at forward bias (J+) divided by the current at reverse bias (J-). In Figure 4.4 the reactification ratios for all molcules (OPPy2, OPPy3, OPPy4, OPPy5) are plotted with R displayed on a logaritmic scale. Here, the Au-Al junctions is shown in 4.4a and the Au-Au junction in Figure 4.4b. The triangles corresponds to R at 0.1 V and the circle corresponds to R at 1.0 V. The black horizontal dotted line at zero indicates no rectification; a molecule that does not rectify would have a rectification ratio of 1 (corresponding to 0 on a log scale).

As mentioned earlier, OPPy2 rectifies in the opposite direction compared to all other molecules in the Au-Au junctions, as indicated by the points for OPPy2 being below zero (Figure 4.4b). In the Au-Al junction, no rectification is observed for OPPy2. In contrast, OPPy3 rectifies more in the Au-Al junction than in the Au-Au junction. OPPy4 and OPPy5 show greater rectification than OPPy3 in both junctions, although they seem to rectify slightly more in the Au-Au junction. These rectification

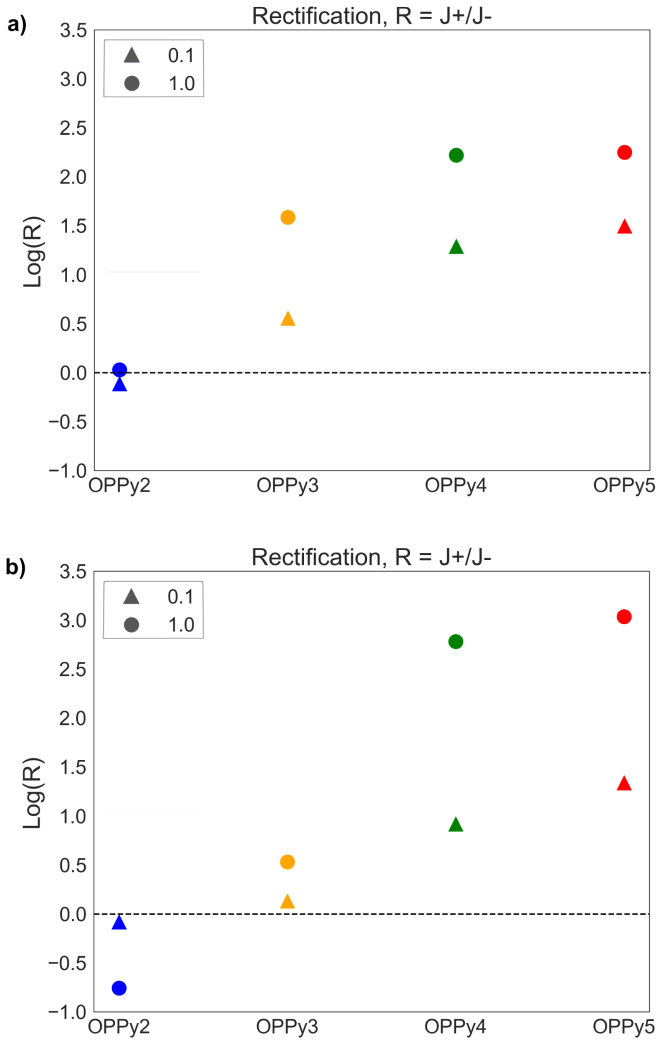

Figure 4.4: Illustration of the rectification ratio for Au-Al (a) and Au-Au (b) junctions for OPPy2 (blue), OPPy3 (orange), OPPy4 (green), and OPPy5 (red). The rectification (R) is calculated as $J+/J-$ and plotted as log(R) vs. voltage (V), displayed as the rectification at 0.1V (triangle) and 1.0V (circle) for each molecule. Reproduced from Soni et al.[P2]

trends support the differences observed in both the IV curves. The two junctions behave differently with the same molecule, even though only the top electrode is changed. Furthermore, in the Au-Al junction, where all molecules rectify in the same direction, the results align more closely with the experimental data compared to the Au-Au junction.

To further explore the differences between the two junctions, the transmission spectrum of OPPy3 at +1 V and -1 V for both junctions are shown in Figure 4.5. The x-axis represents energy in eV, with the Fermi energy at 0 eV, while the y-axis show the transmission. The orange shading represents the bias window at ±1 V, i. e., the area integrated to calculate the current.

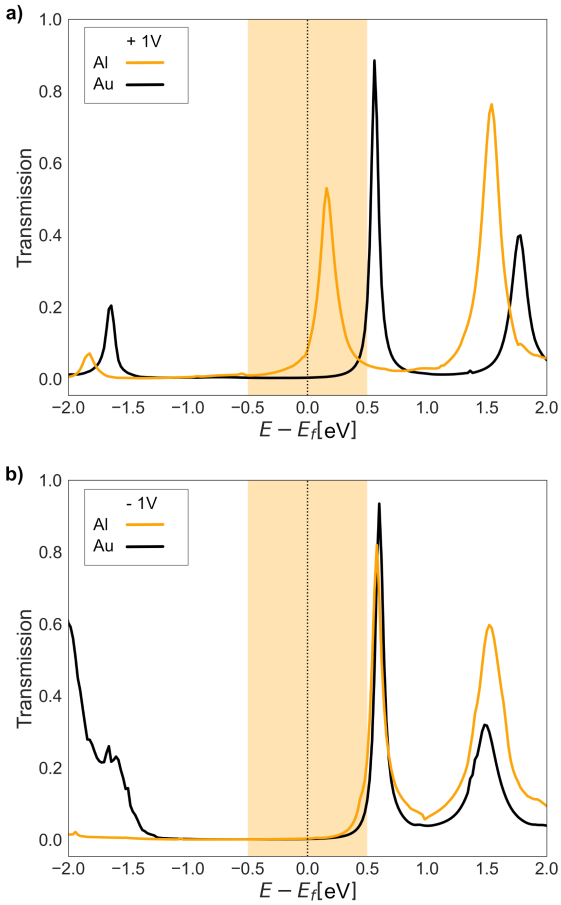

Figure 4.5: Comparison of the transmission for OPPy3 at -1 V(a) and +1 V(b) of the Au-Au(black) and Au-Al(orange) junction. The orange shade corresponds to the bias window. Adapted from Soni et al. [P2]

At -1 V, the LUMO peak for both the Au-Au (black) and Au-Al (orange) junctions is located around 0.5 eV, just outside the bias window, resulting in little to no current. In contrast, at +1 V, the LUMO peak for

the Au-Al junction shifts downward in energy, entering the bias window. This explains why the IV curve for the Au-Al junction exhibits a higher current compared to the Au-Au junction and highlights the difference in the choice of electrode.

4.3 BEHAVIOR OF THE LOWEST UNOCCUPIED MOLECULAR ORBITAL

Now that we have established the importance of the top electrode choice when simulating experiments, we aim to understand the cause of this difference. In Figure 4.6, the LUMO is shown for both the Au-Al and Au-Au junctions for all molecules presented in Figure 4.1. Only the LUMO is presented since the transmission in Figure 4.5 is predominantly LUMO-mediated, as the LUMO peak is the only peak located close to or within the bias window. In the top panel of Figure 4.6, the LUMO is shown at +1 V, and in the bottom panel, it is shown at -1 V. The left side of the figure displays the Au-Al junctions, and the right side shows the Au-Au junctions.

Figure 4.6 demonstrates that the LUMO appears similar for both the Au-Al and Au-Au junctions, with no visually significant differences observed despite the change in the top electrode. Additionally, the bias-dependent behavior of the LUMO is most clearly seen for OPPy5. At +1 V, the LUMO is positioned closer to the right electrode, whereas at -1 V, it shifts and becomes more spread toward the left electrode.

The main difference between the two top electrodes seems to be the energy of the LUMO. Although the LUMO is similar in shape, the actual difference appears to be due to the energy shift of the LUMO peak. In Figure 4.7, the energies of the HOMO and the LUMO are shown with Bias (V) on the y-axis and the energy (eV) on the x-axis. The bias window changes with the applied bias. At 0 V, there is no bias window. As the bias increases, the bias window gradually widens.

Figure 4.7a illustrates the Au-Al junction, while Figure 4.7b represents the Au-Au junction. The trends between the two electrodes are similar. However, for OPPy3 at +1 V, the LUMO is positioned at the edge of

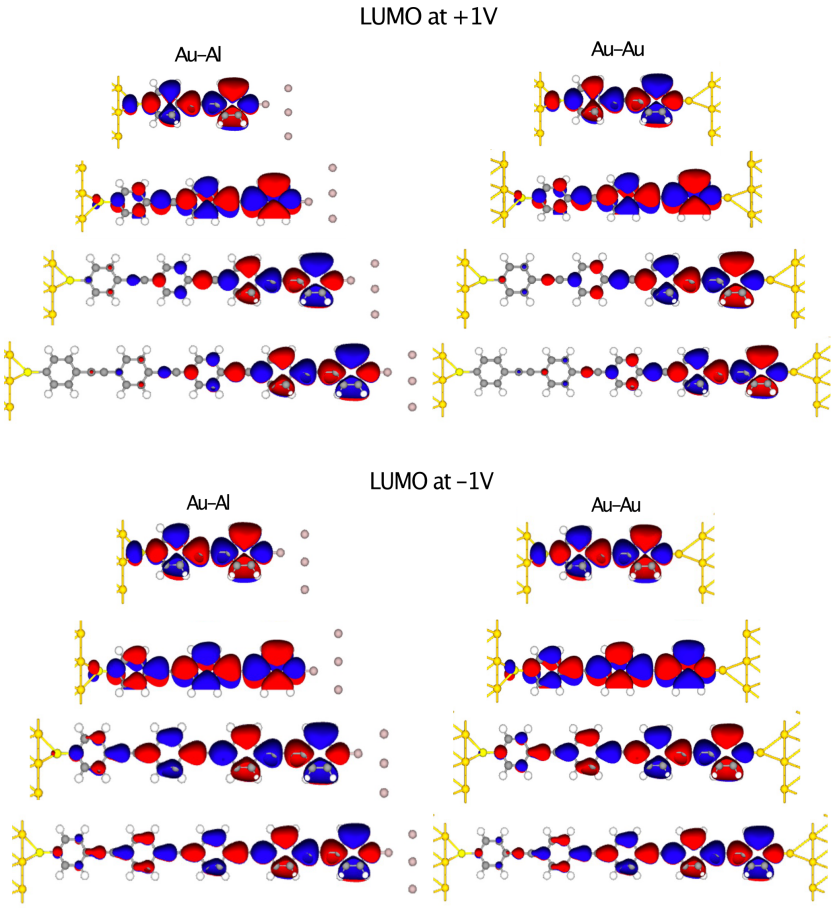

Figure 4.6: Visualization of the molecular orbitals for OPPy2, OPPy3, OPPy4 and OPPy5 for the Al top electrode (left) and the Au top electrode (right). The top panel show the LUMO at +1 V and the bottom panel show the LUMO at -1V.

the bias window in the Au-Au junction (Figure 4.7b), as compared to the Au-Al junction, where it is placed inside the window (Figure 4.7a). This difference is consistent with the behavior shown in Figure 4.5. As previously mentioned, this explains the higher current observed in the IV curves for OPPy3 in the Au-Al junction compared to the Au-Au junction.

In the IV curves, we further observed that OPPy2 in the Au-Au junction (Figure 4.3b) was the only molecule to exhibit rectification in the opposite direction, towards negative bias. This behavior is explained

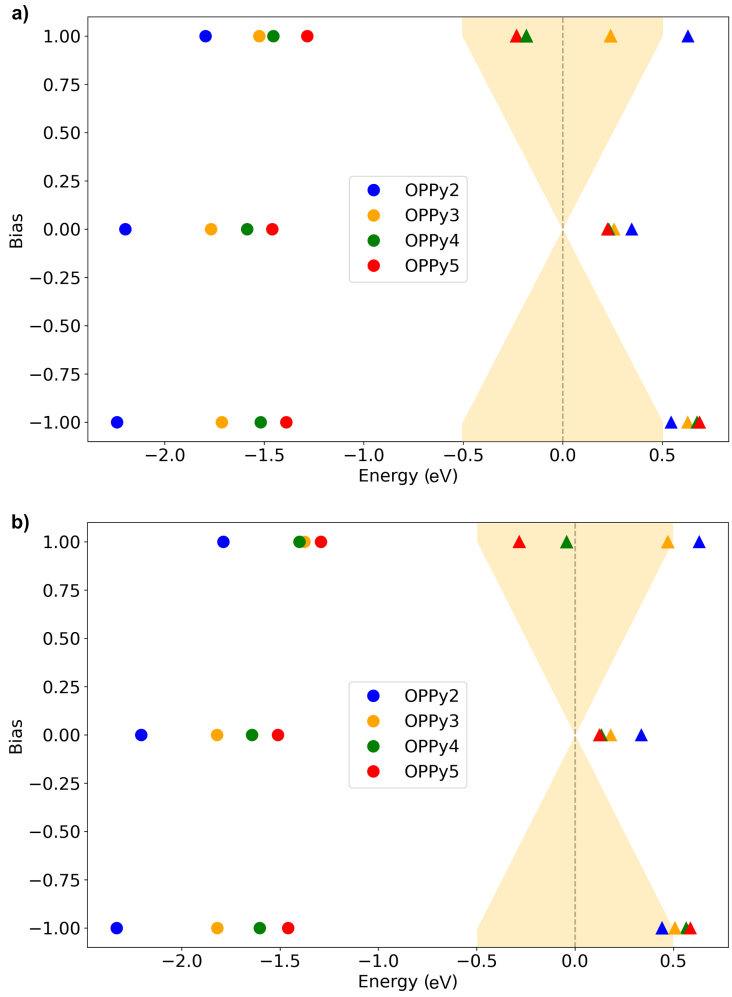

Figure 4.7: Plot of the HOMO-LUMO gap for OPPy2 (blue), OPPy3 (orange), OPPy4 (green) and OPPy5 (red), with bias on the y-axis and energy on the x-axis. The orange shade corresponds to the bias window, and illustrates how it opens up with bias. The HOMO energies are shown as circles and the LUMO energies are shown as triangles. a) show the HOMO-LUMO gaps of Au-Al junction while b) show the HOMO-LUMO gaps of Au-Au junction.

by the location of the LUMO peak of OPPy2 in Figure 4.7. The LUMO peak of OPPy2 is the only example where a LUMO peak lies within the bias window at -1 V. In contrast, both OPPy4 and OPPy5 have their LUMO peaks within the bias window at +1 V but outside the bias

window at -1 V. This explains their rectification towards positive bias and their similar behavior in the IV plot shown in Figure 4.3.

4.4 MULLIKEN POPULATION AND ELECTRON DENSITY

Normally, a shift in the energy of the LUMO peak can be attributed to charge transfer between the molecule and the electrode. To investigate whether this is the cause of the peak movement, we calculated the Mulliken populations for all junctions. The Mulliken populations provide insight into the electronic distribution across the junction. When a bias is applied to the junction, the charge on the molecules increases or decreases compared to the zero-bias condition. Table 4.1 shows the total Mulliken population on the molecule for OPPy2, OPPy3, and OPPy4 in the Au-Al and Au-Al junctions at -1 V, 0 V, and +1 V. To compare the charge differences between the zero-bias and finite-bias junctions, the last two columns present the change in charge on the molecule, obtained by subtracting the zero-bias charge from the finite-bias charge. A positive value indicates that the molecule gains electrons under finite bias, while a negative value indicates that the molecule loses charge. To observe the

Table 4.1: Total Mulliken population on the molecule.

		−1V (a)	0V (b)	+1V (c)	a − b	c − b
Au - Al	OPPy2	70.853	70.761	70.853	0.092	0.092
	OPPy3	106.807	106.781	106.801	0.026	0.02
	OPPy4	142.796	142.778	142.759	0.018	-0.019
Au - Au	OPPy2	70.796	70.786	70.843	0.01	0.057
	OPPy3	106.822	106.799	106.852	0.023	0.053
	OPPy4	142.823	142.803	142.809	0.02	0.006

effect of the charge on the molecule, we can compare it to the movement of the peaks in the transmission spectrum. In Figure 4.8, the transmission of OPPy2 (4.8a,b), OPPy3 (4.8c,d), and OPPy4 (4.8e,f) at -1V and +1V is shown for the Au-Al junction (orange) and the Au-Au junction (black). To illustrate changes in the transmission spectrum under different biases,

the zero-bias transmission is plotted as a dotted line. The orange-shaded background illustrates the bias window at ±1V.

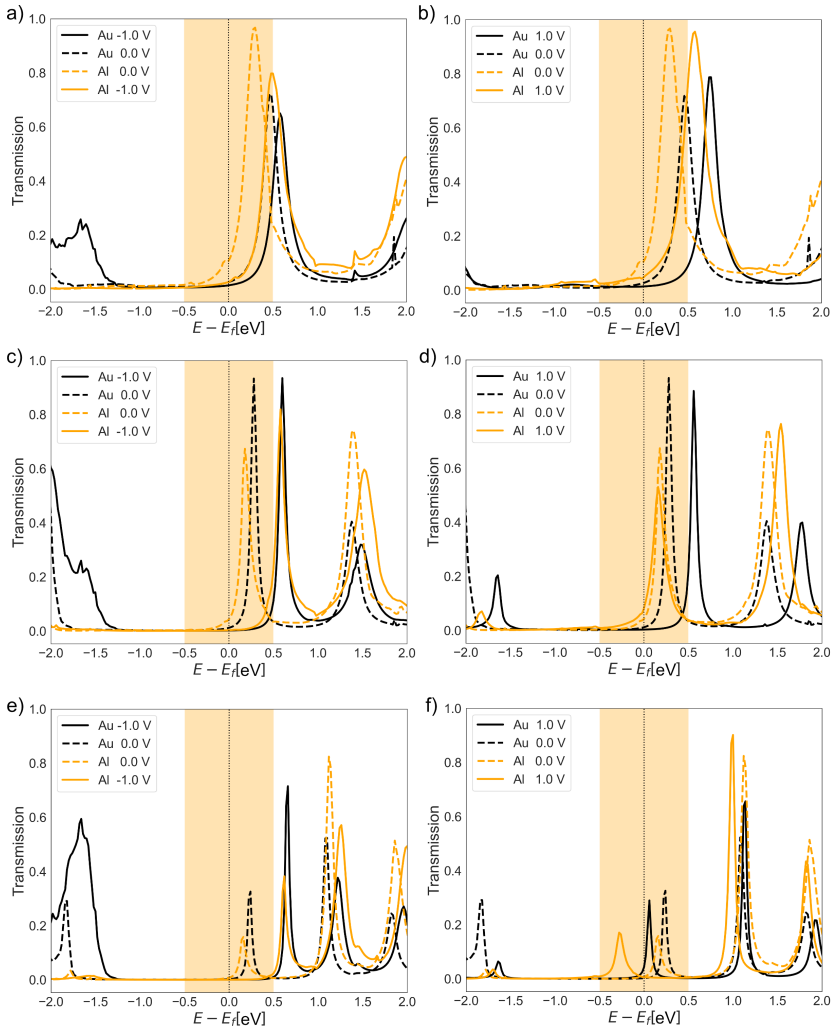

Figure 4.8: Transmission spectra of OPPy2(a,b), OPPy3(c,d) and OPPy4(e,f) at -1 V(a,c,e) and +1 V(b,d,f). Here the Au-Au junctions is shown as the black lines and the Au-Al junctions is shown as the orange line. The dotted line for both junctions corresponds to zero bias. The shaded orange corresponds to the bias window at ±1 V.

From the Mulliken charges of OPPy2 in Table 4.1, we would predict that the peaks in the transmission spectrum would shift up in energy as the molecule gains charge for both the Au-Al and Au-Au junctions. Looking at Figure 4.8a,b, we observe exactly this. The solid lines (finite

bias) shift up in energy compared to the dotted lines (zero bias). For OPPy3, the Mulliken charges show a similar trend, with the molecule gaining charge at both biases for both junctions. However, when examining the transmission of OPPy3 in Figure 4.8c,d, the peak moves up with bias for the Au-Au junction, but for the Au-Al junction at positive bias, the peak appears to remain at the same energy as at zero bias, despite the molecule gaining charge.

To understand if this observation is an outlier, we examine OPPy4. In the Au-Al junction, OPPy4 gains charge at negative bias (a-b) and loses charge at positive bias (c-b). This suggests that the peak should shift in opposite directions at each finite bias compared to zero bias. In the Au-Au junction, OPPy4 gains charge at both finite biases, although at positive bias (c-b) the charge gained is quite small compared to the rest. With this in mind, we turn to the transmission of OPPy4 (Figure 4.8e,f). Indeed, in the Au-Al junction (orange), we observe that the LUMO peak shifts up in energy at negative bias (Figure 4.8e) and down in energy at positive bias (Figure 4.8f). A similar trend is observed for the Au-Au junction. However, at positive bias, where OPPy4 gains only 0.006 charge, the peak still shifts down slightly.

From the Mulliken population and the transmission of the three molecules, we can conclude that OPPy3 is the odd one out when determining the movement of the LUMO peak based on the change in charge on the molecule. However, other factors can also play a role. For these molecules, the LUMO is located closer to the nitrogen (N) atom and, therefore, towards the right electrode (the LUMO of the molecules at positive and negative bias is shown in Figure 4.6). If there is strong coupling to both electrodes, we would expect broad peaks in the transmission spectrum, as observed for OPPy2. This observation correlates with the visualization of the LUMO of OPPy2 in Figure 4.6, where the LUMO is delocalized over the whole molecule. As the molecular length increases, i.e. for OPPy3 and OPPy4, the LUMO becomes more localized toward the right-hand side of the molecule, i.e. closer to the Nitrogen atom, and the peak in the transmission becomes narrower due to the reduced coupling to the electrodes.

It is well known that Mulliken charges are highly sensitive to the choice of basis set and that they partition the electron density based solely on the coefficients of the atomic orbitals (AOs) in the molecular orbitals (MOs). Although the basis set has been kept consistent across all junctions in these calculations, further examining the electron density can provide valuable insight into how the electrons are localized across the junction.

The bias-induced electron density of OPPy2, OPPy3, and OPPy4 is shown in Figures 4.9 and 4.10 for the Au-Al and Au-Au junctions, respectively. All electron density plots represent the difference between finite bias and zero bias. The blue line corresponds to the electron density at negative bias relative to zero bias ($-1V - 0V$), while the red line corresponds to the density at positive bias relative to zero bias ($+1V - 0V$). The two vertical dotted lines indicate the positions of the S atom (left dotted line) and the N atom (right dotted line).

If the electron density is positive, electrons are induced onto the molecule from the electrodes at finite bias. Conversely, if the electron density is negative, electrons are removed from the molecule. In Figure 4.9a, at positive bias (red curve), electrons are transferred to the N atom, while at negative bias (blue curve), electrons are removed from the N atom compared to zero bias.

As observed in Figure 4.6, the LUMO of OPPy2 is spread more evenly across the entire molecule, and a similar trend is seen for the induced electron density. While the Mulliken charges only give the total charge on the molecule, the change of electron density with bias can give insight into the local redistribution of charge. For the Au-Al junction (Figure 4.9a), an increase in electron density at positive bias is observed at both the left and right electrode interface. This effect is less significant in the Au-Au junction (Figure 4.10a). In general, we observe a localization of the LUMO at positive bias and slightly more pronounced delocalization of the LUMO at negative bias (Figure 4.6). A similar trend is reflected in the electron density for all molecules; that is, the gain in electron density appears to follow the behavior of the molecular orbital.

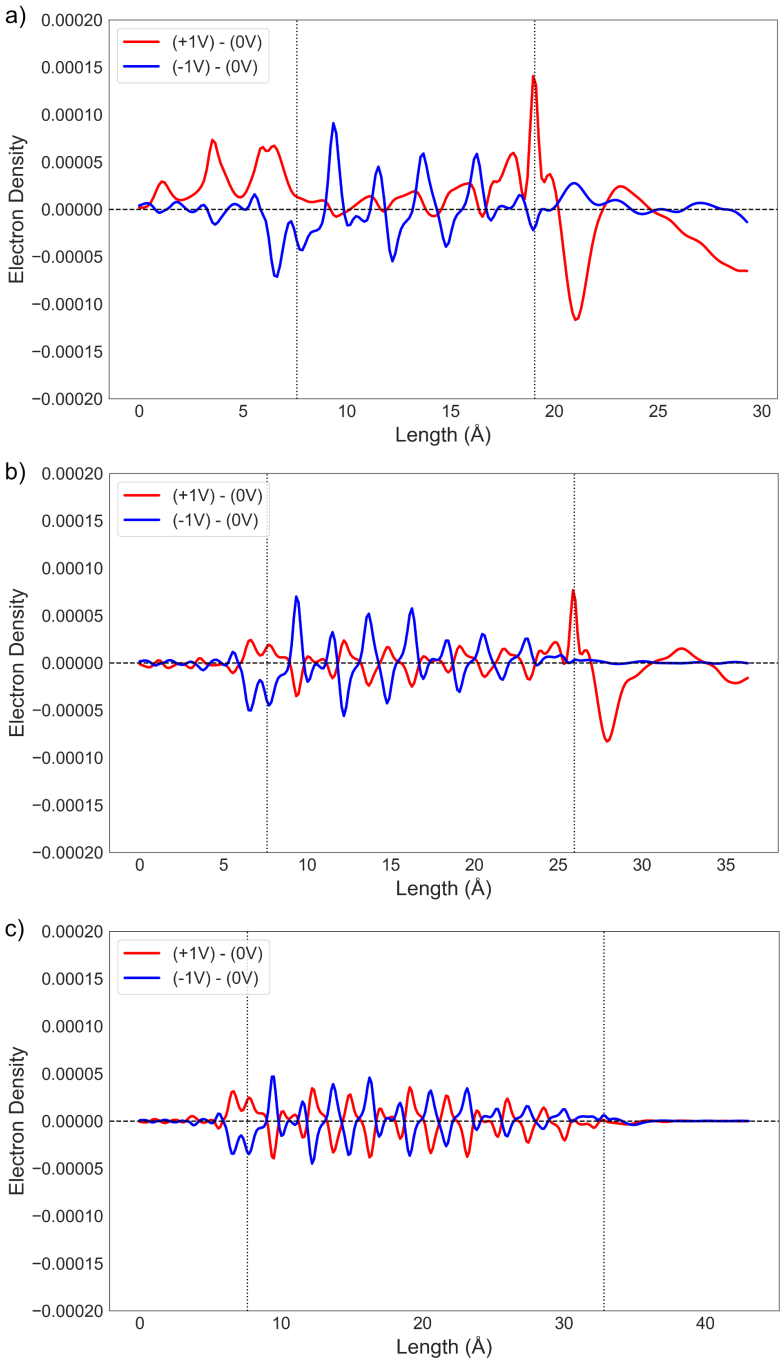

Figure 4.9: Electron density distribution across the Au-Al junctions of OPPy2 (a), OPPy3 (b), and OPPy4 (c), shown as a function of junction length along the x-axis. The distributions represent the difference in electron density between finite bias and zero bias conditions. Red curves indicate positive bias, while blue curves represent negative bias.

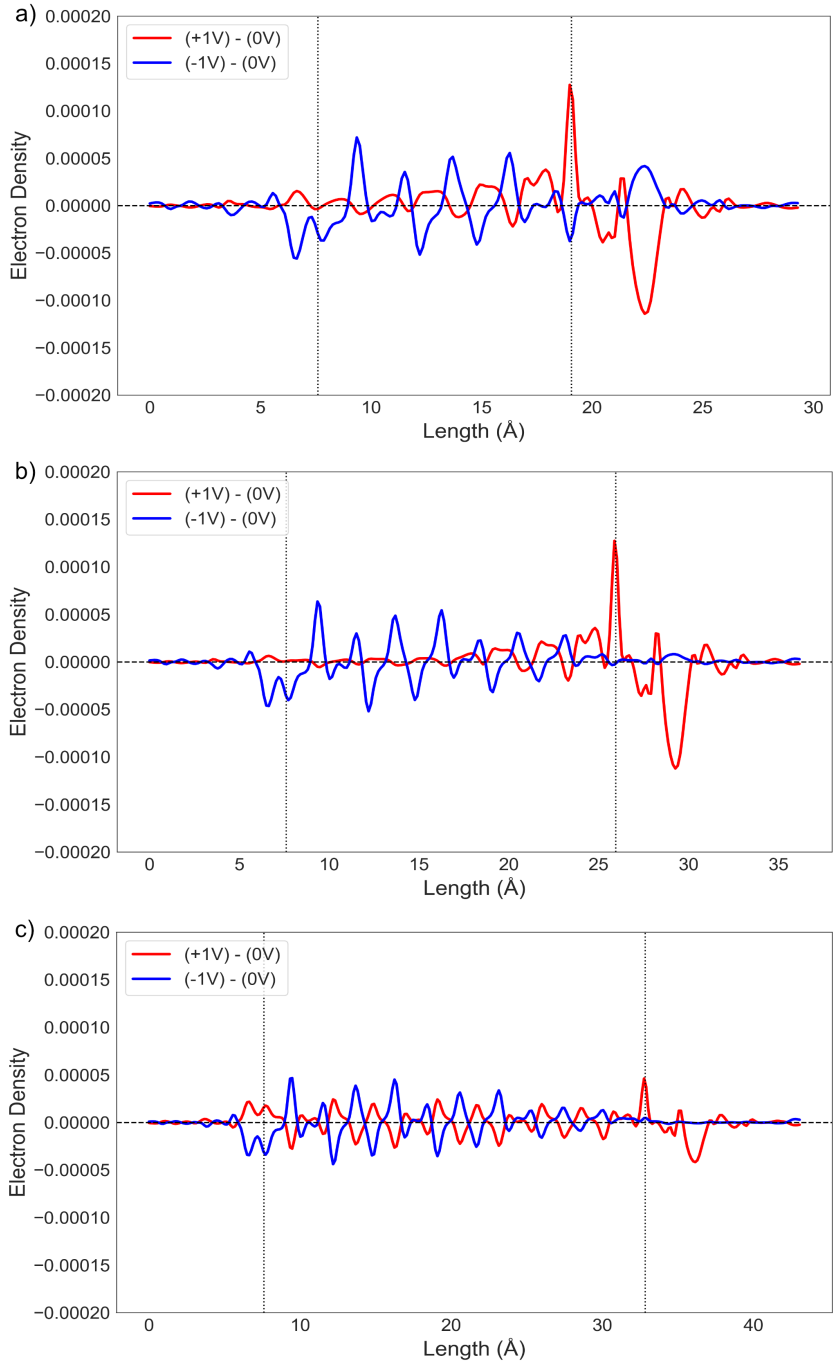

Figure 4.10: Electron density distribution across the Au-Au junctions of OPPy2 (a), OPPy3 (b), and OPPy4 (c), shown as a function of junction length along the x-axis. The distributions represent the difference in electron density between finite bias and zero bias conditions. Red curves indicate positive bias, while blue curves represent negative bias.

One of the main differences observed in the electron density is the amount of charge in the Al electrode for OPPy2 and OPPy3 (Figure 4.9a,b) compared to OPPy4 (Figure 4.9c). Both OPPy2 and OPPy3 show a significant amount of charge in the electrode, which could be attributed to stronger coupling to the electrode. OPPy2 exhibits strong coupling to both the left and right electrodes, whereas OPPy3 primarily shows strong coupling to the right electrode. A similar, though less pronounced, increase in electron density in the right electrode is observed for the Au-Au junction of OPPy2 and OPPy3 (Figure 4.10a,b). In contrast, OPPy4 shows little to no change in electron density in either the left or right electrode (Figure 4.10c).

These results suggest that an additional factor influences the peak shift. Most importantly, it should be noted that we cannot understand from the Mulliken charges or charge density, how much charge is induced specifically in the LUMO. Since the LUMO density is located closer to the top electrode, it appears that the orbital is pinned to the right electrode, causing the LUMO to shift with the chemical potential of the right electrode. In the finite bias calculations, the left electrode is grounded at 0V, while the chemical potential of the right electrode changes with the applied bias. At positive bias, the chemical potential of the right electrode moves down, whereas at negative bias, it moves up. This behavior is exactly what we observe for OPPy4 in Figure 4.8e,f.

The natural question that arises now is why we do not observe this shift for OPPy3 and OPPy2 if the orbital should pin to the chemical potential of the right electrode. We argue that this is due to OPPy2 being strongly coupled to both electrodes, meaning the orbital is more delocalized across the entire molecule, which reduces the impact of the shifting chemical potential. OPPy3, on the other hand, becomes more localized toward the right electrode compared to OPPy2, resulting in weaker coupling to the left electrode. This is evident in Figure 4.9b, where the increase in electron density at +1V in the left electrode is smaller than that observed for OPPy2 (Figure 4.9a). When comparing the electron density in the left electrode of OPPy3 to OPPy4, we see a similar amount of electrons as in the left electrode. Since we observe

that the LUMO peak of OPPy4 follow the chemical potential, we assume that this effect is also to some extend affecting OPPy3, resulting in the LUMO peak staying inside the bias window at positive bias.

This effect is only observed with the Al top electrode, highlighting the importance of the choice of electrode. This may explain why the experiment shows a significantly better rectifier performance for OPPy3 compared to all other molecule lengths.

It is important to note that when using two different electrodes in a calculation, the Fermi level is affected. In the chosen software (QuantumATK), the Fermi levels of the two electrodes are not initially aligned. Therefore, during the calculations, the Fermi level of the right electrode is adjusted to ensure alignment with the left electrode at zero bias. This introduces additional complexity when changing one of the electrodes. However, we observe very similar trends for both electrode configurations. Even when accounting for the Fermi level adjustments, the Al top electrode appears to better replicate the experimental results compared to the Au top electrode.

4.5 SUMMARY

The computational findings in Paper 2 highlight the importance of electrode choice when simulating junctions with a top electrode other than Au. While the LUMO appears similar across different top electrodes, its energetic position shifts with the electrode, resulting in deviations in the corresponding IV curves. This behavior is supported by the Mulliken populations and electron density analysis, which demonstrate that when the charging of the molecule is no longer the primary factor driving the LUMO shift, the chemical potential of the right electrode takes over as the dominant influence.

These insights emphasize that careful consideration of electrode materials is essential for accurately modeling molecular junctions and predicting their behavior, particularly in systems designed for rectification or similar functionalities.

5

THE ROAD TO THIS THESIS

During the development of this thesis, several projects were carried out to achieve the results. This chapter talks about some projects that were abandoned before they were completed. Although some of these turned into side explorations, they did not add directly to the main findings. At the start of this journey, the primary focus was to determine whether it was possible to identify a molecule that, while not exhibiting DQI on its own, would do so as part of an ensemble of molecules. This could involve either a single molecule or a combination of two distinct molecules.

To begin this investigation, the initial approach was to use Hückel theory to test whether it was possible to use a linear conjugated molecule and manipulate its interaction with another linear molecule to produce DQI. For this purpose, we started with (Z)-hexa-1,3,5-triene, shown in Figure 5.1, as a test molecule. Using this molecule, we demonstrated that the coupling site of the electrode to the molecule determines whether DQI is observed. This is illustrated in Figure 5.1a, which show the transmission for different electrode coupling points on the molecule. The blue curve represents coupling to the 1st and 2nd atoms of the molecule, while the red curve represents coupling to the 1st and 3rd atoms. These results align with the Hückel theory example described in Paper 1. We observed that the choice of coupling site could create either a cross-conjugated path or a linear conjugated path, explaining why DQI is observed at certain sites and not at others.

With this knowledge, we set out to experiment with two test molecules to determine whether DQI could be observed when both molecules were connected to electrodes and their interaction was varied. Similar to the single-molecule transmission shown in Figure 5.1a, we only observed DQI when the electrodes were coupled to points on the molecules that allowed for a cross-conjugated path, such as coupling to atoms 1 and 5. However,

when we coupled the electrode to atoms 1 and 5 on one molecule and to atoms 1 and 6 on the other, the DQI observed in the single-molecule transmission was no longer present. This is illustrated in Figure 5.1b. In Figure 5.1b (right), a and b are the interaction integrals depicted as the dotted lines between the two molecules. Additional interaction configurations between the two molecules were tested but did not yield further significant insights. Consequently, these findings did not provide a clear basis for identifying a promising candidate molecule.

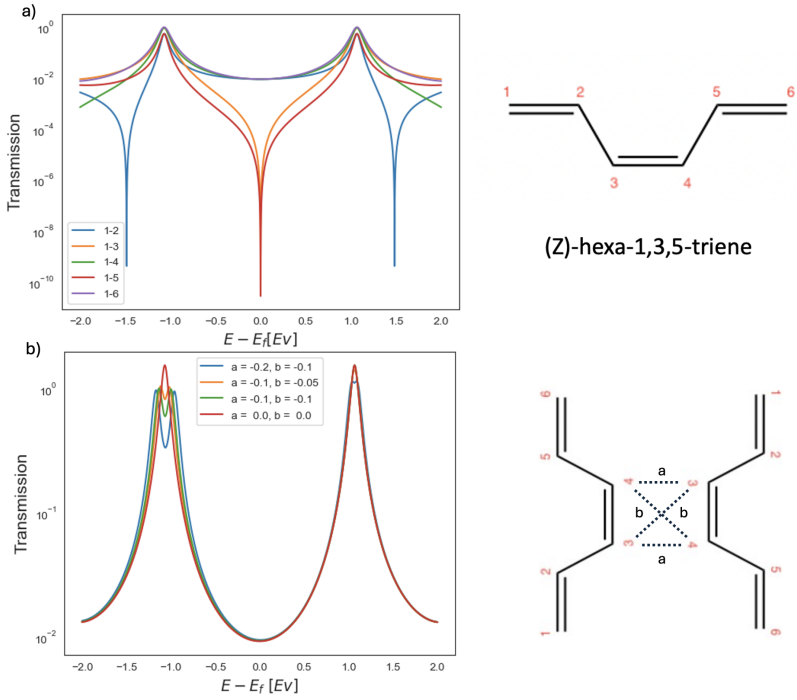

Figure 5.1: Illustration of the (Z)-hexa-1,3,5-triene molecule and the transmission calculated using Hückel theory. (a) Transmission of a single molecule with the electrodes coupled at different atoms, as illustrated on the molecule to the right. (b) Transmission of two molecules, both coupled to electrodes at positions 1 and 6, with varying interaction strengths. The interactions are represented by dotted lines on the molecules shown to the right of the transmission plots.

In 2020, Liu et al.[47] found that an oligo(phenylene ethynylene) (OPE) derivative compound, with the central benzene ring replaced by pentacene (PC), exhibited quantum interference when in an ensemble junction but

not as a single molecule in a single-molecule break junction. This was intriguing because pentacene and OPE are both linearly conjugated. This made the molecule an interesting candidate for the original question. Somehow, it seemed that this molecule in an ensemble junction could exhibit DQI, either due to intermolecular interactions or some other factor, overcoming the constructive interference that made the DQI non-visible in the Hückel calculations performed for the test molecule ((Z)-hexa-1,3,5-triene). The oligo(phenyleneethynylene)-pentacene molecule (OPE-PC) is shown in Figure 5.2.

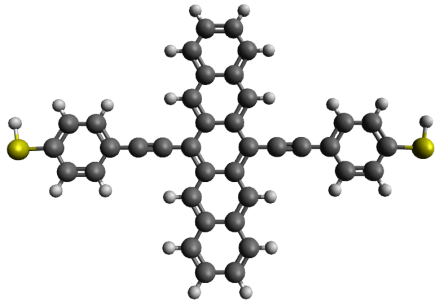

Figure 5.2: Illustration of the oligo(phenylene ethynylene)-pentacene (OPE-PC) molecule.

Based on the findings of Liu et al., we aimed to investigate the cause of the DQI observed in ensemble junctions but not in single molecules for OPE-PC. Using Hückel theory as a screening method, we set out to determine the optimal relative orientation of the two molecules and understand how the overlap between their pentacene units should be configured to replicate the DQI observed in the experiments.

In Figure 5.3, the transmission calculated using Hückel theory for different amounts of overlapping rings is shown. "5" corresponds to complete overlap, while "side" and "tip" correspond to only the sides or tips of the molecules overlapping, respectively. Figure 5.3a shows the transmission when both pentacene units are coupled to both electrodes, whereas Figure 5.3b shows the transmission when each pentacene unit is coupled to a single electrode. For comparison, the side/tip curve is the same in both figures.

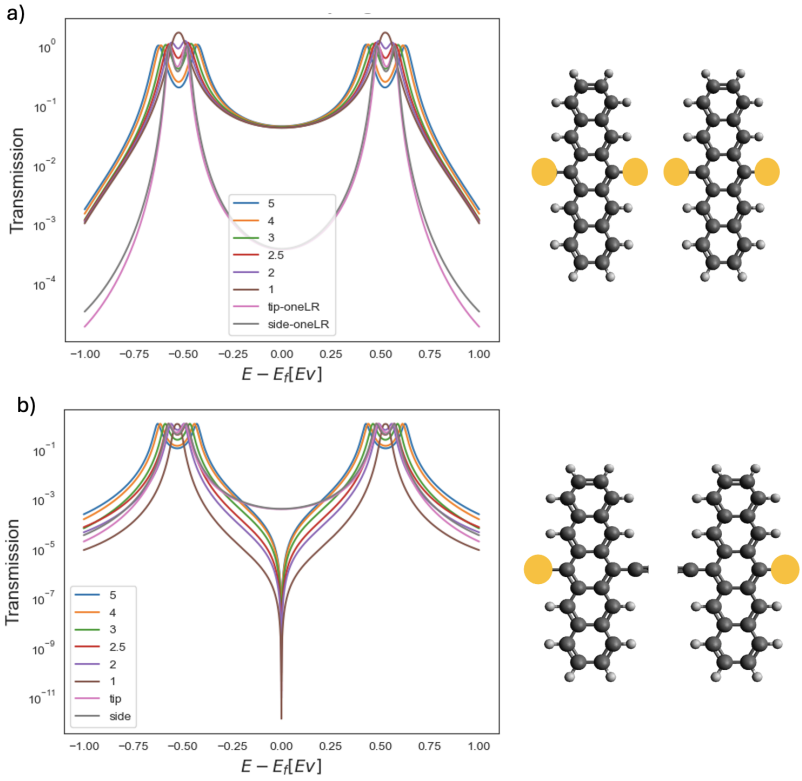

Figure 5.3: Illustration of the transmission (log scale) of the pentacene unit in the OPE-PC molecule with varying degrees of overlapping rings. '5' represents complete overlap of all rings, while 'side' and 'tip' correspond to partial overlap at the side or tip of each molecule, respectively. (a) Both molecules are connected to two electrodes. (b) Each molecule is connected to a single electrode. The configurations are depicted to the right of each transmission spectrum.

When both molecules were coupled to both the left and right electrodes, no DQI was observed, as shown in Figure 5.3a. However, when only the left side of one molecule and the right side of the other molecule were coupled to electrodes—forcing the path to go through both molecules—DQI was observed, as shown in Figure 5.3b. These results suggest that the cause of the DQI is related to the molecules being coupled to separate electrodes. However, as mentioned earlier, the EGaIn electrode is a flexible top electrode, so this explanation does not seem plausible.

To continue the investigation, we aimed to take the calculations a step further by using DFT. The next step involved incorporating two OPE-PC

molecules into the junction. Since the Hückel screening calculations did not yield satisfactory results, we calculated the binding energy of two OPE-PC molecules while varying their relative positions. One molecule was kept stationary, and the distance between the two molecules was fixed at 3.445 Å. The other molecule was shifted along the x- and y-axes, with a maximum displacement of 4 Å in the x direction and 6 Å in the y direction, in increments of 0.5 Å.

To illustrate this, we generated a heatmap of the binding energies, as shown in Figure 5.4b. An illustration of the x- and y-directions representing the movement of the molecule is provided in Figure 5.4a. The

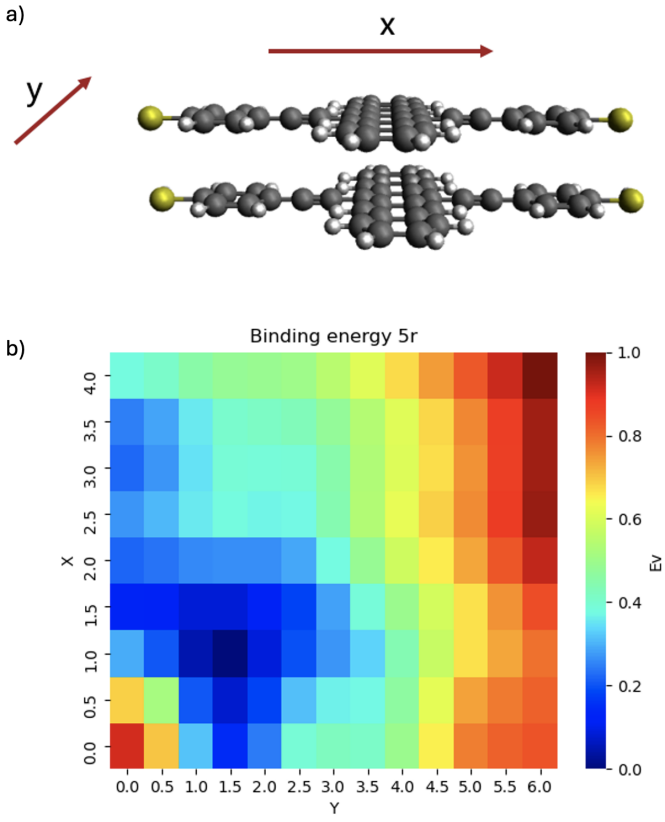

Figure 5.4: Illustration of the binding energies of two OPE-PC molecules. (a) Depicts the relative movements of the two molecules with respect to each other. (b) Shows a heatmap of the normalized binding energies, calculated using the M062X/6-31+G(d,p) functional and basis set.

calculations were performed using the M062X/6-31+G(d,p) functional and basis set, with the inclusion of dispersion and counterpoise corrections to accurately capture non-covalent interactions. These corrections account for basis set superposition effects, enhancing the accuracy of the calculated binding energies. For clarity, the binding energies were normalized.

From the heatmap, the binding energy is lowest around x = 1.0 Å and y = 1.5 Å. This indicates that this configuration is the most stable, suggesting a favorable interaction between the two molecules at this specific relative position compared to other configurations.

Based on these results, we calculated the transmission of OPE-PC as a single molecule on a 6×6 gold electrode and as two molecules in the most stable configuration (x=1.0 Å and y = 1.5 Å) on the same electrode. Consistent with the experiment, we observed that when OPE-PC was calculated as a single molecule, the transmission did not exhibit any DQI features at or near the Fermi level. The calculated transmission can be seen in Figure 5.5a.

Given the experimental findings, we would expect that incorporating two molecules into the junction might reveal some form of DQI. However, as shown in Figure 5.5b, this was not the case. While the transmission for the two molecules is lower, it remains relatively high. Furthermore, no significant peak movement is observed. Although dips in the transmission are evident further from the Fermi level, these are too far away to be detected experimentally.

Similar calculations were carried out for molecules in which the pentacene unit was replaced with anthracene, tetracene, and hexacene. However, none of these variations provided any useful insights. Therefore, based on these results, we are unable to explain why DQI is observed for the OPE-PC molecule in an ensemble junction but not in a single-molecule configuration. The only scenario where DQI was observed was when each molecule was coupled to a single electrode.

At the time of these calculations, we did not consider using aluminum as the top electrode—a choice we later discovered to be more suitable—but instead used gold for both electrodes. As a result, we cannot

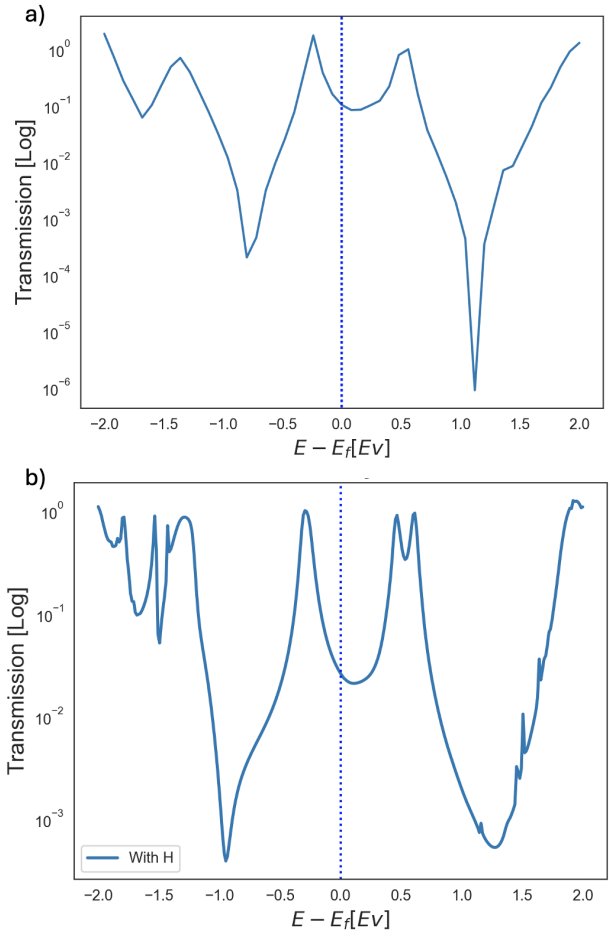

Figure 5.5: Transmission spectrum of a single OPE-PC molecule (a) and two OPE-PC molecules in the x=1.0 Å and y=1.5 Å configuration (b) within a gold-molecule-gold junction, both using the same 6x6 electrode configuration.

determine whether a different top electrode, such as aluminum, could shift the features in the transmission enough to make them observable in experiments. However, the dips observed in the transmission spectrum for the two molecules in the junction still exhibit relatively high transmission values, raising further questions about whether a change in the top electrode would be sufficient to observe any DQI. Furthermore, we did not perform any calculations with an applied bias, which, as discussed in Chapter 4, can significantly influence the results in certain cases.

Other approaches have been explored, such as investigating the effect of hydrogen bonding to induce DQI in an otherwise linear molecule, examining how the electrode's work function influences the monolayer, and determining whether it is possible to short-circuit a molecule by combining a long and a short linearly conjugated molecule, thereby forcing a path between the two molecules. However, none of these investigations have yielded meaningful results thus far.

5.1 SUMMARY

This section illustrates that identifying molecules that exhibit DQI only in ensemble junctions, but not as single molecules, is not straightforward. Even with a molecule that showed promising results in experiments, the theoretical calculations did not provide supporting evidence. This further highlights the challenges involved in searching for specific molecular features or properties. The process often requires extensive trial and error, exploring different ideas, and accounting for subtle factors that may influence the results, making the task far more complex than it might initially seem.

6

CONCLUSION

The work presented in this thesis explored the impact of molecular interactions and electrode choice on the observation of molecular properties in computational calculations. Specifically, it investigated how properties such as destructive quantum interference and rectification are influenced by intermolecular interactions and electrode choice. The findings highlight the critical importance of the calculation setup. Simulating monolayer experiments with a single molecule requires caution, as intermolecular interactions can significantly influence the observed results. This reinforces the need to account for these interactions, as such simulations may not fully capture the complexities of experimental conditions. While density functional theory is a robust and widely used tool in computational chemistry, it is essential to remain mindful of its assumptions to avoid overinterpreting results.

The significance of of Paper 1 lies in its contribution to refining the modeling of molecular junctions based on the specific properties of the molecules under investigation. Not all systems exhibit intermolecular interactions that meaningfully affect transmission and conductance, making it unnecessary to include multiple molecules in every simulation. However, as highlighted in Paper 2, electrode choice can influence the rectifying properties. This finding suggests that electrode choice could similarly affect other molecular junctions, emphasizing the need for careful evaluation in computational studies.

While the results of these studies are promising, they are not without limitations. Computational methods inherently have constraints and cannot fully replicate experimental conditions. The use of DFT as the standard approach introduces assumptions about the physical world. While these assumptions are not inherently problematic, they must be acknowledged and carefully interpreted to draw meaningful conclusions.

The key takeaway from this thesis is the importance of critically evaluating how we simulate molecular junctions. In the future, computational methods may become the first and most efficient way to screen large groups of molecules before conducting experimental measurements. However, if crucial aspects—such as electrode choice and molecular interactions—are overlooked, we risk discarding molecules that may possess valuable and interesting properties for molecular electronics. By refining our approaches to simulation, we can enhance the predictive power of computational studies and support the advancement of molecular electronics.

BIBLIOGRAPHY

[1] M. Kwiat, S. Cohen, A. Pevzner, and F. Patolsky. "Large-scale ordered 1D-nanomaterials arrays: Assembly or not?" In: *Nano Today* 8 (6 Dec. 2013), pp. 677–694. DOI: 10.1016/j.nantod.2013.12.001.

[2] Y. Zhao, W. Liu, J. Zhao, Y. Wang, J. Zheng, J. Liu, W. Hong, and Z. Q. Tian. "The fabrication, characterization and functionalization in molecular electronics." In: *International Journal of Extreme Manufacturing* 4 (2 June 2022). DOI: 10.1088/2631-7990/ac5f78.

[3] W. Lu and C. M. Lieber. "Nanoelectronics from the bottom up." In: *Nature Materials* 6 (11 Nov. 2007), pp. 841–850. DOI: 10.1038/nmat2028.

[4] H. Klauk, U. Zschieschang, J. Pflaum, and M. Halik. "Ultralow-power organic complementary circuits." In: *Nature* 445 (7129 Feb. 2007), pp. 745–748. DOI: 10.1038/nature05533.

[5] Y. Duan, B. Zhang, S. Zou, C. Fang, Q. Wang, Y. Shi, and Y. Li. "Low-power-consumption organic field-effect transistors." In: *JPhys Materials* 3 (1 Jan. 2020). DOI: 10.1088/2515-7639/ab6305.

[6] M. S. I. Veitía and C. Ferroud. "New activation methods used in green chemistry for the synthesis of high added value molecules." In: *International Journal of Energy and Environmental Engineering* 6 (1 Mar. 2015), pp. 37–46. DOI: 10.1007/s40095-014-0148-7.

[7] Z. J. Donhauser et al. "Conductance Switching in Single Molecules Through Conformational Changes." In: *Science* 292 (5525 June 2001), pp. 2303–2307. DOI: 10.1126/science.1060294.

[8] Z. Liu, S. Ren, and X. Guo. "Switching Effects in Molecular Electronic Devices." In: *Topics in Current Chemistry* 375 (3 June 2017), p. 56. DOI: 10.1007/s41061-017-0144-5.

[9] R. Sun, J. Lv, X. Xue, S. Yu, and Z. Tan. *Chemical Sensors using Single-Molecule Electrical Measurements*. Aug. 2023. DOI: 10.1002/asia.202300181.

[10] C. J. Yu, S. V. Kugelgen, D. W. Laorenza, and D. E. Freedman. "A Molecular Approach to Quantum Sensing." In: *ACS Central Science* 7 (5 May 2021), pp. 712–723. DOI: 10.1021/acscentsci.0c00737.

[11] B. Zhang, M. H. Garner, L. Li, L. M. Campos, G. C. Solomon, and L. Venkataraman. "Destructive quantum interference in heterocyclic alkanes: The search for ultra-short molecular insulators." In: *Chemical Science* 12 (30 Aug. 2021), pp. 10299–10305. DOI: 10.1039/d1sc02287c.

[12] M. H. Garner et al. "Comprehensive suppression of single-molecule conductance using destructive σ-interference." In: *Nature* 558 (7710 June 2018), pp. 416–419. DOI: 10.1038/s41586-018-0197-9.

[13] N. Robertson and C. A. McGowan. "A comparison of potential molecular wires as components for molecular electronics." In: *Chemical Society Reviews* 32 (2 Feb. 2003), pp. 96–103. DOI: 10.1039/b206919a.

[14] A. S. Blum, J. G. Kushmerick, D. P. Long, C. H. Patterson, J. C. Yang, J. C. Henderson, Y. Yao, J. M. Tour, R. Shashidhar, and B. R. Ratna. "Molecularly inherent voltage-controlled conductance switching." In: *Nature Materials* 4 (2 Feb. 2005), pp. 167–172. DOI: 10.1038/nmat1309.

[15] A. Facchetti. "Semiconductors for organic transistors." In: *Materials Today* 10 (3 Mar. 2007), pp. 28–37. DOI: 10.1016/S1369-7021(07)70017-2.

[16] W. Kohn and L. J. Sham. "Self-Consistent Equations Including Exchange and Correlation Effects." In: *Physical Review* 140 (4A Nov. 1965), A1133–A1138. DOI: 10.1103/PhysRev.140.A1133.

[17] S. Datta. *Electronic Transport in Mesoscopic Systems*. Vol. 1. Cambridge University Press, Sept. 1995. DOI: 10.1017/CBO9780511805776.

[18] S. Smidstrup et al. "QuantumATK: an integrated platform of electronic and atomic-scale modelling tools." In: *Journal of Physics: Condensed Matter* 32 (1 Jan. 2020), p. 015901. DOI: 10.1088/1361-648X/ab4007.

[19] Synopsis A/S. *QuantumATK version S-2021.06-SP1 and version 2022-S*. Accessed on November 26, 2024. URL: https://www.synopsys.com/manufacturing/quantumatk.html.

[20] J. P. Perdew, K. Burke, and M. Ernzerhof. "Generalized Gradient Approximation Made Simple." In: *Physical Review Letters* 77 (18 Oct. 1996), pp. 3865–3868. DOI: 10.1103/PhysRevLett.77.3865.

[21] S. Grimme, S. Ehrlich, and L. Goerigk. "Effect of the damping function in dispersion corrected density functional theory." In: *Journal of Computational Chemistry* 32 (7 May 2011), pp. 1456–1465. DOI: 10.1002/jcc.21759.

[22] A. Scheer, G. Gallup, and P. Burrow. "Unoccupied orbital energies of 1,4-benzenedithiol and the HOMO–LUMO gap." In: *Chemical Physics Letters* 466 (4-6 Dec. 2008), pp. 131–135. DOI: 10.1016/j.cplett.2008.10.057.

[23] J. L. Bao, L. Gagliardi, and D. G. Truhlar. "Self-Interaction Error in Density Functional Theory: An Appraisal." In: *The Journal of Physical Chemistry Letters* 9 (9 May 2018), pp. 2353–2358. DOI: 10.1021/acs.jpclett.8b00242.

[24] W. Kohn. "Density functional theory for systems of very many atoms." In: *International Journal of Quantum Chemistry* 56 (4 Nov. 1995), pp. 229–232. DOI: 10.1002/qua.560560407.

[25] K. Camilleri. "Heisenberg and the wave–particle duality." In: *Studies in History and Philosophy of Science Part B: Studies in History and Philosophy of Modern Physics* 37 (2 June 2006), pp. 298–315. DOI: 10.1016/j.shpsb.2005.08.002.

[26] R. P. Feynman, R. B. Leighton, M. Sands, and S. Treiman. *The Feynman Lectures on Physics*. 1964.

[27] A. H. Tavabi, C. B. Boothroyd, E. Yücelen, S. Frabboni, G. C. Gazzadi, R. E. Dunin-Borkowski, and G. Pozzi. "The Young-Feynman controlled double-slit electron interference experiment." In: *Scientific Reports* 9 (1 July 2019), p. 10458. DOI: 10.1038/s41598-019-43323-2.

[28] S. Frabboni, G. C. Gazzadi, and G. Pozzi. "Young's double-slit interference experiment with electrons." In: *American Journal of Physics* 75 (11 Nov. 2007), pp. 1053–1055. DOI: 10.1119/1.2757621.

[29] A. D. Arulsamy. "One- and two-slit experiments using photons and electrons: A proper resolution." In: *Results in Optics* 15 (May 2024), p. 100638. DOI: 10.1016/j.rio.2024.100638.

[30] S. Frabboni, G. C. Gazzadi, V. Grillo, and G. Pozzi. "Elastic and inelastic electrons in the double-slit experiment: A variant of Feynman's which-way set-up." In: *Ultramicroscopy* 154 (July 2015), pp. 49–56. DOI: 10.1016/j.ultramic.2015.03.006.

[31] T. Hansen, G. C. Solomon, D. Q. Andrews, and M. A. Ratner. "Interfering pathways in benzene: An analytical treatment." In: *Journal of Chemical Physics* 131 (19 2009). DOI: 10.1063/1.3259548.

[32] H. Valkenier, C. M. Guédon, T. Markussen, K. S. Thygesen, S. J. V. D. Molen, and J. C. Hummelen. *Cross-conjugation and quantum interference: A general correlation?* Jan. 2014. DOI: 10.1039/c3cp53866d.

[33] G. C. Solomon, D. Q. Andrews, R. H. Goldsmith, T. Hansen, M. R. Wasielewski, R. P. V. Duyne, and M. A. Ratner. "Quantum interference in acyclic systems: Conductance of cross-conjugated molecules." In: *Journal of the American Chemical Society* 130 (51 Dec. 2008), pp. 17301–17308. DOI: 10.1021/ja8044053.

[34] A. Aviram and M. A. Ratner. "Molecular rectifiers." In: *Chemical Physics Letters* 29 (2 Nov. 1974), pp. 277–283. DOI: 10.1016/0009-2614(74)85031-1.

[35] A. Troisi and M. A. Ratner. "Conformational molecular rectifiers." In: *Nano Letters* 4 (4 Apr. 2004), pp. 591–595. DOI: 10.1021/nl0352088.

[36] C. V. Dyck and M. A. Ratner. "Molecular rectifiers: A new design based on asymmetric anchoring moieties." In: *Nano Letters* 15 (3 Mar. 2015), pp. 1577–1584. DOI: 10.1021/nl504091v.

[37] R. M. Metzger. "Unimolecular electrical rectifiers." In: *Chemical Reviews* 103 (9 Sept. 2003), pp. 3803–3834. DOI: 10.1021/cr020413d.

[38] L. A. Zotti and E. Leary. "Taming quantum interference in single molecule junctions: Induction and resonance are key." In: *Physical Chemistry Chemical Physics* 22 (10 Mar. 2020), pp. 5638–5646. DOI: 10.1039/c9cp06384f.

[39] C. Tang, L. Huang, S. Sangtarash, M. Noori, H. Sadeghi, H. Xia, and W. Hong. "Reversible Switching between Destructive and Constructive Quantum Interference Using Atomically Precise Chemical Gating of Single-Molecule Junctions." In: *Journal of the American Chemical Society* 143 (25 June 2021), pp. 9385–9392. DOI: 10.1021/jacs.1c00928.

[40] Y. Zhang, G. Ye, S. Soni, X. Qiu, T. L. Krijger, H. T. Jonkman, M. Carlotti, E. Sauter, M. Zharnikov, and R. C. Chiechi. "Controlling destructive quantum interference in tunneling junctions comprising self-assembled monolayers: Via bond topology and functional groups." In: *Chemical Science* 9 (19 2018), pp. 4414–4423. DOI: 10.1039/c8sc00165k.

[41] C. M. Guédon, H. Valkenier, T. Markussen, K. S. Thygesen, J. C. Hummelen, and S. J. van der Molen. "Observation of quantum interference in molecular charge transport." In: *Nature Nanotechnology* 7 (5 May 2012), pp. 305–309. DOI: 10.1038/nnano.2012.37.

[42] Y. Zhang, G. Ye, S. Soni, X. Qiu, T. L. Krijger, H. T. Jonkman, M. Carlotti, E. Sauter, M. Zharnikov, and R. C. Chiechi. "Controlling destructive quantum interference in tunneling junctions comprising self-assembled monolayers via bond topology and functional

groups." In: *Chemical Science* 9 (19 2018), pp. 4414–4423. DOI: 10.1039/C8SC00165K.

[43] D. Fracasso, H. Valkenier, J. C. Hummelen, G. C. Solomon, and R. C. Chiechi. "Evidence for Quantum Interference in SAMs of Arylethynylene Thiolates in Tunneling Junctions with Eutectic Ga–In (EGaIn) Top-Contacts." In: *Journal of the American Chemical Society* 133.24 (2011), pp. 9556–9563. DOI: 10.1021/ja202471m.

[44] V. Rabache, J. Chaste, P. Petit, M. L. Della Rocca, P. Martin, J.-C. Lacroix, R. L. McCreery, and P. Lafarge. "Direct Observation of Large Quantum Interference Effect in Anthraquinone Solid-State Junctions." In: *Journal of the American Chemical Society* 135.28 (2013), pp. 10218–10221. DOI: 10.1021/ja403577u.

[45] M. Carlotti, A. Kovalchuk, T. Wächter, X. Qiu, M. Zharnikov, and R. C. Chiechi. "Conformation-driven quantum interference effects mediated by through-space conjugation in self-assembled monolayers." In: *Nature Communications* 7 (1 Dec. 2016), p. 13904. DOI: 10.1038/ncomms13904.

[46] X. Chen, B. Kretz, F. Adoah, C. Nickle, X. Chi, X. Yu, E. del Barco, D. Thompson, D. A. Egger, and C. A. Nijhuis. "A single atom change turns insulating saturated wires into molecular conductors." In: *Nature Communications* 12 (1 June 2021), pp. 3432-1 - 3432–11. DOI: 10.1038/s41467-021-23528-8.

[47] Y. Liu, L. Ornago, M. Carlotti, Y. Ai, M. E. Abbassi, S. Soni, A. Asyuda, M. Zharnikov, H. S. V. D. Zant, and R. C. Chiechi. "Intermolecular Effects on Tunneling through Acenes in Large-Area and Single-Molecule Junctions." In: *Journal of Physical Chemistry C* 124 (41 Oct. 2020), pp. 22776–22783. DOI: 10.1021/acs.jpcc.0c05781.

[48] B. Huang et al. "Controlling and Observing Sharp-Valleyed Quantum Interference Effect in Single Molecular Junctions." In: *Journal of the American Chemical Society* 140 (50 Dec. 2018), pp. 17685–17690. DOI: 10.1021/jacs.8b10450.

[49] J. Bai et al. "Anti-resonance features of destructive quantum interference in single-molecule thiophene junctions achieved by electrochemical gating." In: *Nature Materials* 18 (4 Apr. 2019), pp. 364–369. DOI: 10.1038/s41563-018-0265-4.

[50] U. Rashid, W. Bro-Jørgensen, K. Harilal, P. Sreelakshmi, R. R. Mondal, V. C. Pisharam, K. N. Parida, K. Geetharani, J. M. Hamill, and V. Kaliginedi. "Chemistry of the Au-Thiol Interface through the Lens of Single-Molecule Flicker Noise Measurements." In: *Journal of the American Chemical Society* 146 (13 Apr. 2024), pp. 9063–9073. DOI: 10.1021/jacs.3c14079.

[51] S. Rodriguez-Gonzalez, Z. Xie, O. Galangau, P. Selvanathan, L. Norel, C. V. Dyck, K. Costuas, C. D. Frisbie, S. Rigaut, and J. Cornil. "HOMO Level Pinning in Molecular Junctions: Joint Theoretical and Experimental Evidence." In: *Journal of Physical Chemistry Letters* 9 (9 May 2018), pp. 2394–2403. DOI: 10.1021/acs.jpclett.8b00575.

[52] L. R. Ditzler, C. Karunatilaka, V. R. Donuru, H. Y. Liu, and A. V. Tivanski. "Electromechanical properties of self-assembled monolayers of tetrathiafulvalene derivatives studied by conducting probe atomic force microscopy." In: *Journal of Physical Chemistry C* 114 (10 Mar. 2010), pp. 4429–4435. DOI: 10.1021/jp9073834.

[53] Y. Fan, S. Tao, S. Pitié, C. Liu, C. Zhao, M. Seydou, Y. J. Dappe, P. J. Low, R. J. Nichols, and L. Yang. "Destructive quantum interference in meta-oligo(phenyleneethynylene) molecular wires with gold-graphene heterojunctions." In: *Nanoscale* 16 (1 Nov. 2023), pp. 195–204. DOI: 10.1039/d3nr04012g.

[54] A. Ismael, X. Wang, T. L. Bennett, L. A. Wilkinson, B. J. Robinson, N. J. Long, L. F. Cohen, and C. J. Lambert. "Tuning the thermoelectrical properties of anthracene-based self-assembled monolayers." In: *Chemical Science* 11 (26 July 2020), pp. 6836–6841. DOI: 10.1039/d0sc02193h.

[55] A. C. Aragonès, D. Aravena, F. J. Valverde-Muñoz, J. A. Real, F. Sanz, I. Díez-Pérez, and E. Ruiz. "Metal-Controlled Magnetoresistance at Room Temperature in Single-Molecule Devices." In: *Journal of the American Chemical Society* 139 (16 Apr. 2017), pp. 5768–5778. DOI: 10.1021/jacs.6b11166.

[56] S. Kumar, J. T. V. Herpt, R. Y. Gengler, B. L. Feringa, P. Rudolf, and R. C. Chiechi. "Mixed Monolayers of Spiropyrans Maximize Tunneling Conductance Switching by Photoisomerization at the Molecule Electrode Interface in EGaIn Junctions." In: *Journal of the American Chemical Society* 138 (38 Sept. 2016), pp. 12519–12526. DOI: 10.1021/jacs.6b06806.

[57] R. C. Chiechi, E. A. Weiss, M. D. Dickey, and G. M. Whitesides. "Eutectic Gallium–Indium (EGaIn): A Moldable Liquid Metal for Electrical Characterization of Self-Assembled Monolayers." In: *Angewandte Chemie International Edition* 47 (1 Jan. 2008), pp. 142–144. DOI: 10.1002/anie.200703642.

[58] H. Kang, J. Jang, G. D. Kong, S. Jung, T. Ohto, and H. J. Yoon. "Deposition condition impacts charge tunneling and thermoelectric properties of N-heterocyclic carbene monolayers." In: *Journal of Materials Chemistry A* 11 (30 July 2023), pp. 16233–16242. DOI: 10.1039/d3ta02443a.

[59] E. J. Lous, P. W. M. Blom, L. W. Molenkamp, and D. M. de Leeuw. "Formation of a Schottky barrier between eutectic Ga,In and thiophene oligomers." In: *Journal of Applied Physics* 81.8 (Apr. 1997), pp. 3537–3542. DOI: 10.1063/1.364990.

[60] H. B. Michaelson. "The work function of the elements and its periodicity." In: *Journal of Applied Physics* 48.11 (Nov. 1977), pp. 4729–4733. DOI: 10.1063/1.323539.

[61] W. P. Davey. "Precision Measurements of the Lattice Constants of Twelve Common Metals." In: *Phys. Rev.* 25 (6 June 1925), pp. 753–761. DOI: 10.1103/PhysRev.25.753.

Part I

APPENDIX

A

PUBLICATION 1

ACS NANOSCIENCE Au
AN OPEN ACCESS JOURNAL OF THE AMERICAN CHEMICAL SOCIETY

pubs.acs.org/nanoau
Article

Intermolecular Interactions and Quantum Interference Effects in Molecular Junctions

Louise O. H. Hyllested, Idunn Prestholm, and Gemma C. Solomon*

Cite This: https://doi.org/10.1021/acsnanoscienceau.4c00041
Read Online

ABSTRACT: Destructive quantum interference (DQI) leads to a decrease in the conductance of certain well-documented molecules. Experimental observations have revealed both direct and indirect manifestations of DQI, although a comprehensive understanding of the underlying causes of these distinct outcomes remains elusive. In both cases, DQI lowers the conductance, but only the direct case exhibits a characteristic V-shaped dip in differential conductance. Currently, the direct signature has exclusively been observed in monolayers and gated single-molecule systems. In this study, we employ density functional theory to elucidate a plausible explanation for the absence of a direct DQI signature in single molecules. Specifically, we attribute the direct DQI signature to a resonance shift induced by intermolecular interactions, which are absent in the individual molecules. By illustrating the impact of these intermolecular interactions, we emphasize the need for explicit treatment of intermolecular interactions when simulating monolayers.

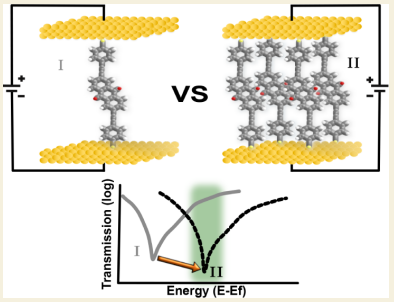

KEYWORDS: *quantum interference, self-assembled monolayer, conductance, density functional theory, charge transport.*

INTRODUCTION

Over the last 15 years, destructive quantum interference (DQI) effects have become accepted as an uncontroversial characteristic of electron transport through some classes of organic molecules, such as anthraquinone and oligo-(phenyleneethynylene) derivatives.[1−3]

When present, DQI hinders the flow of electrons across the molecule, resulting in the molecule exhibiting insulating properties. Similar to the phenomenon of destructive interference in water, DQI can be understood as a cancellation of waves. Despite its widespread presence in the literature, we still do not completely understand how this effect manifests in different molecular environments.

In general, DQI in molecules is observed as a suppressed conductance. In the most extreme case, complete suppression of the conductance could occur; however, in practice DQI results in incomplete suppression of the conductance and some low-level conductance is observed. In one of the earliest experimental reports of DQI in molecules, Guédon et al.,[4] described a "direct" signature of DQI as a V-shaped dip in the differential conductance (dI/dV). As also noted in that work, the absence of a V-shaped dip in dI/dV is not, however, an indication that DQI is absent but rather that it only manifests in a less definitive way as suppressed conductance. To distinguish between different observations of DQI, here we employ the terms "direct" and "indirect". The direct observation of DQI is characterized by the V-shaped dip in the dI/dV, while the indirect observation merely presents as suppressed conductance independent of line shape. This contrast is illustrated in Figure 1e,f.

Similar to experimental observations, the DQI can also be seen in calculated electronic transmission. In this context, DQI manifests as a dip in the transmission spectrum, which can be sharp or broad and may or may not be energetically aligned with the electrode Fermi energy. The direct signature in dI/dV will most clearly manifest in the case that DQI is leading to a sharp dip near the Fermi energy (Figure 1a). As the sharpness of the dip or the proximity to the Fermi energy decreases, the line shape of dI/dV will change and the system will eventually only exhibit an indirect signature (Figure 1d).

One way to study DQI in molecules is through molecular conductance experiments. These experiments typically focus on either monolayers or single molecules, where the primary distinction lies in the number of molecules involved and, consequently, the resulting molecular environment. When multiple molecules are present, the intermolecular interactions come into play alongside the inherent DQI exhibited by individual molecules.

Several single-molecule experiments have demonstrated the indirect signature of DQI as a general decrease in conductance

Received: July 19, 2024
Revised: September 23, 2024
Accepted: September 24, 2024

https://doi.org/10.1021/acsnanoscienceau.4c00041
ACS Nanosci. Au XXXX, XXX, XXX−XXX

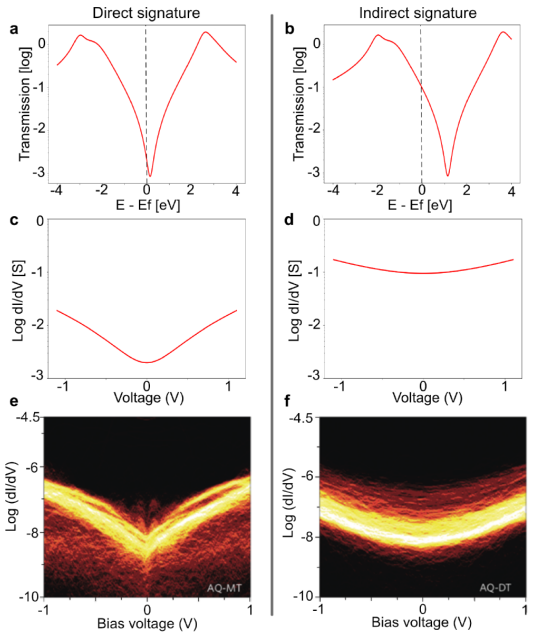

Figure 1. Illustration of transmission for the direct (a) and indirect (b) signatures of DQI. The shift is caused by a change in the onsite energies, from 0 eV in (a) to 1 eV in (b). (c,d) Corresponding dI/dV graphs for the direct (c) and indirect (d) signatures of DQI, respectively. a–d, was calculated using a Hückel model, see Section S1 for further details. (e,f) Experimental conductance measurements of AQ-MT (e) showing a V-shaped dip in the conductance associated with DQI. AQ-DT (f) exhibits a curve associated with either an indirect or no signature of DQI. Both graphs represent logarithmically binned histograms of dI/dV (in Ω^{-1}) versus bias voltage. (e,f) are reproduced with permission from Guédon et al.[4] Copyright 2023 Springer Nature.

without any distinct features.[5−8] In addition, Garner et al.[9] observed the indirect signature of DQI in single molecules, characterized by low conductance and high thermopower. However, direct signatures of DQI in single molecules have only been observed in experiments involving gated junctions.[10,11] The application of gating alters the molecular environment, causing a shift of the DQI into the measurable range. To the best of our knowledge, direct signatures of quantum interference without gating have solely been observed in ensemble junctions.[2,4,12−16] It is worth noting that although an overall low conductance can result from various factors, such as weak connections to the electrodes, a direct signature holds particular importance in confirming the presence of the DQI.

To gain a deeper understanding of the origin of DQI in experiments, theoretical calculations serve as a valuable tool. Theoretically, DQI can be observed in calculations, similar to experiments, as a V-shaped dip in the transmission spectrum, as illustrated in Figure 1a. In 2014, Lykkebo et al.[17] utilized the Hückel model to demonstrate that the interference feature in the transmission spectrum of a single molecule can be shifted by altering the onsite energy of the molecule. In these types of calculations, the transmission around the Fermi energy is the most important, as this region corresponds to what can be probed in experiments. To emphasize the significance of the position of the dip in the transmission spectrum, Figure 1 presents a theoretical depiction of the transmission spectrum and the differential conductance (dI/dV) with varying onsite energies.

As shown by Lykkebo et al., a shift in the onsite energy leads to a corresponding shift of the V-shaped dip in the transmission. This is illustrated by a Hückel model calculation example in Figure 1a,b (see Section S1 for further details). In Figure 1a, the dip aligns with the Fermi energy (0 eV), while, in Figure 1b, it occurs at a higher energy. Examining Figure 1c,d, the plots of dI/dV reveal that only a dip close to the Fermi energy (Figure 1a) results in a V-shaped dip in dI/dV (Figure 1c). By manipulating the onsite energy of the molecule in Hückel calculations, it is possible to shift the interference feature into the measurable range. This example illustrates the distinction between indirect and direct signatures of DQI. Indirect signatures exhibit a dip far from the Fermi energy, while direct signatures feature a dip in the transmission spectrum located at or near the Fermi energy, leading to a dip in the dI/dV. Given our understanding of how DQI can be observed, the question arises as to why the direct signature of DQI has only been detected in monolayers in ungated experiments.

In this study, we focus our investigation on a set of molecules with cross-conjugated and linearly conjugated structures, namely, anthracene-dithiol (AC-DT), anthraquinone-dithiol (AQ-DT), and anthraquinone-monothiol (AQ-MT), depicted in Figure 2. Previous experimental studies[4] have

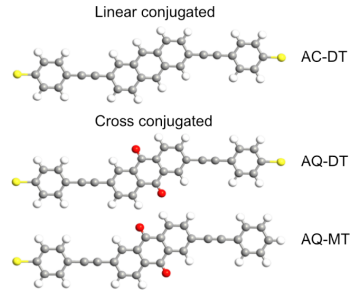

Figure 2. Chemical structures of the molecules included in the study; two cross-conjugated molecules: dithiolated anthraquinone and monothiolated anthraquinone (AQ-DT, AQ-MT) and one linearly conjugated molecule: dithiolated anthracene (AC-DT).

revealed both indirect and direct signatures of DQI in AQ-DT and AQ-MT, respectively. Given that these molecules possess DQI as single entities due to their cross-conjugated nature,[18] they serve as excellent candidates for exploring the influence of intermolecular interactions on DQI.

MODEL SYSTEM

To begin our study, we utilized a simple model based on Hückel theory. Since direct signature of DQI has only been observed for monolayers[4,12−16] and gated single-molecule experiments,[10,11] it is likely that molecular interactions play a role in determining whether there is a direct or indirect signature of DQI. To investigate this further, we employ a Hückel model that incorporates two ethene molecules, either

https://doi.org/10.1021/acsnanoscienceau.4c00041
ACS Nanosci. Au XXXX, XXX, XXX−XXX

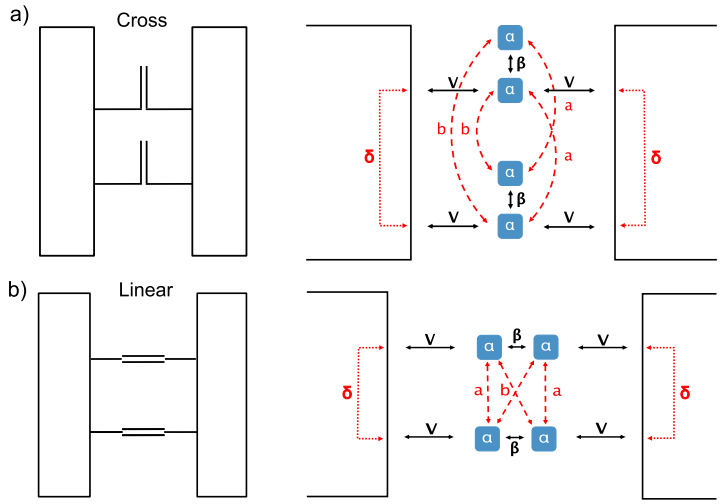

Figure 3. A schematic of the two-molecule linear and cross-conjugated tight-binding model systems, illustrating the various interactions. (a) Two cross-conjugated 2 site molecules. (b) Two linearly conjugated 2 site molecules. α represents the onsite energy. Arrows indicate the interactions, where β denotes the overlap integral between neighboring sites, and a and b represent the intermolecular interaction integrals. V corresponds to the coupling to the electrode, and δ is a single parameter that characterizes the through-electrode intermolecular interaction. It should be noted that δ does not correspond to a simple overlap integral. The intermolecular interactions are highlighted with red dashed arrows.

cross-conjugated (resulting in DQI) or linearly conjugated (resulting in no DQI), coupled to leads.

The choice of molecules for the model system is primarily aimed at maximizing simplicity while retaining the capability to model molecular interactions effectively. The minimal model for a cross-conjugated system, like the AQ family of molecules, is two sites where one site is connected to both electrodes and the other is connected to neither as in Figure 3a. The minimal model for a comparative linearly conjugated system is two sites where each site is connected to a single electrode, as shown in Figure 3b. To probe the effects of intermolecular interactions, we need to consider the different ways these two sites can couple to neighboring molecules. Consequently, it is essential to include two molecules in the model. In this setup, both molecules are connected to the leads. If we imagine these to be models of organic molecules, we could consider these to be ethene molecules connected directly to the leads.

Figure 3 depicts a schematic representation of the cross-conjugated system (Figure 3a) and the linear system (Figure 3b). All interactions included in the models are shown as arrows, where α is the onsite energy, β is the overlap integral and a and b are the intermolecular interaction integrals, highlighted as the red dashed arrows. In the model, each alpha corresponds to a carbon atom in the ethene molecules. Since each ethene molecule consists of two carbon atoms, there are two alphas in both cases. In the linear setup, each carbon in the ethene molecule is connected to one lead. However, in the cross-conjugated setup, only one carbon in each ethene molecule is connected to both leads

The Hamiltonians of the molecules in the two configurations are identical, and read

$$\mathbf{H} = \begin{bmatrix} \alpha & \beta & b & a \\ \beta & \alpha & a & b \\ b & a & \alpha & \beta \\ a & b & \beta & \alpha \end{bmatrix} \tag{1}$$

where α is the onsite energy, β is the overlap integral between neighboring sites, and a and b are intermolecular interaction integrals. Within a coherent tunneling formalism, the zero-bias transmission through a molecular wire at zero temperature is given as

$$T(\varepsilon) = \mathrm{Tr}\{\mathbf{\Gamma}^L \mathbf{G}(\varepsilon) \mathbf{\Gamma}^R \mathbf{G}^\dagger(\varepsilon)\} \tag{2}$$

Here, the retarded Green's function, $G(\varepsilon)$, is defined as

$$G(\varepsilon) = [\varepsilon \mathbf{I} - \mathbf{H} + \frac{i}{2}\mathbf{\Gamma}^L + \frac{i}{2}\mathbf{\Gamma}^R]^{-1} \tag{3}$$

Where ε is the energy and $\mathbf{I}$ is the unit matrix. $\mathbf{\Gamma}^L$and $\mathbf{\Gamma}^R$ describe the broadening of the molecular resonances caused by the coupling to the leads, V. Additionally, we consider the inclusion of through-electrode intermolecular interaction, represented as δ. Yaliraki and Ratner[19] have demonstrated that this interaction has an impact on the conductance when the molecules are in close proximity to each other, specifically at a distance equivalent to the unit lattice distance. The self-energies for the cross-conjugated model system (Figure 3a) read

$$\mathbf{\Gamma}^L = \mathbf{\Gamma}^R = \begin{bmatrix} V^2 & 0 & 0 & \delta \\ 0 & 0 & 0 & 0 \\ 0 & 0 & 0 & 0 \\ \delta & 0 & 0 & V^2 \end{bmatrix} \tag{4}$$

and for the linearly conjugated model system (Figure 3b),

https://doi.org/10.1021/acsnanoscienceau.4c00041
ACS Nanosci. Au XXXX, XXX, XXX−XXX

$$\mathbf{\Gamma}^L = \begin{bmatrix} V^2 & 0 & 0 & \delta \\ 0 & 0 & 0 & 0 \\ 0 & 0 & 0 & 0 \\ \delta & 0 & 0 & V^2 \end{bmatrix}, \quad \mathbf{\Gamma}^R = \begin{bmatrix} 0 & 0 & 0 & 0 \\ 0 & V^2 & \delta & 0 \\ 0 & \delta & V^2 & 0 \\ 0 & 0 & 0 & 0 \end{bmatrix} \tag{5}$$

The total current through the system can then be calculated as

$$I = \frac{2e}{h} \int_{-\infty}^{\infty} d\varepsilon [f_L - f_R] T(\varepsilon) \tag{6}$$

where $[f_L - f_R]$ refers to the Fermi Dirac distribution for the left and right electrode and $T(\varepsilon)$ is the zero bias transmission shown in eq 2. From the total current, the zero-bias differential conductance can also be obtained by differentiation with voltage (see SI for further details).

The transmissions for the two models, considering different parameter choices, are depicted in Figure 4. To gain a deeper understanding of these results, it is necessary to examine the molecular systems in detail. The Hamiltonian has the following eigenvalues:

$$\begin{aligned} \varepsilon_1 &= \alpha + \beta - b + a, \\ \varepsilon_2 &= \alpha + \beta + b - a, \\ \varepsilon_3 &= \alpha - \beta - b - a, \\ \varepsilon_4 &= \alpha - \beta + b + a. \end{aligned} \tag{7}$$

Examining the eigenvalues provides insight into the energetic locations of the resonances in the transmission spectrum. The eigenvalues exhibit a splitting of both the occupied orbitals, ε_1 and ε_2, as well as the unoccupied orbitals, ε_3 and ε_4, when intermolecular interactions a and b are taken into account. As the values of a and b approach zero, the eigenvalues become degenerate pairs, indicating the behavior of two noninteracting molecules. This observation highlights the influence of intermolecular interactions on the electronic structure and the resonance behavior in the system.

Figure 4 presents the transmission for the linearly conjugated model systems (Figure 4a,b) and the cross-conjugated model system (Figure 4c). Both model system calculations were performed with β as −2.7 eV and α as 0 eV. The colors in the figure indicate the degree of interaction between the two molecules. The black dashed-dotted line corresponds to no interaction (a, b = 0 eV, 0 eV), representing two isolated single molecules (SM). The purple dashed line represents weak interactions (a, b = −0.1 eV, −0.05 eV), resembling two molecules with weak intermolecular interactions, while the orange solid line indicates strong interactions (a, b = −0.2 eV, −0.1 eV), resembling two molecules with strong intermolecular interactions. The purpose of illustrating weak (purple) and strong (orange) interactions is to show a sparsely packed monolayer (M) and a densely packed monolayer (DM), respectively.

The transmission through the linearly conjugated ethene system (Figure 4a,b) reveals a splitting of the molecular resonances when the coupling to the electrodes is set to a sufficiently small value, V = −0.2 eV, and δ = 0.0 eV^2 (Figure 4a). However, when the coupling is strengthened to V = −1.0 eV and δ = 0.2 eV^2, the molecular resonances become broadened, resulting in the disappearance of peak splitting (Figure 4b). Similar behavior can be observed for the resonant characteristics of the cross-conjugated ethene model system (see Figures S2 and S3). This observation aligns with the findings of Obersteiner et al.,[20] who previously reported the splitting of molecular resonances in clusters comprising only two molecules.

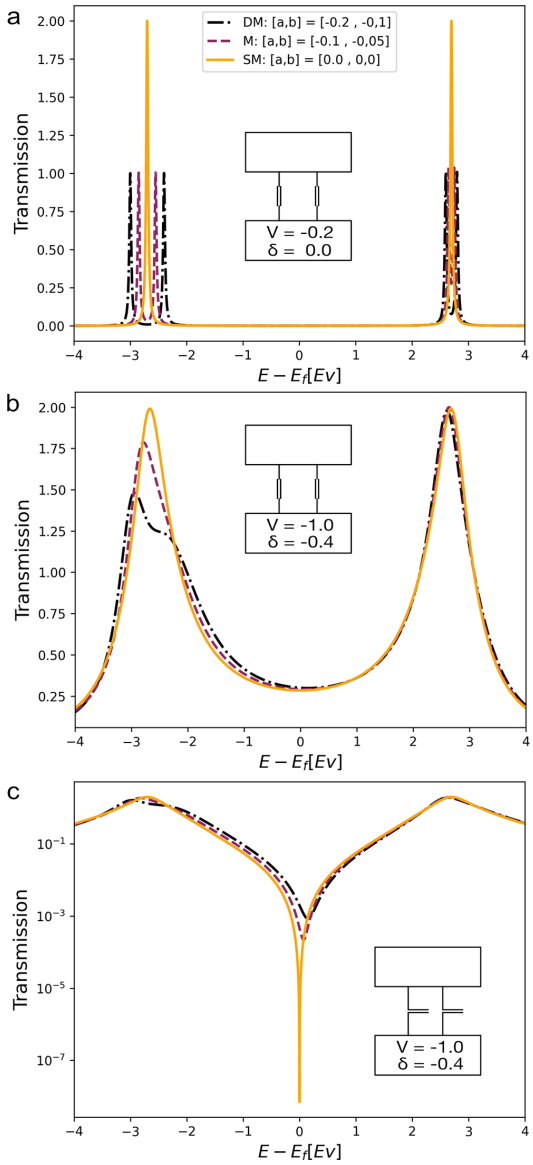

Figure 4. Energy-dependent zero-bias transmission for the linearly conjugated (a,b) and cross-conjugated (c) model systems in a strongly coupled configuration (b,c) and a weakly coupled configuration (a). The colors indicate whether the two molecules are non-interacting (black dashed−dotted line), corresponding to two isolated molecules, weakly interacting (purple dashed line), corresponding to a sparse monolayer, or strongly interacting (orange solid line) corresponding to a dense monolayer. The transmission in (c) is plotted on a logarithmic scale to highlight the effects on the antiresonance.

The linearly conjugated system cannot give us any indication of the effects of intermolecular interaction on DQI, however, in

https://doi.org/10.1021/acsnanoscienceau.4c00041
ACS Nanosci. Au XXXX, XXX, XXX−XXX

Figure 4c, a noticeable dip in conductance at the Fermi energy is apparent for the cross-conjugated system.

In these model system calculations we can solve for values of energy (E) where the transmission goes to zero, and find it is purely real for noninteracting molecules in the junction. However, when we include intermolecular interactions in the Hamiltonian and self-energies, this solution becomes imaginary. Depending on the strength of the interaction, the transmission zero moves deeper into the complex plane, and consequently, the dip on the real axis becomes less pronounced (For further information, see SI). We note here that it would be interesting to have a physical interpretation for this result, but at this stage, we only have a mathematical observation.

From these calculations we conclude that both a depth reduction and shift of the antiresonance could be observed when intermolecular interactions are present. The shift in the destructive interference feature occurs due to a change in the relative positions of the HOMO and LUMO at different interaction strengths, which is a consequence of the asymmetric shift of the resonances.

Up to this point, the model has not taken into account any electrostatic interactions, and therefore, no uniform resonance shifts across the full spectrum have been observed. In actual molecular junctions, electrostatic effects arise from local dipoles associated with the linker groups, leading to changes in the local electrostatic environment.[21] To incorporate this effect into the model, the on-site energies, denoted as α, can be shifted. This shift in α results in a corresponding shift in the transmission spectrum, as depicted in Figure 5a. Here, the transmission of the dense monolayer is plotted for different α values: 0.0, 0.5, and 1.0. It is worth noting that the shift in transmission and the position of the antiresonance significantly influence the line shape of the conductance, as demonstrated in Figure 5b. When an antiresonance in the transmission approaches the Fermi level, a sharp dip in the conductance occurs. The magnitude of this conductance dip depends on the depth and location of the antiresonance in the transmission, given that the conductance is calculated based on the transmission at the Fermi energy.

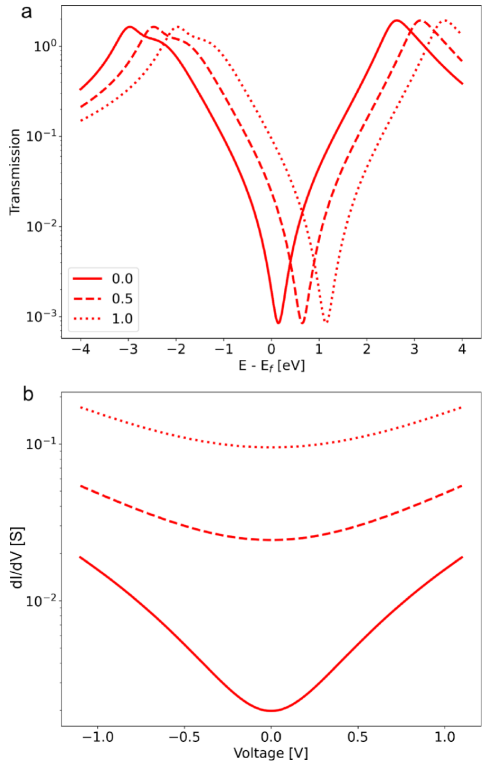

Figure 5. Energy-dependent zero-bias transmission (a) and corresponding dI/dV curves (b) for the cross-conjugated model system. The calculations are performed at different onsite energies: 0.0, 0.5, and 1.0. The figure emphasizes the sensitivity of dI/dV to the position and depth of the antiresonance in the transmission. The $I-V$ traces are calculated from the energy-dependent zero-bias transmission function according to eq 6, and the dI/dV traces are obtained from differentiation of the $I-V$ curves.

ATOMISTIC CALCULATIONS

Following the model system, we extended our investigation to include three conjugated molecules, namely, AQ-MT, AQ-DT, and AC-DT, which were incorporated into an Au−molecule−Au junction (Figures S4 and S5). Our interest was focused on understanding how the interactions between these molecules would impact the electronic transmission. To guide our study, we drew inspiration from the work conducted by Obersteiner et al.[20] They investigated charge transport through molecular clusters that do not exhibit interference and observed a highly nonlinear current behavior as the clusters increased in size. They attributed this behavior to the collective electrostatic effects originating from the dipoles associated with the binding groups. Their work emphasized the significant influence of the transition from a single molecule to a cluster on the overall current. Motivated by their findings, we probe the impact of intermolecular interactions on the transition from single molecules to monolayers in systems with DQI.

We calculate the transmission for various junction configurations, ranging from a single molecule (SM) to clusters consisting of 4 (C4), 6 (C6), and 9 (C9) molecules as well as dense monolayer (DM) and sparse monolayer (M) configurations. For the monolayer calculations, we treated the system as one molecule within a small unit cell and applied periodic boundary conditions. Additionally, we conducted calculations for a sparse monolayer junction with 4 molecules included explicitly in the unit cell, representing the same density as the one-molecule sparse monolayer configuration.

Figure 6 provides an illustration of the different junction configurations with the top electrode removed for clarity. The dots in the figure indicate the positions of the binding group, while the lines represent the size of the unit cell for each junction configuration. In Figure 6a, the solid red line represents a densely packed monolayer consisting of a single molecule on a 2 × 2 Au FCC(111) electrode. In addition, the dotted red line represents a sparse monolayer, consisting of one molecule on a (3 × 3) Au FCC(111) electrode. For the single molecule and cluster configurations, we modeled the systems with 1 (4, 6, or 9) molecule(s) on a (9 × 9) Au FCC(111) electrode.

The molecules in the junctions are positioned at every second FCC hollow sites, resulting in a distance of 5.77 Å between the sulfur atoms of neighboring molecules. This arrangement leads to different molecular coverages for each configuration: SM (single molecule) has a coverage of $\frac{1}{16}$, C4

https://doi.org/10.1021/acsnanoscienceau.4c00041
ACS Nanosci. Au XXXX, XXX, XXX−XXX

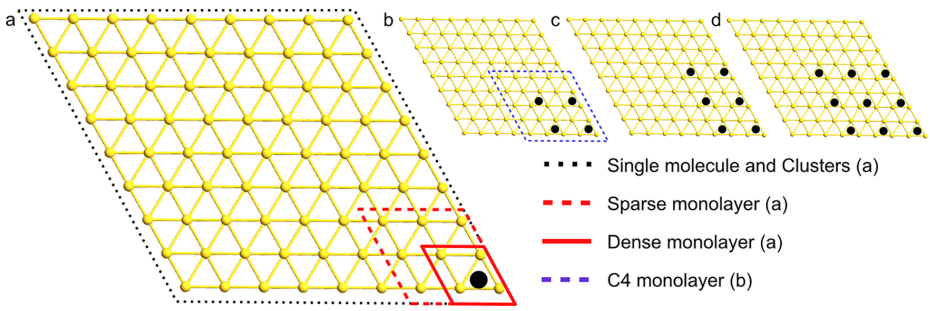

Figure 6. Illustration of the different junction configurations. The top gold electrode is removed for clarity. The black dots represent a molecule location, while the dotted/solid lines represent the different electrode size. If no line is present, the electrode is the size of the entire Au surface. The single molecules and clusters are all added to a 9 × 9 Au electrode. The following configurations are depicted: (a) Single molecule (SM) and dense (DM)/sparse (M) monolayer. The single molecule electrode is shown as a dotted black line. The dense and sparse monolayer electrodes are the solid and dotted red line, respectively. The single molecule is on a 9 × 9 Au electrode, whereas the sparse and dense monolayer consists of a single molecule on a 2 × 2 and 3 × 3 Au electrode, respectively. (b) Four-molecule cluster (C4) and four-molecule monolayer (C4M): The electrode of the C4 monolayer is indicated by a dotted line (5 × 5 Au electrode). (c) 6 molecule cluster (C6). (d) 9 molecule cluster (C9).

(cluster of 4 molecules) has a coverage of $\frac{4}{16}$, C6 (cluster of 6 molecules) has a coverage of $\frac{6}{16}$, and C9 (cluster of 9 molecules) has a coverage of $\frac{9}{16}$. It is worth noting that our chosen molecular coverage differs from that used by Obersteiner et al., as they employed a smaller electrode, which resulted in closer proximity of the molecules in their junctions. Illustrations of the molecular density for SM, C4, C6, and C9 can be found in Figure 6a–d, respectively.

To simulate a sparse monolayer junction with 4 molecules (C4M), we selected a (5 × 5) Au FCC(111) electrode with 4 molecules in the junction. This choice was made to mimic the density of the single-molecule sparse monolayer. From this point onward, we will refer to this configuration as the C4 monolayer (C4M). Further details regarding the calculation setup can be found in Section S2).

To investigate how the molecular environment affects the transmission, we calculated the transmission per molecule for each junction configuration, ranging from a single molecule to a dense monolayer. We were particularly interested in examining the impact of the electrostatic interactions, which we knew from the model system would result in a resonance shift. The results of these calculations are presented in Figure 7. In each plot, the triangular marks show the lowest transmission value for each system, and a vertical line is included to highlight their position on the energy axis. The corresponding transmission spectra for each junction setup are shown in the same colors but faded in the background. For the linear-conjugated molecule AC-DT (Figure 7a), no DQI features are observed in the transmission. This aligns with our expectations based on the model system. In contrast, when examining the cross-conjugated molecules AQ-DT and AQ-MT (Figure 7b,c, respectively), DQI features are observed in the transmission spectra, and they are shifted toward higher energy with intermolecular interactions. These observations are consistent with our model system predictions. We cannot definitively determine why the energy of the single molecule junctions exhibits an antiresonance at a specific position. However, we can assert that the energy of the system is influenced by intermolecular interactions, which become apparent when more molecules are added to the junction.

The transmission decreases going from AC-DT to AQ-DT and further to AQ-MT. This reduction in transmission is first due the absence/presence of DQI but can be partially attributed to the variations in the binding groups utilized. AC-DT and AQ-DT both feature sulfur (S) as the binding group on both sides of the molecule, and it is widely acknowledged in the literature that sulfur and gold exhibit a strong interaction.[22] On the other hand, AQ-MT incorporates a sulfur binding group on one side and a hydrogen atom on the other side, resulting in weaker coupling between one side of the molecule and the electrode.

While the difference in binding group contributes slightly to the change in transmission, the primary factor contributing to the overall decrease in transmission is the presence of DQI. In addition to the evident dip in the transmission spectrum, DQI further diminishes the transmission compared with that of the linearly conjugated molecule.

First, examining the magnitude of the transmission per molecule for the cross-conjugated molecules AQ-DT and AQ-MT, we see that both the single molecule (SM) and the sparse monolayer (M) exhibit similar low levels of transmission at their minima (triangles). Given this similarity in minimum transmission levels and the absence of intermolecular interactions in a single molecule, it suggests that the primary factor responsible for the dip shift lies within the molecular environment.

Since we cannot entirely dismiss the possibility of electrode effects, we calculated the electrostatic difference potential (EDP) (see Supporting Information). This calculation allows us to examine how the charge rearrangement in the junction changes the potential. We do observe a charge rearrangement at the electrode–molecule interface, with the molecule becoming increasingly negatively charged as the number of molecules in a cluster or the density of the monolayer increases. These types of charge rearrangements will certainly result in orbital energy shifts, although we cannot quantify to what extent this affects the shift of the interference feature. We emphasize that the electrodes are periodic for all systems, with additional gold atoms added for the cluster calculations to minimize cluster–cluster interactions. Essentially, the cluster calculations represent dilute monolayers of clusters.

https://doi.org/10.1021/acsnanoscienceau.4c00041
ACS Nanosci. Au XXXX, XXX, XXX–XXX

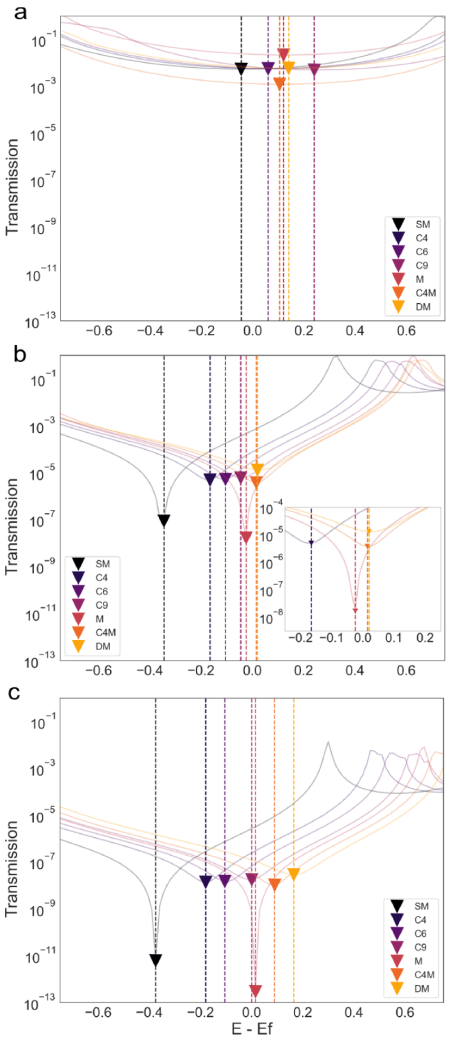

Figure 7. Energy-dependent zero-bias transmission spectra for each molecule: AC-DT (a), AQ-DT (b), and AQ-MT (c), calculated with DFT. In each spectrum, the marks highlight the lowest point of transmission. Additionally, the shifts in the transmission features are emphasized by vertical dashed lines, providing visual cues for the changes in the transmission characteristics.

To further investigate the effect of the molecular environment, we can examine the calculations for the C4 monolayer (C4M), which represents a molecular density equivalent to that of a sparse monolayer (one molecule on a 3 × 3 Au electrode). If the complete influence of the molecular environment is accounted for in the sparse monolayer (M), the transmission spectra of the sparse monolayer (M) and the C4 monolayer (C4M) should be identical. Conversely, if the two curves diverge, it would indicate a deviation due to the molecular environment.

In Figure 7b (AQ-DT), the inset provides a magnified view of the transmission spectra for the four-cluster (C4), C4 monolayer (C4M), sparse monolayer (M), and dense monolayer (DM) configurations. This illustration serves to highlight that the C4 monolayer (C4M) and sparse monolayer (M) are not identical. This disparity indicates that when modeling a monolayer with a single molecule and periodic boundary conditions (M), some information regarding molecular interactions is lost. Furthermore, the 4 cluster (C4) and C4 monolayer (C4M) possess the same features. The resonance is merely shifted as a result of the change in the molecular environment when we shift from a small cluster of molecules to a monolayer junction.

The dense monolayer (DM) exhibits a transmission curve that resembles the clusters but with a higher overall transmission. In the case of AQ-MT (Figure 7c), the dense monolayer (DM) also undergoes a further energy shift upward. This suggests that unsurprisingly, the dense monolayer (DM) experiences stronger interactions with the surrounding molecules compared to the sparse monolayer (M). However, whether the molecules would pack together so densely in an experimental scenario remains to be determined. These findings emphasize the critical importance of simulating junctions as accurately as possible when considering intermolecular interactions. By capturing the realistic molecular environment, we can obtain a more comprehensive understanding of the transmission behavior and its dependence on molecular packing.

It is important to note that the atomistic calculations do not allow us to distinguish between electrostatic effects and screening effects from neighboring molecules. Therefore, it is challenging to definitively conclude whether screening plays a role in the observed DQI without further investigation or experimental validation. However, it is worth noting that even if screening does influence DQI, its impact ultimately stems from the molecular environment.

To establish a comparison with experimental measurements, we focused on calculating the differential conductance based on the transmission at the Fermi energy for both the single-molecule (SM) and the C4 monolayer (C4M) of AQ-DT and AQ-MT. Figure 8 illustrates the transmission (Figure 8a) and the corresponding differential conductance (Figure 8b) for AQ-DT and AQ-MT. As observed, similar to the model system, the C4 monolayer (C4M) exhibits a dip in both the transmission near the Fermi energy and the differential conductance. Conversely, the single molecule (SM), which displays a sharp dip at lower energies in the transmission, does not show a corresponding dip in the differential conductance. These results highlight the significance of the DQI position within the transmission spectrum in determining whether a clear direct signature of DQI is experimentally observed in the differential conductance.

It is crucial to acknowledge the caveats regarding the molecular environment. This could arise from using a single molecule calculation to interpret a monolayer experiment, uncertainties in monolayer density or packing, or the potential influence of additional molecules on what would be considered a single molecule. In all cases, the exact energetic position of the antiresonance dips cannot be known precisely, and the correspondence between theory and experiments must be interpreted accordingly. However, by analyzing trends present in the calculations, we can gain valuable insights into the behavior of different molecules.

https://doi.org/10.1021/acsnanoscienceau.4c00041
ACS Nanosci. Au XXXX, XXX, XXX−XXX

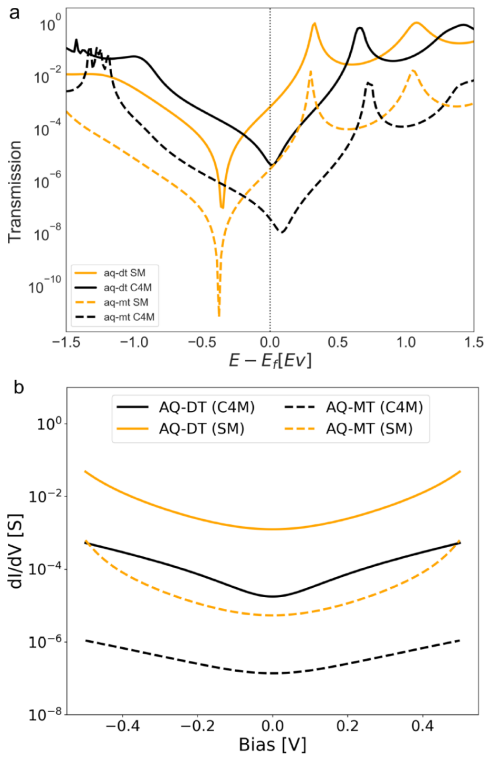

Figure 8. Zero-bias transmission spectra of AQ-DT (solid line) and AQ-MT (dashed line) in both single molecule and C4 monolayer junction configurations (a). The color scheme distinguishes between the calculation performed on a single molecule (SM, indicated by orange) and a C4 monolayer (C4M, indicated by black). Simulated dI/dV traces (b) were calculated from the zero-bias transmission function. These dI/dV traces are obtained through differentiation of the integrated transmission function, as specified by eq 6.

CONCLUSION

This work presents a comprehensive investigation of a group of molecules with and without DQI and the role of intermolecular interactions in controlling the observed transport properties. The key findings emphasize the influence of the molecular environment on the presence and manifestation of DQI. Shifting from single molecules to monolayers, which alters the molecular interactions within the junction, can lead to a shift of an antiresonance toward higher energy. This explains why single molecules may not exhibit a direct signature of DQI in experimental measurements even if this is observed in monolayers measurements. Additionally, the study highlights the significance of considering intermolecular interactions in simulating junctions. The results demonstrate that the transmission can be significantly impacted when transitioning from a one-molecule junction to a junction with four molecules while maintaining the same molecular density and applying periodic boundary conditions. By advancing our understanding of how intermolecular interactions affect properties, such as DQI, this work provides guidelines for best practice for calculations of monolayer experiments and the interpretation of agreement, or lack thereof, between calculations, single-molecule experiments, and monolayer experiments on the same molecule.

METHOD

The calculations were conducted by using density functional theory (DFT) combined with the Greens function approach and the Landauer formula to determine the transmission and conductance. QuantumATK (version S-2021.06-SP1)[23−25] was employed for these calculations, utilizing the GGA PBE functional.[26,27] A double-ζ basis set (with a single-ζ on Au) and polarization functions on all molecular atoms were used along with periodic boundary conditions. Additionally, noncovalent interactions were accounted for by incorporating the Grimme DFT D3 dispersion correction.[28] Further details regarding the calculations can be found in the Supporting Information.

ASSOCIATED CONTENT

Supporting Information

The Supporting Information is available free of charge at https://pubs.acs.org/doi/10.1021/acsnanoscienceau.4c00041.

Atomistic calculations details. Additional model system calculations, including figures of the cross conjugated system strongly coupled, the cross conjugated system weakly coupled, and the linear conjugated system strongly coupled (on a logarithmic scale). Explanation of the differentiation of the total current. Calculated energy at the transmission minimas of the model system. Electrostatic difference potential (EDP) (PDF)

AUTHOR INFORMATION

Corresponding Author

Gemma C. Solomon − *Department of Chemistry and Nano-Science Center, University of Copenhagen, Copenhagen 2100, Denmark; NNF Quantum Computing Programme, Niels Bohr Institute, University of Copenhagen, Copenhagen 2100, Denmark;* orcid.org/0000-0002-2018-1529; Email: gsolomon@chem.ku.dk

Authors

Louise O. H. Hyllested − *Department of Chemistry and Nano-Science Center, University of Copenhagen, Copenhagen 2100, Denmark;* orcid.org/0000-0002-1701-0438

Idunn Prestholm − *Department of Chemistry and Nano-Science Center, University of Copenhagen, Copenhagen 2100, Denmark*

Complete contact information is available at: https://pubs.acs.org/10.1021/acsnanoscienceau.4c00041

Author Contributions

CRediT: **Louise Oxen Høgh Hyllested** conceptualization, data curation, formal analysis, methodology, project administration, visualization, writing - original draft, writing - review & editing; **Idunn Prestholm** conceptualization, data curation, formal analysis, methodology, visualization, writing - original draft, writing - review & editing; **Gemma C. Solomon** conceptualization, funding acquisition, methodology, supervision, writing - review & editing.

Notes

The authors declare no competing financial interest.

https://doi.org/10.1021/acsnanoscienceau.4c00041
ACS Nanosci. Au XXXX, XXX, XXX−XXX

■ ACKNOWLEDGMENTS

We would like to acknowledge the European Research Council (ERC) for their generous funding of this project under the European Union's Horizon 2020 research and innovation programme (grant agreement No. 865870). Additionally, we would like to acknowledge the use of ChatGPT for its assistance in making grammatical corrections throughout the writing process.

■ REFERENCES

(1) Arroyo, C. R.; Tarkuc, S.; Frisenda, R.; Seldenthuis, J. S.; Woerde, C. H. M.; Eelkema, R.; Grozema, F. C.; Van Der Zant, H. S. Signatures of quantum interference effects on charge transport through a single benzene ring. *Angew. Chem., Int. Ed.* **2013**, *52*, 3152−3155.

(2) Liu, Y.; Ornago, L.; Carlotti, M.; Ai, Y.; El Abbassi, M.; Soni, S.; Asyuda, A.; Zharnikov, M.; van der Zant, H. S. J.; Chiechi, R. C. Intermolecular Effects on Tunneling through Acenes in Large-Area and Single-Molecule Junctions. *J. Phys. Chem. C* **2020**, *124*, 22776−22783.

(3) Zotti, L. A.; Leary, E. Taming quantum interference in single molecule junctions: Induction and resonance are key. *Phys. Chem. Chem. Phys.* **2020**, *22*, 5638−5646.

(4) Guédon, C. M.; Valkenier, H.; Markussen, T.; Thygesen, K. S.; Hummelen, J. C.; Van Der Molen, S. J. Observation of quantum interference in molecular charge transport. *Nat. Nanotechnol.* **2012**, *7*, 305.

(5) Aradhya, S. V.; Meisner, J. S.; Krikorian, M.; Ahn, S.; Parameswaran, R.; Steigerwald, M. L.; Nuckolls, C.; Venkataraman, L. Dissecting contact mechanics from quantum interference in single-molecule junctions of stilbene derivatives. *Nano Lett.* **2012**, *12*, 1643−1647.

(6) Arroyo, C. R.; Tarkuc, S.; Frisenda, R.; Seldenthuis, J. S.; Woerde, C. H.; Eelkema, R.; Grozema, F. C.; van der Zant, H. S. Signatures of quantum interference effects on charge transport through a single benzene ring. *Angew. Chem.* **2013**, *125*, 3234−3237.

(7) Liu, X.; Sangtarash, S.; Reber, D.; Zhang, D.; Sadeghi, H.; Shi, J.; Xiao, Z.-Y.; Hong, W.; Lambert, C. J.; Liu, S.-X. Gating of quantum interference in molecular junctions by heteroatom substitution. *Angew. Chem., Int. Ed.* **2017**, *56*, 173−176.

(8) Ballmann, S.; Härtle, R.; Coto, P. B.; Elbing, M.; Mayor, M.; Bryce, M. R.; Thoss, M.; Weber, H. B. Experimental evidence for quantum interference and vibrationally induced decoherence in single-molecule junctions. *Phys. Rev. Lett.* **2012**, *109*, 056801.

(9) Garner, M. H.; Li, H.; Chen, Y.; Su, T. A.; Shangguan, Z.; Paley, D. W.; Liu, T.; Ng, F.; Li, H.; Xiao, S.; et al. Comprehensive suppression of single-molecule conductance using destructive σ-interference. *Nature* **2018**, *558*, 415−419.

(10) Huang, B.; Liu, X.; Yuan, Y.; Hong, Z. W.; Zheng, J. F.; Pei, L. Q.; Shao, Y.; Li, J. F.; Zhou, X. S.; Chen, J. Z.; Jin, S.; Mao, B. W. Controlling and Observing Sharp-Valleyed Quantum Interference Effect in Single Molecular Junctions. *J. Am. Chem. Soc.* **2018**, *140*, 17685−17690.

(11) Bai, J.; et al. Anti-resonance features of destructive quantum interference in single-molecule thiophene junctions achieved by electrochemical gating. *Nat. Mater.* **2019**, *18*, 364−369.

(12) Zhang, Y.; Ye, G.; Soni, S.; Qiu, X.; Krijger, T. L.; Jonkman, H. T.; Carlotti, M.; Sauter, E.; Zharnikov, M.; Chiechi, R. C. Controlling destructive quantum interference in tunneling junctions comprising self-assembled monolayers via bond topology and functional groups. *Chem. Sci.* **2018**, *9*, 4414−4423.

(13) Fracasso, D.; Valkenier, H.; Hummelen, J. C.; Solomon, G. C.; Chiechi, R. C. Evidence for quantum interference in SAMs of arylethynylene thiolates in tunneling junctions with eutectic Ga−In (EGaIn) top-contacts. *J. Am. Chem. Soc.* **2011**, *133*, 9556−9563.

(14) Rabache, V.; Chaste, J.; Petit, P.; Della Rocca, M. L.; Martin, P.; Lacroix, J.-C.; McCreery, R. L.; Lafarge, P. Direct observation of large quantum interference effect in anthraquinone solid-state junctions. *J. Am. Chem. Soc.* **2013**, *135*, 10218−10221.

(15) Carlotti, M.; Kovalchuk, A.; Wächter, T.; Qiu, X.; Zharnikov, M.; Chiechi, R. C. Conformation-driven quantum interference effects mediated by through-space conjugation in self-assembled monolayers. *Nat. Commun.* **2016**, *7*, 13904.

(16) Chen, X.; Kretz, B.; Adoah, F.; Nickle, C.; Chi, X.; Yu, X.; Del Barco, E.; Thompson, D.; Egger, D. A.; Nijhuis, C. A. A single atom change turns insulating saturated wires into molecular conductors. *Nat. Commun.* **2021**, *12*, 3432.

(17) Lykkebo, J.; Gagliardi, A.; Pecchia, A.; Solomon, G. C. IETS and quantum interference: Propensity rules in the presence of an interference feature. *J. Chem. Phys.* **2014**, *141*, 124119.

(18) Solomon, G. C.; Herrmann, C.; Hansen, T.; Mujica, V.; Ratner, M. A. Exploring local currents in molecular junctions. *Nat. Chem.* **2010**, *2*, 223−228.

(19) Yaliraki, S. N.; Ratner, M. A. Molecule-interface coupling effects on electronic transport in molecular wires. *J. Chem. Phys.* **1998**, *109*, 5036−5043.

(20) Obersteiner, V.; Huhs, G.; Papior, N.; Zojer, E. Unconventional Current Scaling and Edge Effects for Charge Transport through Molecular Clusters. *Nano Lett.* **2017**, *17*, 7350−7357.

(21) Obersteiner, V.; Egger, D. A.; Heimel, G.; Zojer, E. Impact of collective electrostatic effects on charge transport through molecular monolayers. *J. Phys. Chem. C* **2014**, *118*, 22395−22401.

(22) Bain, C. D.; Troughton, E. B.; Tao, Y. T.; Evall, J.; Whitesides, G. M.; Nuzzo, R. G. Formation of monolayer films by the spontaneous assembly of organic thiols from solution onto gold. *J. Am. Chem. Soc.* **1989**, *111*, 321−335.

(23) Synopsis *QuantumATK version S-2021.06-SP1*. www.synopsys.com/silicon/quantumatk.html, Accessed 2023 February 6.

(24) Soler, J. M.; Artacho, E.; Gale, J. D.; García, A.; Junquera, J.; Ordejón, P.; Sánchez-Portal, D. The SIESTA method for ab initio order-N materials simulation. *J. Phys.: Condens. Matter* **2002**, *14*, 2745.

(25) Brandbyge, M.; Mozos, J.-L.; Ordejón, P.; Taylor, J.; Stokbro, K. Density-functional method for nonequilibrium electron transport. *Phys. Rev. B* **2002**, *65*, 165401.

(26) Burke, K.; Perdew, J.; Ernzerhof, M. Generalized Gradient Approximation Made Simple. *Phys. Rev. Lett.* **1997**, *78*, 1396.

(27) Perdew, J. P.; Burke, K.; Ernzerhof, M. Generalized Gradient Approximation Made Simple. *Phys. Rev. Lett.* **1996**, *77*, 3865.

(28) Grimme, S.; Antony, J.; Ehrlich, S.; Krieg, H. A consistent and accurate ab initio parametrization of density functional dispersion correction (DFT-D) for the 94 elements H-Pu. *J. Chem. Phys.* **2010**, *132*, 154104.

https://doi.org/10.1021/acsnanoscienceau.4c00041
ACS Nanosci. Au XXXX, XXX, XXX−XXX

Supporting Information: Intermolecular interactions and quantum interference effects in molecular junctions

Louise O. H. Hyllested,[†] Idunn Prestholm,[†] and Gemma C. Solomon[*,†,‡]

†*Department of Chemistry and Nano-Science Center, University of Copenhagen, 2100 Copenhagen, Denmark*

‡*NNF Quantum Computing Programme, Niels Bohr Institute, University of Copenhagen, 2100 Copenhagen, Denmark*

E-mail: gsolomon@chem.ku.dk

Model system calculations

All Hückel model system calculations were performed with beta(β) as -2.7 eV and alpha(α) as 0 eV. The choice of beta is somewhat arbitrary but based on an approximate value to model the p system in conjugated molecules as used in previous calculations.[S1] The coupling V was -1.0 eV for a strong coupling and -0.2 eV for a weak coupling. δ was set to -0.4 eV^2 for a strong coupling and -0.0 eV^2 for a weak coupling. To investigate the intermolecular interactions, the intermolecular interaction integrals were set to a, b = 0.0 eV, 0.0 eV, for non-interacting molecules (SM) , a, b = -0.1 eV, -0.05 eV, for weakly interacting molecules (M), and a, b = -0.2 eV, -0.1 eV, for strong interacting molecules (DM).

The same model system was used to provide the examples for Figure 1 in the main paper. Here the choice of beta was kept at -2.7 and alpha was chosen as 0.0 and 1.0 for the direct signature and indirect signature, respectively. The interaction between the two molecules was chosen as a, b = -0.2 eV, -0.1 eV, the same as for the strong interacting molecules (DM) in the model. This was mainly chosen to provide a clear example of the indirect and direct signature of DQI explained in the introduction.

In Figure S1 the transmission on the log scale for the linearly conjugated system with strong coupling is illustrated for the three different intermolecular interaction integrals. The colours indicate whether the two molecules are non-interacting (SM), corresponding to two isolated molecules, weakly interacting (M), corresponding to a sparse monolayer, or strongly interacting (DM) corresponding to a dense monolayer. Figure S2 follows the same setup, for the cross-conjugated model system with strong coupling on the linear scale. S1 Lastly, Figure S3 follows the same setup, for the cross conjugated model system with weak coupling on the linear scale.

We note that as the primary difference in the model lies in how the ethene molecules are connected to the electrodes, the differences between linear and cross-conjugated systems are not evident when the transmission is plotted on a linear scale. The only notable distinction is that the transmission probability is lower for the cross-conjugated system compared to

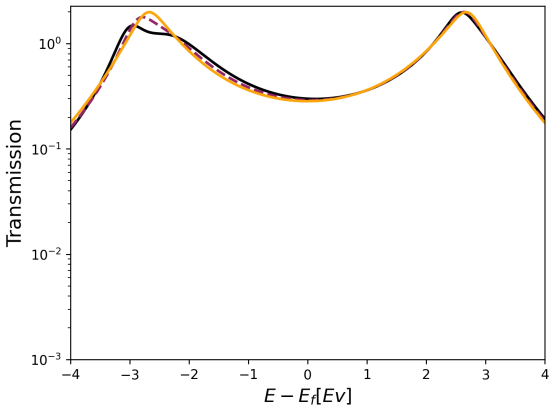

Figure S1: Hückel model calculation plot for the transmission of the Linear conjugated model system with strong coupling on a logarithmic scale. The non-interacting (green), weakly interacting (blue), and strongly interacting (red).

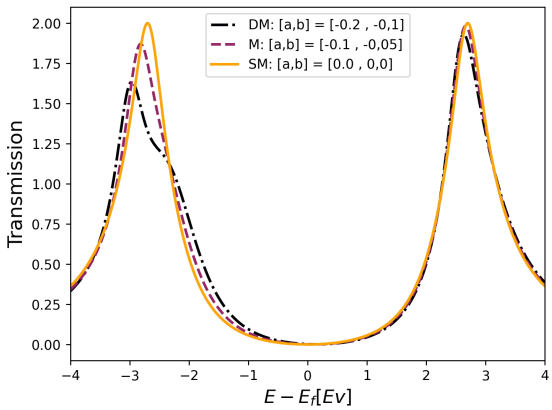

Figure S2: Hückel model calculation plot for the transmission of the cross conjugated model system with strong coupling on a linear scale. The non-interacting (SM), weakly interacting (M), and strongly interacting (DM).

the linear-conjugated system, this is visible in the strong coupling case in the re-scaling of the y axis between Figure 4b and Figure S2. This difference becomes impossible to see on the linear scale when there is weak coupling to the electrodes. Therefore, examining the log scale is crucial, the DQI feature is visible in Figure 4c (cross-conjugated system) but not in

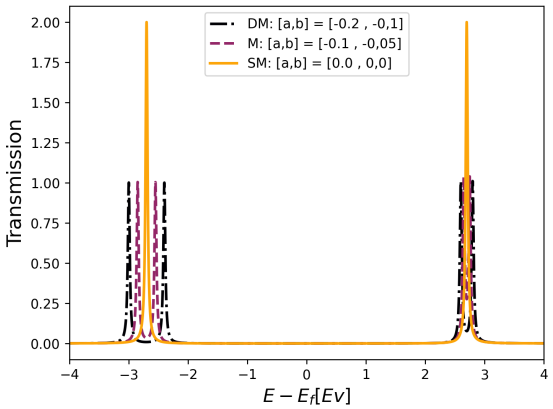

Figure S3: Hückel model calculation plot for the transmission of the cross conjugated model system with weak coupling on a linear scale. The non-interacting (SM), weakly interacting (M), and strongly interacting (DM).

Figure S1 (linear-conjugated system).

Differentiation of the total current

The differentiation of the total current was carried out as following. Knowing that total current through the system are calculated as:

$$I = \frac{2e}{h} \int_{-\infty}^{\infty} d\varepsilon \, [f_L - f_R] T(\varepsilon), \tag{1}$$

the $\frac{dI}{dV}$ (differential conductance) can be calculated by taking the difference of current and dividing it with the difference of the bias throughout the energy range, with the bias ranges chosen to be from -1.1 to 1.1 V.

$$\frac{dI}{dV} = \frac{I[i+1] - I[i]}{bias[i+1] - bias[i]} \tag{2}$$

For interest in the code used for transmission and dI/dV calculations see: `https://github.com/Solomon-Hansen/Intermolecular_interactions_QI_effects`

Values of E

To support the explanation of the increase and decrease of the transmission zero on the real axis, we have added the Energy at the transmission minimas for the different interaction strengths (dense monolayer, sparse monolayer and single molecule, i.e. no interaction). From these results it can be seen that the imaginary part increases going from the single molecule to the dense monolayer (See Appendix A for further details on the calculation).

Table S1: Energy at transmission zero

Single Molecule	0.0004
Monolayer	0.2636 + 0.0828 i
Dense monolayer	0.4129 + 0.3278 i

Electrostatic difference potential (EDP)

The electrostatic difference potential (EDP) represents the potential corresponding to the electron density difference between the self-consistent state and the initial state. The initial state is defined as the system before any interactions, while the self-consistent state is the system after it has reached equilibrium, i.e., after the redistribution of electron density due to interactions between atoms. EDP can be used to visualize how the potential landscape of a system changes due to interactions and can, therefore, provide insight into the charge rearrangement within the system. A positive EDP is interpreted as a loss of electrons, resulting in a positive charge, whereas a negative EDP is interpreted as a gain of electrons, resulting in a negative charge.

In Figure S4, the EDP of the different junction types (single molecule, clusters, dense, and sparse monolayers) are presented as a 2D projection obtained by taking each point along the z direction (along the junction) and averaging over x and y. Line A denotes the position of the Au atom binding to the S atom, while line B represents the position of the S atom. Similar to the observed shift in transmission spectra with varying molecule numbers in the

junction, a corresponding shift in the EDP can be seen. To determine whether this shift can be attributed to an electrode effect, the electrode-molecule interface can be examined. This interface spans the Au and S positions (lines A and B in Figure S4, respectively).

The charge induced in the molecule (or removed from the electrode) varies across the different systems. For instance, the dense monolayer (yellow) exhibits a higher degree of charge rearrangement, with more charge localized at the Au site and less at the S site compared to other configurations. This variation in charge rearrangement can be attributed to an electrode effect, although we cannot confirm to what extent this contributes to the shift of the interference.

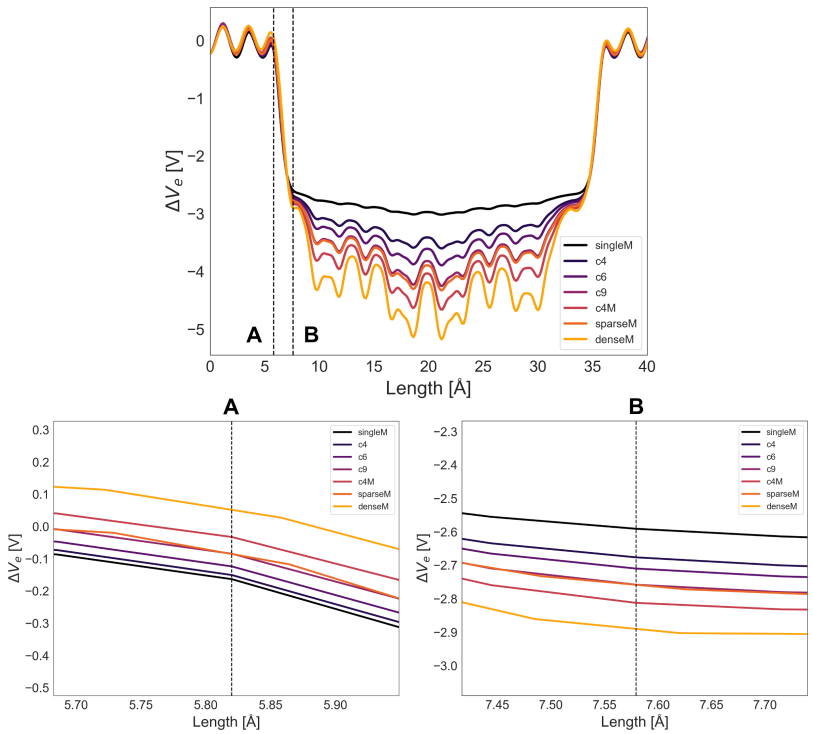

Figure S4: The electrostatic difference potential(EDP) of aqmt for the different junction types. The line A correspond to the location of the Au atom connecting to the Sulfur (S) and the line B the location of S. The A and B plot are a zoom of the initial plot for the Au line and S line, respectively.

Calculation Setup

The calculations were carried out in Quantum ATK. Each molecule was optimized using the GGA PBE functional in the gas phase, with sulfur and nitrogen passivated with hydrogen.[S2–S4] Following optimization the molecule was bound in a junction between 2 gold electrodes. The molecules were added to the gold electrode at an FCC hollow site, at a distance of 1.71Å from the gold surface for the S-bound molecule, resulting in a Au-S distance of 2.39 Å.,[S5 S6] For AQ-MT, the distance between H and Au was chosen to be 2.08Å, based on the previously shown distance of 2.06 between Au and H in an Au complex with a medium to strong hydrogen bond.[S7] This resulted in junctions as shown in Figure S5 and Figure S6 for a single molecule and C4 cluster junction with the AC-DT molecule.

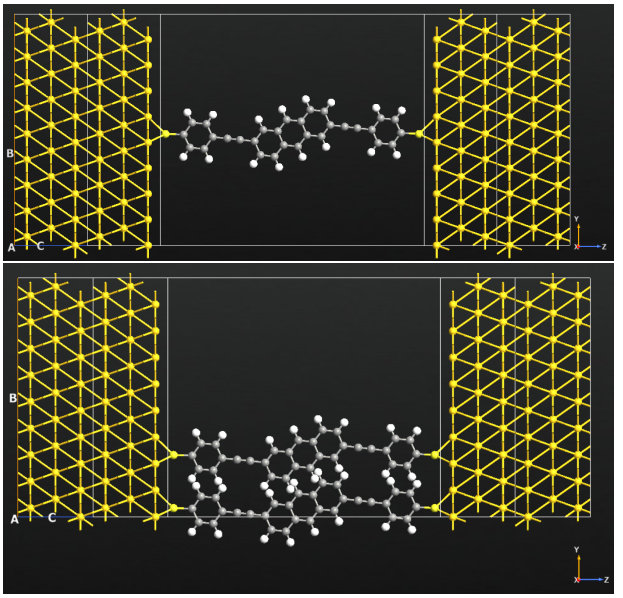

Figure S5: Top: Junction with single AC-DT single molecule. Bottom: C4 junction of AC-DT. Both from the side view.

The junctions were relaxed and optimized following the ATK optimize device configuration with the electrodes active (meaning that the device optimization will not try apply hydrogen passivation to the surface) and the region center chosen by ATK. The region length

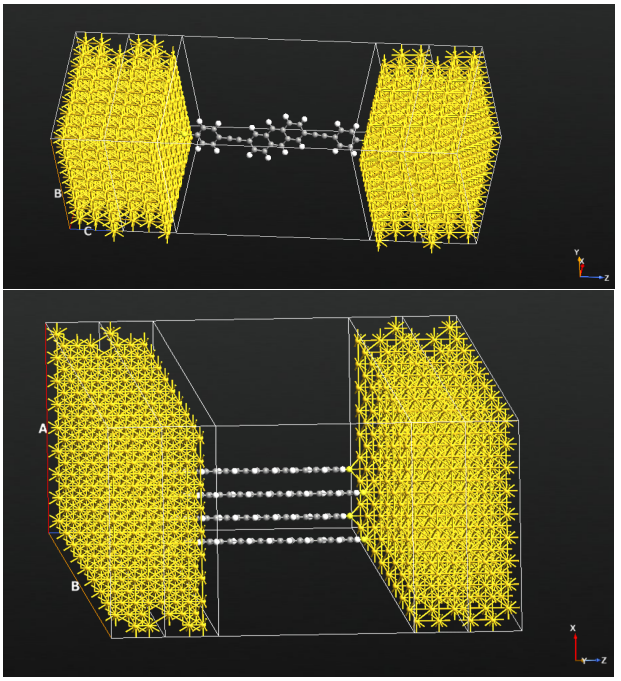

Figure S6: Top: Junction with single AC-DT single molecule turned. Bottom: C4 junction of AC-DT shown from an angle.

was measured from the left most sulfur atom and to the rightmost sulfur atom, adding 1.71Å to obtain the distance just above each electrode layer. The reason for this method was to avoid optimization of the topmost gold layer. The junction optimization was carried out for the single molecule junctions, sparse monolayer junction and dense monolayer junction. The cluster junctions were not optimized as a junction due to computational time.

Lastly, the transmission calculations were performed (using the GGA.PBE functional and a double-zeta basis (single- zeta on Au) set with polarization functions on all molecular atoms), with an energy range of -3 to 3 eV and 401 points. K point sampling was set to 35x35 for the sparse and dense monolayers, 10x10 for the single molecule, and 6x6 for the C4 monolayer junctions (these were chosen in the interest of computational time). For the cluster calculations the k point sampling was set to 1x1.

Data available

All .xyz and inputfiles for quantumATK can be found via DOI: `https://doi.org/10.17894/ucph.9ff34365-dd3c-4d14-9c53-d797108339eb` The README file explains the folder setup.

References

(S1) Baer, R.; Neuhauser, D. Phase coherent electronics: A molecular switch based on quantum interference. *Journal of the American Chemical Society* **2002**, *124*, 4200–4201.

(S2) Synopsis A/S, QuantumATK version S-2021.06-SP1. `www.synopsys.com/silicon/quantumatk.html`.

(S3) Burke, K.; Perdew, J.; Ernzerhof, M. Generalized Gradient Approximation Made Simple. *Phys. Rev. Lett* **1997**, *78*, 1396.

(S4) Perdew, J. P.; Burke, K.; Ernzerhof, M. Generalized Gradient Approximation Made Simple. *Phys. Rev. Lett.* **1996**, *77*, 3865.

(S5) Brandbyge, M.; Mozos, J. L.; Ordejón, P.; Taylor, J.; Stokbro, K. Density-functional method for nonequilibrium electron transport. *Physical Review B - Condensed Matter and Materials Physics* **2002**, *65*, 1654011–16540117.

(S6) Daigle, A. D.; Belbruno, J. J. Density functional theory study of the adsorption of nitrogen and sulfur atoms on gold (111), (100), and (211) surfaces. *Journal of Physical Chemistry C* **2011**, *115*, 22987–22997.

(S7) Schmidbaur, H. Proof of Concept for Hydrogen Bonding to Gold, AuHX. *Angewandte Chemie International Edition* **2019**, *58*, 5806–5809.

Appendix A

```
> with(MTM):
> wth(LinearAlgebra):
> with(plots):
```

Output from python minimum transmission.
DM: [a,b] = [-0.2 , -0,1] 0.0008471591509311533
M: [a,b] = [-0.1 , -0,05] 0.0002188130503900599
SM: [a,b] = [0.0 , 0,0] 6.986180319617075e-09
Numbers used here:
DM: [a,b] = [-0.2 , -0,1] 0.000848
M: [a,b] = [-0.1 , -0,05] 0.000219
SM: [a,b] = [0.0 , 0,0] 6.986e-09

```
> B := -2.7
```

$$B := -2.7 \tag{1}$$

```
> a := -0.1
```

$$a := -0.1 \tag{2}$$

```
> b := -0.05
```

$$b := -0.05 \tag{3}$$

```
> x := 0
```

$$x := 0 \tag{4}$$

```
> d := -0.4
```

$$d := -0.4 \tag{5}$$

```
> V := -1.0
```

$$V := -1.0 \tag{6}$$

```
> E := q
```

$$E := q \tag{7}$$

```
>
> H := Matrix([[x, B, b, a], [B, x, a, b], [b, a, x, B], [a, b, B, x]])
```

$$H := \begin{bmatrix} 0 & -2.7 & -0.05 & -0.1 \\ -2.7 & 0 & -0.1 & -0.05 \\ -0.05 & -0.1 & 0 & -2.7 \\ -0.1 & -0.05 & -2.7 & 0 \end{bmatrix} \tag{8}$$

```
> eI := Matrix([[E, 0, 0, 0], [0, E, 0, 0], [0, 0, E, 0], [0, 0, 0, E]])
```

$$eI := \begin{bmatrix} q & 0 & 0 & 0 \\ 0 & q & 0 & 0 \\ 0 & 0 & q & 0 \\ 0 & 0 & 0 & q \end{bmatrix} \tag{9}$$

```
> Gam := Matrix([[V^2, 0, 0, d], [0, 0, 0, 0], [0, 0, 0, 0], [d, 0, 0, V^2]])
```

$$Gam := \begin{bmatrix} 1.00 & 0 & 0 & -0.4 \\ 0 & 0 & 0 & 0 \\ 0 & 0 & 0 & 0 \\ -0.4 & 0 & 0 & 1.00 \end{bmatrix} \quad \textbf{(10)}$$

```
>
```

```
> Gam2 := Matrix([[0, 0, 0, 0], [0, V^2, d, 0], [0, d, V^2, 0], [0, 0, 0, 0]])
```

$$Gam2 := \begin{bmatrix} 0 & 0 & 0 & 0 \\ 0 & 1.00 & -0.4 & 0 \\ 0 & -0.4 & 1.00 & 0 \\ 0 & 0 & 0 & 0 \end{bmatrix} \quad \textbf{(11)}$$

```
> G := (eI - H + (i/2 · Gam) + (i/2 · Gam))^(-1) :
>
> Gr := LinearAlgebra[HermitianTranspose](G) :
> T := LinearAlgebra[Trace](Gam · G · Gam · Gr) :
>
```

(12)

```
> logplot(T, q = -1 ..1)
```

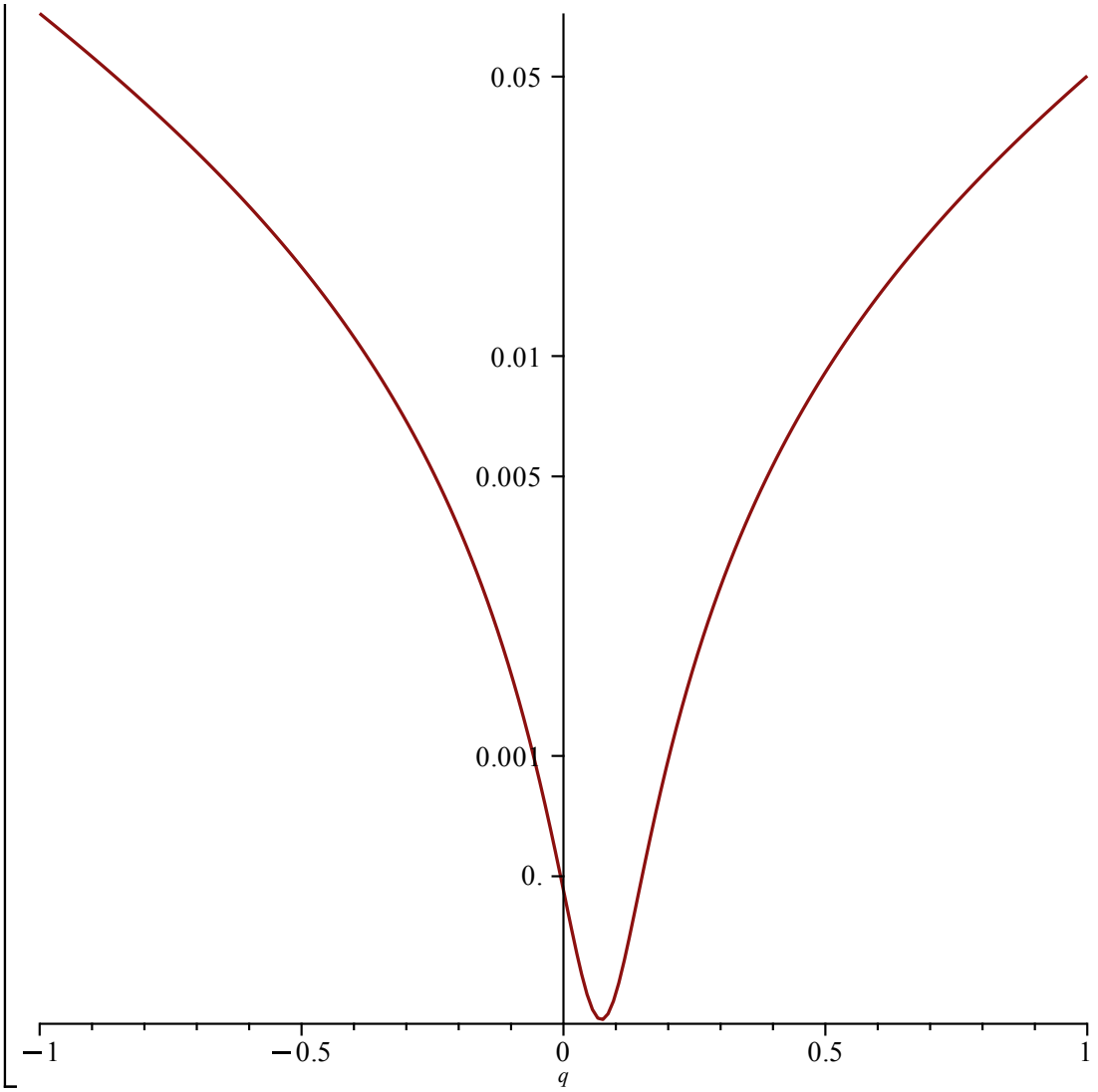

>

> $simplify(solve(T = 0.00219, q))$

$$0.2635749377 + 0.08277093248\,I \qquad \textbf{(13)}$$

>

Dense Monolayer:
T= 0.00848 0.4128583179 + 0.3277595099 I
Monolayer:
T = 0.00219 0.2635749377 + 0.08277093248 I
Single Molecule :

$\mathrm{Re}(T = 6.986 \cdot 10^{-9})\ \ 0.0004000348413\ ,\ \mathrm{Im}(T = 6.986 \cdot 10^{-9})\ \ 0$

>

>

>

>

B

PUBLICATION 2

Manuscript in preparation.

Frontier Orbital Gating of Rectification and Conductance in Tunneling Junctions Comprising Pyridine-terminated Molecular Wires

Saurabh Soni[1], Louise O. H. Hyllested[6], Marco Carlotti[3], Sumit Kumar[2], Jane Kardula[4], A. G. Mike Uiterwijk[4], Remco W. A. Havenith[4,5], Olle Hellman[7], María Camarasa Gómez[7], Leeor Kronik[7], Gemma C. Solomon[6,8], and Ryan C. Chiechi*[9]

[1]Hybrid Materials for Opto-Electronics Group, Department of Molecules and Materials, MESA+ Institute for Nanotechnology, Molecules Center and Center for Brain-Inspired Nano Systems, Faculty of Science and Technology, University of Twente, P.O. Box 2017, 7500 AE Enschede, The Netherlands
[2]Electrical Engineering Division, Department of Engineering, University of Cambridge, United Kingdom
[3]Italian Institute of Technology, Center for MicroBioRobotics, Viale Rinaldo Piagio 34, 56025, Pontedera, Italy
[4]Stratingh Institute for Chemistry, University of Groningen, Nijenborgh 4, 9747 AG Groningen, the Netherlands
[5]Zernike Institute for Advanced Materials, Nijenborgh 4, 9747 AG Groningen, the Netherlands
[6]Department of Chemistry and Nano-Science Center, University of Copenhagen, Copenhagen, Denmark
[7]Department of Molecular Chemistry and Materials Science, Weizmann Institute of Science, Rehovoth 7610001, Israel
[8]NNF Quantum Computing Programme, Niels Bohr Institute, University of Copenhagen, Denmark
[9]Department of Chemistry & Organic and Carbon Electronics Cluster, North Carolina State University, Raleigh, North Carolina 27695-8204, United States
*e-mail: ryan.chiechi@ncsu.edu

Keywords: Molecular Electronics · Rectification · Self-assembled Monolayers · EGaIn

Target Journal:

Abstract

1 Introduction

Molecular electronics explores the electronic structure and properties of both ensembles of molecules[Liu2021, Vilan2017] and individual molecules,[Xin2019, Chen2021] which are typically contacted by at least two metal electrodes. This investigation often considers the effects of an applied external bias. Over the years, various properties of molecules have been discovered, such as insulators, switches, and rectifiers. In 1974, Aviram and Ratner proposed a unimolecular rectifier consisting of donor and acceptor fragments separated by a methylene bridge as a prototypical molecular-electronic circuit element.[aviram1974molecular] In the intervening decades, numerous molecules in different device geometries have been investigated as potential unimolecular rectifiers operating by the mechanism they proposed.[Metzger˙unimolecular˙rectifiers] In response, other studies have proposed molecules that defy the donor-bridge-acceptor paradigm, particularly in molecular ensemble junctions (MEJs)[Liu2021] comprising self-assembled monolayers (SAMs) with eutectic Gallium-Indium (EGaIn)[Chiechi2008] as the top electrode. They have suggested thermally-assisted hopping-plus-tunnelling (H+T),[Yuan2015, Chen˙2017] the Stark-effect,[Xie2018, Cho2018, Ai2018] and asymmetries created by permanent dipoles[Ocampo2015] as alternative mechanisms for rectification.

Expanding on their earlier research, van Dyck and Ratner reported a rectification mechanism (vDR) that depends on the pinning of spatially separated frontier molecular levels to different electrodes.[VanDyck2015] Rather than utilizing donor (*i.e.*, high-lying HOMO) and acceptor (*i.e.*, low-lying LUMO) units, frontier orbitals that are localized on either

side of a saturated spacer follow the electrodes in and out of the conduction window at forward and reverse bias,[Jia2013, Xie2015] resulting in asymmetric tunneling charge-transport (rectification). Like most theoretical models—including the original donor-bridge-acceptor model—the model was developed for single-molecule junctions.

Since ensemble junctions are more stable and thus more usable as electronic components, it is crucial to understand how these systems behave in regard to rectification. The aforementioned MEJ-based phenomena have been reproduced in several different systems. Recently, molecules based on benzotetrathiafulvalene headgroups were reported to rectify depending on the choice of metal substrates, as different frontier levels fall in the conduction window, effecting the H+T mechanism.[Han2020] As the molecular levels participate in electron-transport, temperature-assisted hopping occurs between the metal and the respective energy level, exactly as for the prototypical ferrocene-terminated alkanethiol H+T rectifiers.[Yuan2015, Chen'2017] Stark-effect-based rectification has been observed in alkanethiols bearing pyrene and benzo[a]pyrene[Cho2018] and $-$COOH head groups.[Ai2018] Pure and mixed SAMs of alkanethiols bearing bipyridyl headgroups enabled the observation of the charge-transport transitions from the normal to inverted Marcus[Yuan2018] regime, in which the H+T mechanism becomes activationless.[Kang2020, Kang2021] This system also exhibits a design principle of the van Dyck-Ratner (vDR) mechanism; the LUMO on the bipyridyl moiety and the HOMO on thiol anchor pin strongly to the EGaIn top electrode and Au bottom electrode, respectively. Bipyridyl-metal complexes terminated by alkanethiols also exhibit control over rectification by changing the alignment and identity of the frontier orbitals with respect to

the Fermi level E_F by varying the identity of the metal ion.[Park2021] Although these studies all invoke the concept of level-alignment and Fermi pinning at bias, none explicitly follow the vDR mechanism or address the role of orbital resonances[Perrin2014, Perrin2020] and the strength of coupling between two frontier orbitals involved in conduction or rectification.

To investigate the influence of spatially-separated frontier orbitals and their coupling to electrodes on molecular rectification, we designed and synthesized a series of highly polarizable *p*-oligo(phenylene ethynylene)pyridine compounds denoted mOPPyn, where $n = 1-4$ indicates the number of aromatic rings and the prefix m denotes a CH_2 (methylene) bridge between the π system and the thiol anchor, as shown in Fig. 1a. The spatial overlap of the HOMO and the LUMO varies inversely with n and the highest rectification ratios occur when $n = 3$, suggesting a correlation between the spatial separation of the frontier orbitals and the magnitude of rectification, as predicted by the vDR mechanism. To control for asymmetric coupling to the electrodes, we also synthesized OPPy3, which is directly conjugated to the thiol anchor. We found that the magnitude of rectification responds to molecular length (n), independent of the coupling to the anchoring thiol / bottom electrode (m), supporting the assertion of the vDR mechanism that thiols are weakly coupled to π systems and that interfacial dipoles are more relevant than coupling.

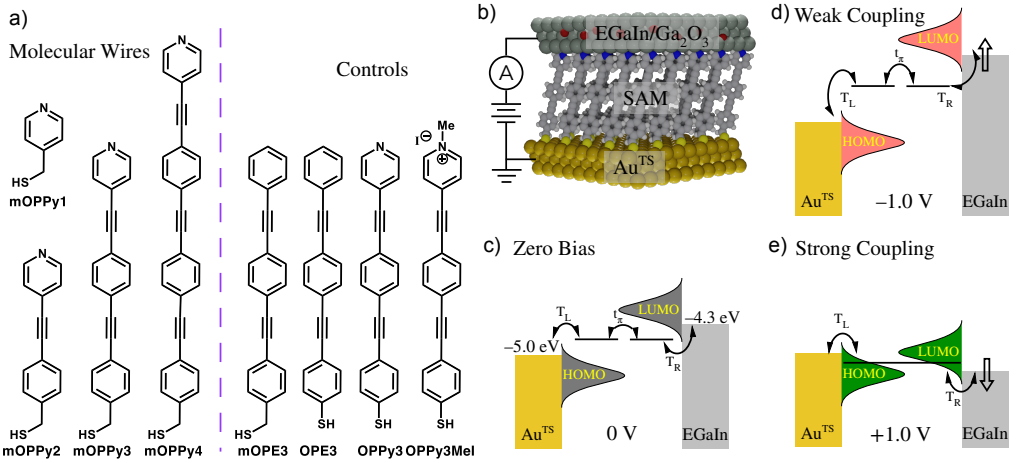

Figure 1: (a) Chemical structures of mOPPy*n* molecules, for n = 1-4, with pyridino head groups studied in this work along with the control molecules. (b) Illustration of a large-area molecular ensemble junction (MEJ) comprising a self-assembled monolayer sandwiched between Au^{TS} (bottom electrode) and EGaIn (top electrode). (c) Schematic of band-diagram of the MEJ showing the E_F of two electrodes and the molecular HOMO & LUMO levels at zero bias. (d,e) Band diagrams showing shifts of the energy levels of EGaIn under applied biases of opposite polarity, resulting in systematic shifts of the frontier molecular levels inside the tunneling barrier.

2 Results and Discussion

Molecular design. Asymmetric coupling of a frontier orbital to the leads is not sufficient to induce rectification;[Baldea2021] there must (also) be a bias-induced shift (*e.g.*, the Stark-shift and H+T mechanisms) or the recruitment of an additional orbital (*e.g.*, the vDR mechanism). A prerequisite for bias-induced shifts is polarizability, which is often accomplished by inserting a saturated spacer between the π-conjugated fragment (on which the orbital is localized) and the anchoring group.[Yuan2015, Zhang2018] Similarly, van Dyck and Ratner prescribe a saturated spacer, which both localizes the frontier orbitals on the flanking π-

conjugated fragments and decouples them from the opposite electrodes; however, the spacer is not required by the theoretical framework, only that the orbitals gating transport are pinned to the electrodes and relatively weakly coupled to each other. Further, the model compounds proposed by van Dyck and Ratner (asymmetric oligoenes) would be non-trivial to synthesize, let alone to use for growing SAMs. Thus, we designed a series of molecules that are straightforward to synthesize and grow SAMs from, but that still fulfill the requirements of the vDR mechanism. The main requirement is that the frontier molecular orbitals (MOs) track E_{F}, otherwise known as pinning, the driving force behind which is polarizability.[VanDyck2014] Theoretically, pinning is defined as $S \approx 0$ in Eq. (1) where S refers to the degree of pinning, E_{MO} is the energy of the relevant MO in the junction and IP_{g} is the ionization potential of the MO in the gas phase; when $S = 0$, IP_{g} has no to little effect and the functional group have no effect on $E_{\mathrm{F}} - E_{\mathrm{MO}}$.[VanDyck2013]

$$S \equiv \left| \frac{d(E_{\mathrm{F}} - E_{\mathrm{MO}})}{d(IP_{\mathrm{g}})} \right| \approx 0 \tag{1}$$

We designed our molecules without a spacer between the fragments on which the frontier MOs are localized, such that they are fully π-conjugated and the localization of the frontier orbitals is instead controlled by the electronegativities of functional groups. In this design, Eq. (1) works in our favor, since the HOMO will pin to the Au substrate and the LUMO will pin to the EGaIn top-contact and $E_{\mathrm{F}} - E_{\mathrm{MO}}$ will depend almost entirely on the interfacial dipoles. The dipole moments of the two anchoring moieties—Au–S and pyridyl-

EGaIn—simultaneously localize the frontier MOs and lower the frontier MO gap E_g, while the polarizability of the OPE backbone effects pinning.[VanDyck2015] We included a CH_2 spacer between the π-conjugated backbone and the thiol anchor to assist the inductive push-pull effect (to localize the frontier MOs) and decreases the tilt angle, but it does not substantially alter the weak coupling between the thiol and the π system that results from poor MO overlap. The spacer also allows us to test that hypothesis and the theory of the vDR mechanism by independently varying the coupling and interfacial dipoles, as discussed below.

We chose pyridyl groups as the 'pull' in the push-pull because they are structurally analogous to phenyl groups, affecting the frontier MOs without affecting the self-assembly process.[Fracasso2013] Pyridyl groups can act as an anchor for growing SAMs on metallic surfaces,[Wang2009, Ma2011] but several experimental studies[Sauter2017, Silien2008, Wchter2018, Fracasso2013] have found that molecules containing both thiolate and pyridyl groups preferentially bind to gold surfaces via the thiolate anchoring group. Moreover, Zharnikov *et al.*[Wchter2018, Sauter2017, Silien2008] and Wöll *et al.*[Liu2010] have reported the growth of SAMs of thiolate-anchored, pyridine-terminated π-conjugated molecular wires on metallic surfaces, which they rigorously characterized by (HR)XPS, NEXAFS, surface IR, and STM. To control for the effects of pyridyl groups, we include OPE3 and mOPE3, which are the same lengths as the mOPPy3 and OPPy3, but which substitute the terminal pyridyl group for a phenyl group. These molecules control for the push-pull effects and provide junctions against which to compare the mOPPyn series that are unambiguously bound to the electrode through a thiolate anchor.

The operational principle of the mOPPyn MEJs is shown in Fig. 1c-d. At 0 V, E_F sits between the frontier orbitals; the work functions (shown above the electrodes in Fig. 1c) are such that the electrodes that are in contact with the ends of the molecules are also closest in energy to the respective frontier MOs, which pin to them (*i.e.*, sit at a fixed $E_F - E_{MO}$). While E_g is reduced in a MEJ compared to the gas phase, at zero bias the orbitals remain separated by E_g. As a result of the polarizability of OPE moieties, the MOs track the electrodes such that at -1 V bias the LUMO is shifted further apart from the HOMO (Fig. 1d) and E_g increases. Since coupling varies inversely with E_g, the frontier MOs are qualitatively weakly coupled at negative bias. The exact opposite happens when 1 V is applied; E_g decreases and, ideally, the frontier MOs become strongly coupled, creating a resonant channel and increasing the transmission probability (Fig. 1e). Thus, the rate of charge-transport through the MEJ is higher at positive bias than at negative bias, and the rectification ratio $|R| = |\frac{J(+)}{J(-)}| > 1$, where $J(+)$ and $J(-)$ are the current densities at positive and negative bias, respectively.

Electrical characterization. We fabricated MEJs comprising SAMs of the molecular wires shown in Fig. 1a, on template-stripped Au (Au^{TS}, **??**)[weiss2007si] contacted by a cone-shaped non-Newtonian liquid metal alloy, eutectic Ga-In (EGaIn), as the top electrode.[Chiechi2008] An idealized schematic of the Au^{TS}/SAM//Ga_2O_3/EGaIn MEJ is shown in Fig. 1b, where '/' and '//' denote covalent and non-covalent interfaces, respectively. The Au^{TS} electrode was grounded while external bias was applied to the EGaIn top electrode to acquire tunneling current density vs. Voltage (J–V) data. The details of instrument setup and data acquisition

methodology are described in the Supporting Information.

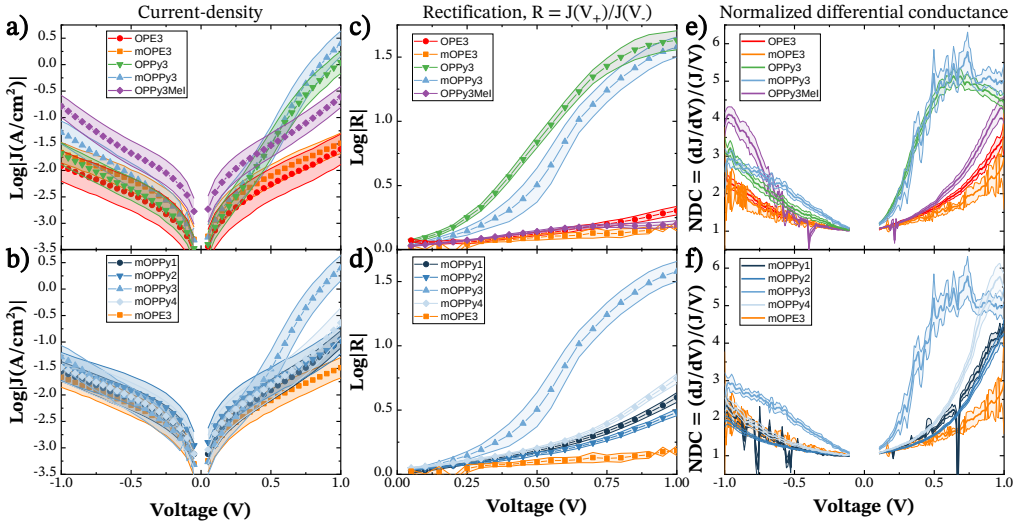

Figure 2: $J-V$ characteristics of molecules under study: OPE3, mOPE3, OPPy3, OPPy3MeI, and mOPPyn (for n = 1-4). (a,b) Semi-log plots of current-density (J) vs. applied voltage (V) highlighting symmetry and asymmetry in $J-V$ curves for different molecules. (c,d) Semi-log plots of the rectification ratio, $R = \frac{J(+1V)}{J(-1V)}$, vs. V showing highest rectification ratio for OPPy3 and mOPPy3 and near-zero rectification for non-pyridyl cotrols and the methylated-derivative OPPy3MeI. (e,f) Normalized differential conductance, NDC $= \frac{dJ/dV}{J/V}$, plots indicating the influence of molecular levels on conductance in the form of peaks for $V > 0$. For all the subfigures a-e, we have plotted the gaussian-averaged means with 95% confidence intervals as the corresponding error bands, explained in detail in the Supporting Information.

The $J-V$ characteristics are shown in Fig. 2. From the $\log|J|$ vs. V plots in Fig. 2a, it can be seen that the pyridyl-terminated OPPy3 and mOPPy3 are significantly more conductive at positive bias than at negative bias, while OPE3, mOPE3 and OPPy3MeI all yield symmetric $J-V$ curves. This result suggests that the pyridyl groups are necessary to observe rectification, which could be caused either by the pyridyl//EGaIn interface or the electronic structure of the pyridyl-functionalized molecular wires. The methylated derivative

OPPy3MeI also exhibits symmetric $J-V$ curves, verifying that free pyridyl (*i.e.*, not phenyl or pyridinium) groups at the SAM//EGaIn interface are necessary for rectification. A previous study of pyridine-terminated oligophenylenes in MEJs showed that the pyridyl//EGaIn interface itself does not cause rectification.[Fracasso2013] Together, these observations suggest that the electronic structure of the molecular wires is responsible for the observed rectification.

Figure 2b shows the $\log|J|$ vs. V plots of the mOPPyn series together with mOPE3. The low-bias conductance is comparable across the mOPPyn series, indicating that there is little dependence of conductance on molecular length, which is not the case for OPEn monothiol and dithiol series.[flowbox, Xie2015] This observation supports the hypothesis that the mOPPyn series fulfills the vDR mechanism criterion that $S \approx 0$ meaning that $E_{\mathrm{F}} - E_{\mathrm{MO}}$ is insensitive to E_{g}, which decreases with increasing conjugation. Table 1 shows that E_{g} decreases by $\sim 1\,\mathrm{eV}$ across the mOPPyn series, which would otherwise manifest as increasing conductance as the offset between E_{F} and the transport level decreases. Although not common, other $S \approx 0$ systems have been reported by observing very small or even negative tunneling decay coefficients,[Zhang2018, Lee2021] including polyyne molecular wires with symmetric pyridyl anchoring groups in single-molecular junctions.[Wang2009]

To compare the rectification of the MEJs directly, we plotted $\log|R|$ versus $|V|$ in Fig. 2c-d. As with conductance, the low-bias regions are all similar, but OPPy3 and mOPPy3 reach values of R of 42.75 and 37.87, respectively, while $R \approx 1$ across the entire bias-range

Table 1: Tabulated values for the different calculated and experimental properties. The optical bandgap was calculated from the onset of the UV-Vis spectra. Energies of HOMO and LUMO levels, and the dipole moments were calculated using gas-phase DFT simulations, while E_g from TDDFT. EGaIn yields were calculated as the number of non-shorting working junction divided by the total number of junctions and the rectification ratio was calculated by using the following equation: $R = \frac{J(+1V)}{J(-1V)}$. Contact angles were measured using 1 µL droplet of water. The thickness of the monolayer was determined using ellipsometry.

	OPE3	mOPE3	mOPPy1	mOPPy2	mOPPy3	mOPPy4	OPPy3	OPPy3MeI
Optical E_g (eV)	3.44		3.95	3.35	2.95	2.86	2.97	-
R at 1 V	2.02	1.53	3.95	3.15	37.87	6.97	42.75	1.50
$V_{trans}{}^{+}$ (V)	0.72	0.78	0.53	0.65	0.26	0.25	0.53	0.56
$V_{trans}{}^{-}$ (V)[c]	-0.87	–	–	-0.99	-0.52	-0.62	-0.87	-0.6
Contact angle	–	–	59.2±5.8	75.7 ± 5.7	79.8 ± 69.5	89.0 ± 5.7	78.0 ± 5.7	89.8 ± 5.8
SAM thickness	-	-	-	-	-	-	-	-

[c]for mOPE3 and mOPPy1, $V_{trans}{}^{-}$ was outside measurement window.

for the other molecular wires. The mOPPy−n molecular wires (Fig. 2d) for $n \neq 3$ exhibit significantly lower values of R, but are still higher than OPE3, mOPE3 and OPPy3MeI. The values of R at 1 V are summarized in Table 1.

Finally, we computed the normalized differential conductance, NDC = $\frac{(dJ/dV)}{(J/V)}$, for all the molecules under study, as shown in Fig. 2e and f. The NDC heatmaps of all the raw binned data are separately shown in **??** of the Supporting Information. In our previous work, we showed that presence of peaks in the NDC plots can suggest that the frontier molecular levels come in resonance with the E_F level of the metal, increasing the transmission probability of the tunneling charge.[Zhang2018] Here, it is clear that for OPPy3 and mOPPy3 molecular wires, the NDC curves exhibit a peak at ∼0.6 V. The other molecules in mOPPy−n series also show a rise in NDC at V → 1, while on the other hand, they all have bowl-shaped NDC for V<0, same as the control molecules. This suggests absence of dominance of frontier molecular levels in tunneling conductance for the negative bias range,

unlike for the positive bias range for the rectifying molecules. The frontier levels, especially the lowered LUMO because of the electron-withdrawing pyridyl group, comes in resonance with E_F of the electrodes. This result is in agreement with the calculated molecular energy levels as shown in Figure **??** and the V_{trans} values as shown in **??** and Table 1. The ${V_{trans}}^+$ for the pyridine series is smaller than the corresponding ${V_{trans}}^-$ but specifically for OPPy3 and mOPPy3, the ${V_{trans}}^+$ is very small, suggesting proximity of LUMO level to the E_F.

Charge transport simulations To gain further insights into the charge-transport mechanism in the MEJs comprising the pyridine-functionalized OPEn molecules, we implemented density functional theory (DFT) simulations in conjunction with the non-equilibrium Green's function (NEGF) approach. Details of the calculations are provided in the Supporting Information. These simulations were performed for OPPy2, OPPy3, OPPy4, and OPPy5. The decision to calculate Au-S instead of Au-S-CH_2 is based on its simpler geometry and fewer degrees of freedom. In contrast, the addition of the $-CH_2$ group increases flexibility and introduces more complex interactions, making the system harder to model accurately (A comparison of the transmission for mOPPy3 and OPPy3 can be found in the Supporting Information). Since our experiments did not reveal a significant difference between these linker groups, we are confident that this choice does not affect the results.

To simulate the experiments, transmission spectra and $I - V$ curves were calculated with biases ranging from -1 V to +1 V in a junction consisting of Au - molecule - Aluminium (Al). Al(111) was chosen as the top electrode, since the workfunction of Al is similar to that

of EGaIn (Al (4.24 eV) and EGaIn (4.1–4.2 eV)).[AlWF, EgainWF] The junctions were created following the method of Kang *et al.*, who previously demonstrated that Al(111) can be used as a model for EGaIn due to its similar workfunction and its lattice constant being comparable to that of Au(111).[AlEgain] It is common for calculations of junctions to use Au for both electrodes, but we emphasize the importance of electrode choice, as we observed differences in our calculations depending on the top electrode used. A comparison of the results for the Au and Al top electrode is provided in the Supporting Information.

In order to gain deeper insight into the electronic properties of the system, we analyzed how the transmission spectra respond to different applied biases, revealing a notable shift in the LUMO peak. Figure 3 shows the transmission spectra at -1 V (Figure 3a) and +1 V (Figure 3b) for OPPy2, OPPy3, OPPy4, and OPPy5. The orange shading corresponds to the bias window. At -1 V, the LUMO peak for all the molecules is centered around 0.5 eV. However, at +1 V, the LUMO peaks shift to different energy levels. The current is calculated based on the area under the transmission curve within the bias window. As shown in Figure 3, the peaks shrink with increasing molecular length, suggesting that the current decreases with molecular length. The calculated $I - V$ curves demonstrating this can be found in the Supporting Information.

Since the peaks at +1 V move into the bias window, more current is observed at +1 V than at -1 V, resulting in rectification, consistent with the experimental results. In addition, the LUMO peak is pinned at -1 V but shifts in energy at +1 V. This behavior aligns with the

MEJ operational principle shown in Figure 2c,d,e. The locations of the HOMO and LUMO peaks for all molecules under bias are shown in Figure **??**.

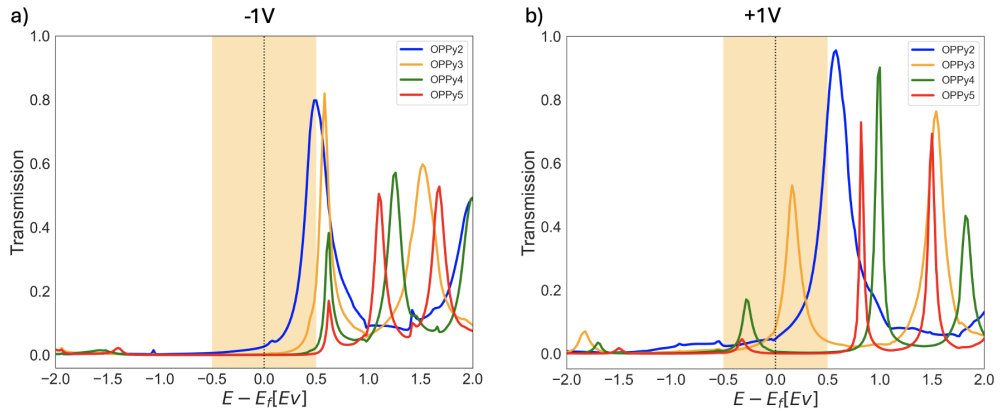

Figure 3: Transmission spectrum from -2 to +2 eV for OPPy2 (blue), OPPy3 (orange), OPPy4 (green), and OPPy5 (red), at -1 V (a) and +1 V (b). The orange shade corresponds to the bias window.

The splitting and gathering of the LUMO peaks can be attributed to the behavior of the MO. The LUMO are influenced by the electric field, as illustrated in Figure 4. For clarity, the top layer of each electrode is shown, though these are not part of the MO. The MO are calculated solely for the molecule within the junction. The MOs in Figure 4 is an illustration of the LUMO at +1 V and -1 V. At +1 V, the LUMO shift towards the pyridyl group, whereas at -1 V, the LUMO are more evenly distributed across the entire molecule. These tendencies become more pronounced with increasing molecular length. Since the LUMO is the main contributor to the transmission only the LUMO is shown in Figure 4. The HOMO and LUMO at 0 V can be seen in Figure **??**.

To understand the effect of the dipole moment on the observed movement of the LUMO

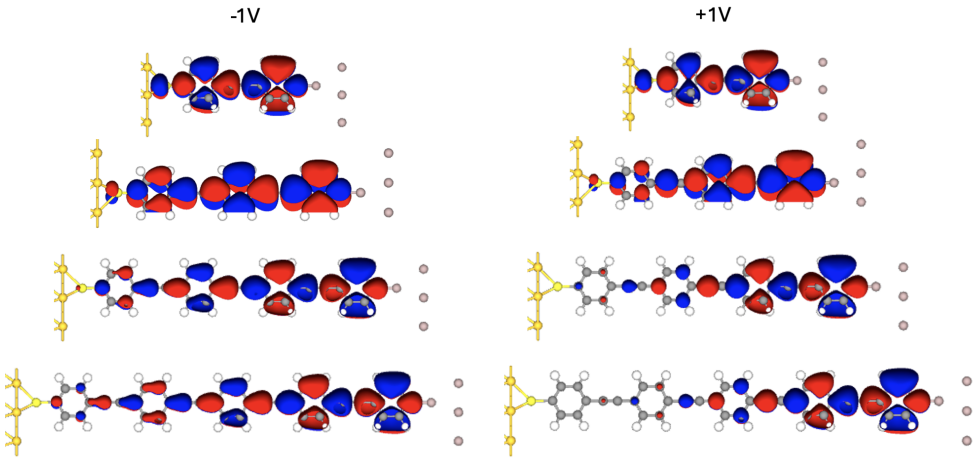

Figure 4: Lowest unoccupied molecular orbital (LUMO) of OPPy2, OPPy3, OPPy4, and OPPy5, from top to bottom, respectively. This figure illustrates the LUMO under biases of -1 V (left) and +1 V (right).

peak, the dipole moments of the molecules were calculated without electrodes. These calculations were performed with two molecules placed in parallel between two plates, making them independent of the electrodes. The dipole moments follow the same trend observed for the LUMO peak: a splitting of the dipoles at +1 V and a gathering of the dipoles at -1 V. The dipole moment and the LUMO peak, can be seen in Figure 5a,b. Figure 5a illustrates the movement of the LUMO peak with bias. Here, the grey triangles indicate the opening of the bias window with increasing voltage. At -1 V, the LUMO peak for all molecular lengths gathers around 0.5 eV, while at +1 V, the LUMO peaks split, as observed in Figure 3. Comparing this to Figure 5b, a similar trend is evident: the dipole moments of the molecules gather at -1 V and spread out at +1 V. This observation illustrates that it is not solely the asymmetry of the electrodes that creates the rectification.

The observation of a gathering in both the LUMO peak and the dipole moment at -1 V suggests that the spread of the LUMO across the junction leads to similar transmission characteristics and dipole moments for all molecules. Conversely, at +1 V, the shift of the LUMO towards N creates a more pronounced difference in both the dipole moment and the LUMO peak location. This aligns with the molecular design, as we observe that the LUMO are localized towards the N, pinning to the EGaIn top electrode.

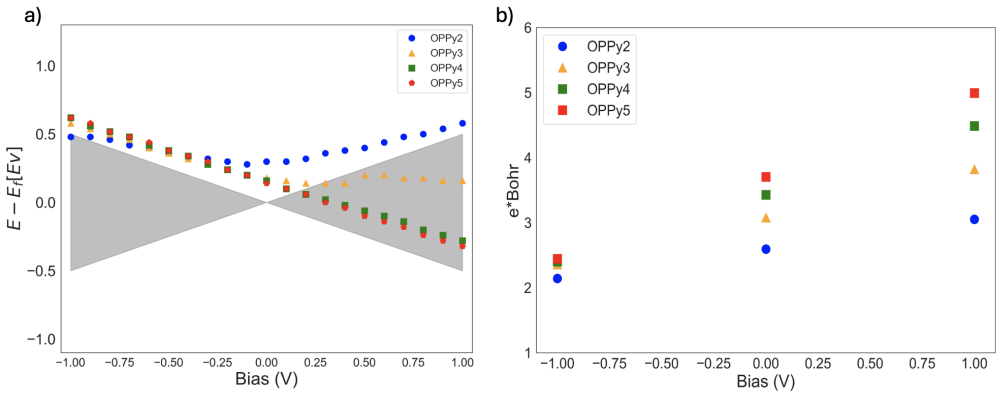

Figure 5: (a) Illustration of the LUMO peak location for OPPy2, OPPy3, OPPy4 and OPPy5, with Bias (V) on the x-axis and Energy ($E - E_{\mathrm{F}}$) on the y-axis. The grey triangles illustrate the bias window as we move towards higher bias. Each point is the location of the top of the LUMO peak. (b) Dipole moment of OPPy2, OPPy3, OPPy4 and OPPy5 with Bias (V) on the x-axis and the dipole moment on the y-axis in units of e*Bohr.

We do not observe clear evidence in the calculations explaining why mOPPy3/OPPy3 should be orders of magnitude better at rectifying than the other molecules. Since we observe an effect similar to the LUMO peak shift in the dipole independently of the electrodes, we argue that the better the dipoles of the molecules are aligned and self-organized in the SAM, the better rectification would be observed. However, disorder in the dipoles within

the monolayers cannot be accounted for in the simulations.

3 Conclusion

This paper highlights the influence of spatially separated frontier orbitals on molecular rectification. Instead of incorporating a spacer between the HOMO and LUMO carrying fragments (as the vDR model suggests), the molecules were designed without a spacer, utilizing the electronegativity of the functional groups to separate the LUMO and HOMO. This design resulted in clear rectification, especially for OPPy3, demonstrating that this approach is highly effective for molecular rectifiers. These findings suggest that a spacer in the molecular backbone is not essential to create a rectifying molecule, opening the door for easily synthesizable and self-assembled monolayer rectifiers. Looking ahead, the insights gained from this study suggest promising avenues for the development of molecular rectifiers. Continued theoretical and experimental investigations will be essential to refine these concepts and enhance the performance and manufacturability of molecular rectifiers.

4 Experimental

Materials and Methods The synthesis of OPE3, OPPy3, mOPPy1, mOPPy3 have been reported previously.[Carlotti2016, SLMpaper, Fracasso2013] The synthesis of the rest of the molecules is provided in the Supporting Information. Extra-dry toluene and 1,8-Diazabicyclo(5.4.0)undec-7-ene (DBU) was purchased from Sigma-Aldrich. 99.99% Au was obtained from Schöne Edelmetaal B.V. and 'Norland 61' optical adhesive purchased from Norland Products Inc. for preparing Au^{TS} substrates. Uvitron product Intelly-ray 600 (UV0832) was used to cure the optical adhesive.

SAM preparation and EGaIn measurements SAMs were prepared using established methodology.[flowbox] 50 µM solutions of the molecules were prepared in extra-dry Toluene under inert nitrogen atmosphere. 3 m]liter of this solution was used and a 100 nm Au^{TS} 1 cm × 1 cm substrate was immersed overnight. 0.05 mL of 17 mM DBU in extra-dry Toluene was added to the solution for 1.5 h. Following which, the substrates were rinsed with 3 mL ethanol drop-wise. The substrate was dried under nitrogen flow and EGaIn measurements were performed inside a flowbox with controlled atmosphere (O_2 = 1-3%; relative humidity ¡ 10%), the details of which are described in the Supporting Information, same as our previous report.[fracasso2011evidence]

DFT The calculations were conducted using density functional theory (DFT) combined with the Greens function approach and the Landauer formula to determine the transmission and conductance. QuantumATK (version S-2021.06-SP1) [**ATK**, **ATK-DFT**, **ATK-NEGF**] was employed for these calculations, utilizing the GGA PBE functional [**PBE1**, **PBE2**]. A double-ζ basis set and polarization functions on all molecular atoms were used, along with periodic boundary conditions. Additionally, non-covalent interactions were accounted for by incorporating the Grimme DFT D3 dispersion correction [**Grimme2010**]. Further details regarding the calculations can be found in the supporting information.

XPS measurements Sumit will enter XPS experimental here

Acknowledgments

R.C.C. and M.C. acknowledge the European Research Council for the ERC Starting Grant 335473 (MOLECSYNCON). S.S. acknowledges the Zernike Institute for Advanced Materials. We thank the Center for Information Technology of the University of Groningen for their support and for providing access to the Peregrine high performance computing cluster. G.C.S acknowledge the European Research Council (ERC) for their generous funding of this project under the European Union's Horizon 2020 research and innovation programme (grant agreement No 865870).

Supporting Information for: **Frontier Orbital Gating of Rectification and Conductance in Tunneling Junctions Comprising Pyridine-terminated Molecular Wires**

Saurabh Soni[1], Louise O. H. Hyllested[6], Marco Carlotti[3], Sumit Kumar[2], Jane Kardula[4], A. G. Mike Uiterwijk[4], Remco W. A. Havenith[4,5], Olle Hellman[7], María Camarasa Gómez[7], Leeor Kronik[7], Gemma C. Solomon[6,8], and Ryan C. Chiechi*[9]

[1]Hybrid Materials for Opto-Electronics Group, Department of Molecules and Materials, MESA+ Institute for Nanotechnology, Molecules Center and Center for Brain-Inspired Nano Systems, Faculty of Science and Technology, University of Twente, P.O. Box 2017, 7500 AE Enschede, The Netherlands
[2]Electrical Engineering Division, Department of Engineering, University of Cambridge, United Kingdom
[3]Italian Institute of Technology, Center for MicroBioRobotics, Viale Rinaldo Piagio 34, 56025, Pontedera, Italy
[4]Stratingh Institute for Chemistry, University of Groningen, Nijenborgh 4, 9747 AG Groningen, the Netherlands
[5]Zernike Institute for Advanced Materials, Nijenborgh 4, 9747 AG Groningen, the Netherlands
[6]Department of Chemistry and Nano-Science Center, University of Copenhagen, Copenhagen, Denmark
[7]Department of Molecular Chemistry and Materials Science, Weizmann Institute of Science, Rehovoth 7610001, Israel
[8]NNF Quantum Computing Programme, Niels Bohr Institute, University of Copenhagen, Denmark
[9]Department of Chemistry & Organic and Carbon Electronics Cluster, North Carolina State University, Raleigh, North Carolina 27695-8204, United States
*e-mail: ryan.chiechi@ncsu.edu

Contents

S1 Materials and Methods

All reagents were purchased from Sigma-Aldrich, Acros, TCI Europe or Boom and used as received unless otherwise stated. Triethylamine and $CHCl_3$ were distilled over CaH and P_2O_5 respectively, and used within 10 days. Anhydrous acetonitrile, toluene, dichloromethane (DCM), and tetrahydrofuran (THF), dimethylformamide (DMF) were obtained from a in-house Solvent Purification System. For non-anhydrous reactions, THF was stirred for 1 hour with basic alumina to remove BHT. For thin layer chromatography (TLC) Merck silica gel 60 F_{254} aluminium plates were used. Visualization of compounds by TLC were done by irradiation with UV light at 254 nm, iodine, potassium permanganate stain, or phosphomolybdic acid. Column chromatography was performed using Silicagel Kieselgel 60 M (0.04 - 0.063 mm, 230 - 400 mesh). ^{1}H NMR, ^{13}C NMR were performed on Agilent Technologies 400/54 Premium Shielded (400 MHz), Varian Oxford AS400 (400 MHz). Chemical shifts are reported in parts per million (ppm), relative to the solvent resonance of $CDCl_3$ (δ = 7.26 ppm for ^{1}H NMR and 77.0 ppm for ^{13}C NMR).

S2 Synthesis

We described the preparation of OPE3, and diSAc-OPE3 is described somewhere else.[Kaliginedi2012] The synthesis of OPE3 is described in our previous publication.[flowbox] mOPE3, OPPy3, and mOPPy3 are described in our recently published manuscript.[SLMpaper]

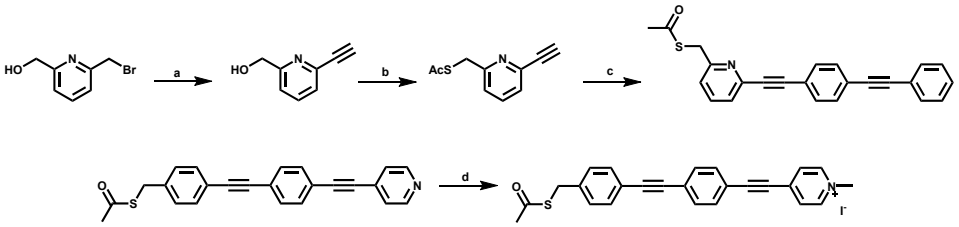

Figure S1: Reaction scheme for synthesis of mOPPy3 – 2, 6 and OPPy3 – *MeI*. *a*: i)TMS-acetylene, CuI, $Pd(PPh_3)_4$, Et_3N, THF; ii)TBAF, H_2O, THF; *b*: i)Et_3N, methanesulfonyl chloride, DCM; ii)KSAc, DMF; *c*: 1-bromo-4-(phenylethynyl)-benzene, $Pd(PPh_3)_4$, CuI, Et_3N, THF; *d*: CH_3I, CH_3CN. Note: write the molecular acronyms under structures

The synthesis of S-(4-iodobenzyl) ethanethioate is described in Ref. **andrew˙thesis**.

S2.1 mOPPy3 – 2, 6.

might decide to drop it out

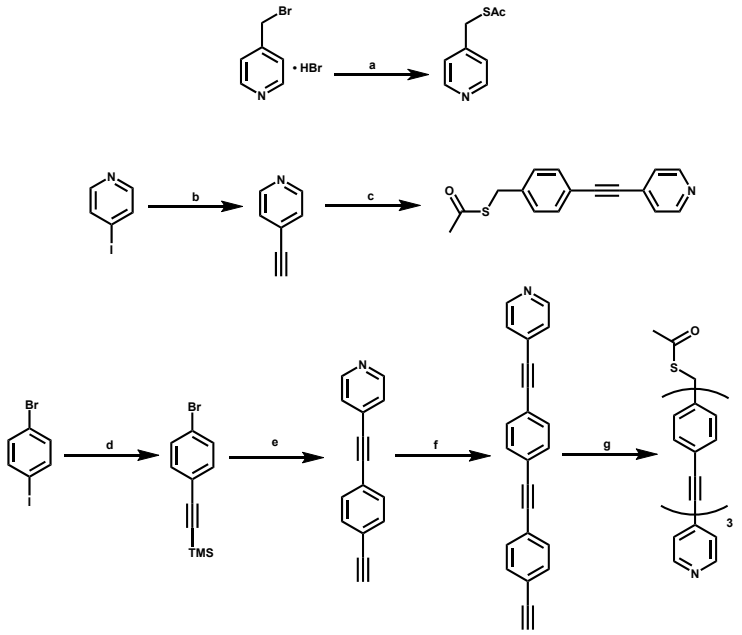

Figure S2: Reaction scheme for synthesis of mOPPy1, mOPPy2, mOPPy4.*a*:KSAc, H_2O;*b*: i)TMS-acetylene, $Pd(PPh_3)_4$, CuI, Et_3N; ii)TBAF, THF;*c*:S-(4-Iodobenzyl) ethanethioate, cePd(PPh3)4, CuI, Et_3N, THF;*d*:TMS-acetylene, $Pd(PPh_3)_4$, CuI, Et_3N, THF;*e*: i)4-ethynylpyridine, $Pd(PPh_3)_4$, CuI, Et_3N, THF; ii)TBAF, H_2O, THF;*f*: i)((4-bromophenyl)ethynyl)trimethylsilane, $Pd(PPh_3)_4$, CuI, Et_3N, THF; ii)TBAF, H_2O, THF;*g*: S-(4-iodobenzyl)ethanethioate, $Pd(PPh_3)_4$, CuI, Et_3N, THF. Note: write the molecular acronyms under structures

(6-ethynylpyridine-2-yl)methanol In an oven dry flask equipped with a condenser under N_2, 1.22 g of (6-bromopyridin-2-yl)methanol (6.38 mmol, 1.6 mL of (trimethylsilyl)acetylene (1.5 g, 1.15 mmol, 50 mg of CuI (0.26 mmol, 150 mg of $Pd(PPh_3)_4$ (0.13 mmol) and 7.1 mL of NEt_3 were dissolved in 30 mL of THF. The reaction was kept at reflux overnight. The solvents were removed under vacuum and the TMS-protected purified via

filtration through a short plug of silica using hexane/ethylacetate 1:1 to obtain brown oil (1.12 g, 89% yield). 935 mg of the latter (4.55 mmol) were dissolved in 40 mL in THF and the solution placed in an ice bath. 9.1 mL of a terbutylammonium fluoride solution 1 M in THF (9.1 mM) were added dropwise and the bath removed. After 20 hours, water was added to the solution which was then extracted with ehylt acetate. The organic phase was washed with brine and dried over Na_2SO_4. The final compound was purified via column chromatography (hexane/ethyl acetate, 1:1) to obtain pale yellow solid (542 mg, 90% yield).^{1}H NMR ($CDCl_3$, 400 MHz) δ 7.76 (t, J=7.8 Hz, 1H), 7.39 (d, J= 7.6 Hz, 1H), 7.28 (d, J=7.7 Hz, 1H), 4.75 (s, 2H), 3.28(s, br, 1H), 3.17(s, 1H) 13C NMR ($CDCl_3$, 101 MHz) δ HRMS m/z: ($[M+H]^+$) calculated for ; found .

S-((6-ethynylpyridin-2-yl)methyl)ethanethioate. In an oven dried flask under N_2, 300 mg of (6-ethynylpyridine-2-yl)methanol (2.26 mmol) and 0.5 mL of NEt_3 (343 mg, 3.4 mmol) were dissolved in 22 mL of DCM and the solution cooled in an ice bath. 0.21 mL of methanesulfonyl chloride (311 mg, 2.71 mmol) were added dropwise and the reaction left overnight. The solvent was removed under vacuum, the flask rapidly put under N_2, and the residue dissolved in 6 mL of dry DMF. The reaction was placed in an ice bath and 395 mg of Potassium thioacetate (3.46 mmol) added in portions over 1 hour. The bath was then removed and the reaction was stirred for 20 hours. Water was then added to the flask and the solution extracted with DCM. The organic phase was washed with water, LiCl aq. sat., and it was dried over Na_2SO_4. The product was purified via column chromatography (hex-

ane/ethyl acetate, 3:1) to obtain a dark yellow oil (344 mg, 80% yield). ^{1}H NMR ($CDCl_3$, 400 MHz) δ 7.60 (t, J=7.8 Hz, 1H), 7.35 (d, J=7.7 Hz, 1H), 7.34 (d, J=7.6 Hz, 1H), 4.24 (s, 2H), 3.15 (s, 1H), 2.35 (s, 3H).

1-bromo-4-(phenylethynyl)benzene To a flame dried Schlenk tube under inert atmosphere (N_2), 1 g of 1-bromo-4-iodobenzene (3.35 mmol), 150 mg of $Pd(PPh_3)_4$ (0.13 mmol), 50 mg of CuI (0.23 mmol) were dissolved in dry THF followed by addition of 4 mL) of Et_3N (28.2 mmol) and 400 mg of ethynylbenzene (3.89 mmol). The resulting mixture was stirred at room temperature for 18 hours and at 60 °C for 3 hours. After cooling down the mixture was diluted with water, extracted with DCM. The organic phase was washed with brine and dried over Na_2SO_4. The product was purified using column chromatography using gradient of pure hexane to 15% ethyl acetate in hexane. This yielded the product as white microcrystals (770 mg, yield 77%). ^{1}H NMR ($CDCl_3$, 400 MHz) δ 7.54-7.52 (m, 2H), 7.49 (d, J= 8.4 Hz, 2H), 7.40 (d, J= 8.4 Hz, 2H), 7.37-7.35 (m, 3H).^{1}3C NMR ($CDCl_3$, 101 MHz) δ 133.18, 131.77, 131.75, 128.57, 128.56, 123.06, 122.63, 122.41, 90.65, 88.45.

S-((6-((4-(phenylethynyl)phenyl)ethynyl)pyridin-2-yl)methyl)ethanethioate. In an oven dry flask equipped with a condenser under N_2, 200 mg of 1-bromo-4-(phenylethynyl)-benzene (0.78 mmol), 179 mg of S-((6-ethynylpyridin-2-yl)methyl)ethanetioate (0.93 mmol), 45 mg of $Pd(PPh_3)_4$ (0.04 mmol), 15 mg of CuI (0.08 mmol), and 1 mL of NEt_3 were dissolved in 5 mL of THF. The reaction was kept at reflux for two days. The final compound was

purified via column chromatography (hexane/ethyl acetate, 6:1) and recrystallized from hexane to obtain a pale yellow solid (4.1 mg, 2% yield). ^{1}H NMR ($CDCl_3$, 400 MHz) δ 7.64 (t, J=7.8 Hz, 1H), 7.58 (d, J=8.3 Hz, 2H), 7.55 - 7.50 (m, 4H), 7.24 (d, J=7.7 Hz, 1H), 7.38 - 7.33 (m, 4H), 4.28 (s, 2H), 2.37 (s, 3H)

S-(pyridin-4-ylmethyl) ethanethioate. In a round bottom flask, 100 mg of 4-(Bromomethyl)pyridine hydrobromide (0.395 mmol) were suspended in H_2O followed by addition of KSAc (99 mg, 0.87 mmol) and heated to 80 °C over night. The following day the reaction was cooled to room temperature, extracted with DCM, washed with brine and dried over $MgSO_4$. Product was obtained as a yellow oil after purification using column chromatography using pentane/ethyl acetate as eluent. ^{1}H NMR ($CDCl_3$, 400 MHz) δ 8.6 – 8.5 (m, 1H), 7.3 – 7.2 (m, 1H), 4.1 (s, 1H), 2.4 (s, 1H). 13C NMR ($CDCl_3$, 101 MHz) δ 194.45, 149.99, 147.10, 124.00, 32.34, 30.42. HRMS *m/z*: ($[M + H]^+$) calculated for $C_8H_{10}NOS$ 168.0478; found 168.0476.

S2.2 mOPPy1

S-(pyridin-4-ylmethyl) ethanethioate. In a round bottom flask, 100 mg of 4-(Bromomethyl)pyridine hydrobromide (0.395 mmol) were suspended in H_2O followed by addition of KSAc (99 mg, 0.87 mmol) and heated to 80 °C over night. The following day the reaction was cooled to room temperature, extracted with DCM, washed with brine and

dried over $MgSO_4$. Product was obtained as a yellow oil after purification using column chromatography using pentane/ethyl acetate as eluent. ^{1}H NMR ($CDCl_3$, 400 MHz) δ 8.6 – 8.5 (m, 1H), 7.3 – 7.2 (m, 1H), 4.1 (s, 1H), 2.4 (s, 1H). 13C NMR ($CDCl_3$, 101 MHz) δ 194.45, 149.99, 147.10, 124.00, 32.34, 30.42. HRMS m/z: ($[M + H]^+$) calculated for $C_8H_{10}NOS$ 168.0478; found 168.0476.

S2.3 mOPPy2

XXXXXXX

S-(4-(pyridin-4-ylethynyl)benzyl)ethanethioate, mOPPY2 In an oven dry Schlenk tube under N_2, 311 mg of S-(4-iodobenzyl) ethanethioate (1.1 mmol) and 127 mg of 4-ethynylpyridine (1.2 mmol) were dissolved in 10 mmol of dry THF. 67 mg of $Pd(PPh_3)_4$ (0.06 mmol), 28 mg of CuI (0.15 mmol) followed by 1 mL of freshly distilled NEt_3. The reaction was heated to 50 °C and left overnight. The reaction mixture was cooled down to room temperature and the solid was filtered off. The solvents were removed under vacuum and the orange solid was preadsorbed on silica. The crude was purified via column chromatography using hexane/ethyl acetate (3:1) and recrystallization from DCM/hexane to obtain the product (75 mg, 31% yield). NEEDS NMR DATA

S2.4 OPPy3*MeI*

4-((4-((4-((acetylthio)methyl)phenyl)ethynyl)phenyl)ethynyl)pyridin-1-ium iodide In a dry Schlenk tube under N_2, 43 mg of S-(4-((4-(pyridin-4-ylethynyl)phenyl)ethynyl)benzyl) ethanethioate (0.12 mmol) were dissolved in 15 mL of CH_3CN followed by addition of 0.5 mL of CH_3I (10 mmol) and left to react for 24 hours at 90 °C. The excess of CH_3I was removed under vacuum and Et_2O was added until precipitate was formed. The precipitate was recrystallized from a mixture of CH_3Cl and Et_2O kept in the freezer. NEEDS NMR DATA!

S2.5 mOPPy4

XXXXXXX

((4-bromophenyl)ethynyl)trimethylsilane In an oven dry flask, 5 g of 4-bromoiodobenzene (17.7 mmol), 32 mL of (trimethylsilyl)acetylene (24.4 g, 19.5 mmol), 150 mg of $Pd(PPh_3)_4$ (0.13 mmol), 50 mg of CuI (0.26 mmol) and 10 mL of NEt_3 were dissolved in 30 mL of THF. The reaction was left at room temperature over the weekend. It was then filtered in stirring hexane/water mixture and 6 M HCl was added until net acidity. The organic phase was washed with water, dried over Na_2SO_4, the solvent removed under vacuum. The crude was purified via column chromatography (hexane) to obtain pure product (2.61 g,

58% yield). ^{1}H NMR ($CDCl_3$, 400 MHz) δ 7.47 - 7.37 (m, 2H), 7.38 - 7.27 (m, 2H) 0.24 (s, 9H). ^{1}3C NMR ($CDCl_3$, 101 MHz) δ 133.35, 131.44, 122.71, 122.07, 103.83, 95.56, -0.14.

4-ethynylpyridine In an oven dry Schlenk tube under N_2, 2 g of 4-iodo-pyridine (9.8 mmol, 2 mL of (trimethylsilyl)acetylene (1.42 g, 15 mmol), 150 mg of $Pd(PPh_3)_4$ (0.13 mmol), 50 mg of CuI (0.26 mmol) were dissolved in 10 mL of NEt_3. The reaction was left at 60 °C over the weekend. The solvent was removed under vacuum and the residue extracted with hot hexane. The TMS-protected compound was purified by filtration over a short plug of silica using hexane/ethyl acetate (5:1) and obtained as a brown oil (1.42 g, 83% yield). The latter was dissolved in 70 mL of THF and the solution was placed in an ice bath. 9.6 mL of a tetrabutylammonium fluoride solution (1 M in THF, 9.6 mmol) and 0.48 mL of H_2O were added dropwise and the bath removed. After 25 minutes, the solution was dried with Na_2SO_4 and the product preadsorbed on silica. The final compound was purified via filtration over a short plug of silica using hexane/ethyl acetate (3:1) to obtain white flaky crystals (440 mg, 35% yield over 2 steps) which were immediately used in the next step. ^{1}H NMR ($CDCl_3$, 400 MHz) δ 8.60-8.53 (m, 2H), 7.36 - 7.28 (m, 2H) 3.28 (s, 1H)

4-((4-ethynylphenyl)ethynyl)pyridine In a dry Schlenck tube under N_2, 420 mg (4.1 mmol) of 4-ethynylpyridine and 1.0 g of ((4-bromophenyl)ethynyl)trimethylsilane (4 mmol) were dissolved in 10 mL of dry THF. To the solution, 180 mg of $Pd(PPh_3)_4$ (0.16 mmol), 50 mg of CuI (0.26 mmol) and 4.5 mL of NEt_3 were added and the reaction

was left overnight at 60 °C. The solvent was removed under vacuum and the crude adsorbed on silica. The crude was purified via column chromatography using hexane:ethyl acetate (3:1) and the product was obtained as yellow crystals (473 mg, 42% yield). The product was dissolved in 40 mL of THF (not stabilized with BHT). The yellow solution was degassed and placed in a ice bath. 0.09 mL of H_2O was added, followed by 1.8 mL of 1 M tetrabutylammonium fluoride solution in THF (1.8 mmol). The ice bath was removed and the reaction was left to stir for 25 minutes before removing the solvent under vacuum. The yellowish crude was dissolved in $CHCl_3$ and adsorbed on silica prior to purifying it via column chromatography using hexane/ethyl acetate (2:1) to obtain the product as white solid (231 mg, 71% yield). NEEDS NMR DATA!

4-((4-((4-ethynylphenyl)ethynyl)phenyl)ethynyl)pyridine In a dry Schlenk tube under N_2, 220 mg of 4-((4-ethynylphenyl)ethynyl)pyridine (1.08 mmol) and 271 mg ((4-bromophenyl)ethynyl)trimethylsilane (1.08 mmol) were dissolved in 10 mL of dry THF. To the reaction, 150 mg of $Pd(PPh_3)_4$ (0.13 mmol), 50 mg of CuI (0.26 mmol) and 3 mL of freshly distilled NEt_3 were added. After the reaction was left overnight to react at 60 °C, the reaction mixture was cooled to room temperature and the solvent was removed under vacuum. The crude was preadsorbed on a silica and purified via a silica plug (hexane/ethyl acetate, 2:1) in order to obtain the product as off-white crystals (299 mg, 74% yield). 235 mg of 4-((4-((4-((trimethylsilyl)ethynyl)phenyl)ethynyl)phenyl)ethynyl)pyridine (0.63 mmol) was dissolved in 50 mL of THF (not stabilized with BHT). The reaction flask was cooled in ice bath be-

fore adding 0.03 mL of H_2O and 0.69 mL of 1 M of tetrabutylammonium fluoride in THF (0.69 mmol). After removal of the ice bath, the reaction mixture was left to stir for 30 minutes before adding Na_2SO_4 and filtering it. The crude was preadsorbed on silica prior to purification via silica plug using hexane/ethyl acetate (3:2) and obtaining the product as white crystals (125 mg, 65% yield). NEEDS NMR DATA!

S-(4-((4-((4-(pyridin-4-ylethynyl)phenyl)ethynyl)phenyl)ethynyl)benzyl) ethanethioate In a dry Schlenk tube under N_2 125 mg of 4-((4-((4-ethynylphenyl)ethynyl)phenyl)ethynyl)pyridine (0.41 mmol) and 132 mg of S-(4-iodobenzyl) ethanethioate (0.45 mmol) were dissolved in 10 mL of dry THF followed by addition of 50 mg of $Pd(PPh_3)_4$ (0.04 mmol), 20 mg of CuI (0.11 mmol) and 0.5 mL of dry Et_3N and left to react overnight at 60 °C. The solvent was removed under vacuum and the crude was preadsorbed on silica. The product was purified via silica plug (hexane/ethyl acetate, 1:1) followed by recrystallization from toluene in order to obtain it a as light yellow solid (60 mg, 31% yield). NEEDS NMR DATA!

S2.6 UV-Vis Absorbance Spectroscopy

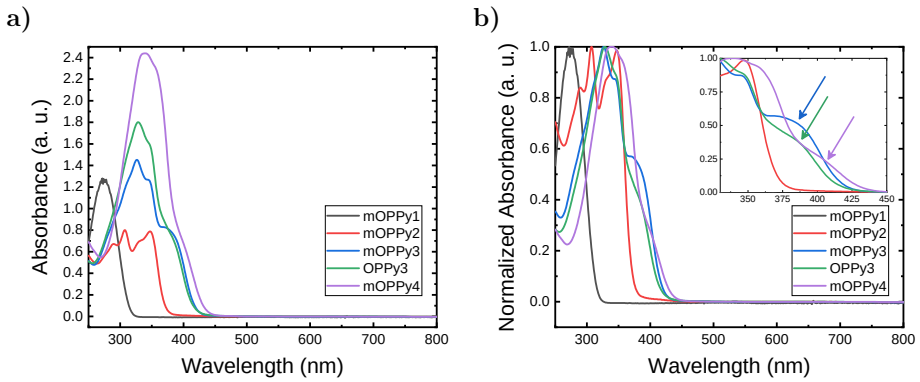

Figure S3: (a) UV-Vis absorbance spectra of OPPy3 and mOPPyn for $n = 1$ to 4. (b) Normalized UV-Vis absorbance of the same molecules, with the inset showing the zoomed-in version of the λ-onset region along with arrows indicating the extra peak which are absent in mOPPy1 and mOPPy2. The extracted bandgaps are shown in Table S1.

UV-Vis spectra of all the measured compounds were obtained using Shimadzu UV-3600 spectrometer from 50 µM solutions in chloroform solvent with the wavelengths ranging from 250 to 800 nm. The spectra are shown in Figure S3 and the extracted bandgaps are tabulated in Table S1. As can be seen from mOPPy1 and mOPPy2 show an absence of the extra peak that is present in mOPPy3 and OPPy3 at ≈385 nm and mOPPy4 at ≈400 nm. These peaks are indicated using arrows in the inset of Figure S3b. The values of the optical bandgaps extracted from the onset of UV-vis absorbance are reported in Table S1.

Table S1: Bandgaps (E_g) of the molecules investigated in this study: mOPPyn (for $n = 1$ to 4) and OPPy3. The UV-Vis spectra are shown in Figure S3.

Molecule	UV-Vis Bandgap (eV)
mOPPy1	3.23
mOPPy2	3.35
mOPPy3	2.95
OPPy3	2.97
mOPPy4	2.86

S3 Fabrication of Self-assembled Monolayers

Template-stripped metal substrates were prepared by depositing a 100 nm-thick layer of Au on a Si wafer. 1x1x0.3 cm glass slides were glued to the deposited metal using an UV-curable optical adhesive (Norland series 60). The samples were cleaved from the wafer with the help of a razor and immediately used. SAMs of the compounds in this Chapter were prepared in dry toluene solutions by *in situ* deprotection using DBU according to a known procedure.[flowbox]

The SAMs of were formed via *in situ* deprotection of the anchoring thioacetate groups to form thiols[Valkenier2011, Carlotti2016] on template-stripped Au substrates (Au^{TS}, surface topography scans are shown in Figure S4).[weiss2007si, chiechi2008eutectic, Liu2020] Same process to fabricate SAMs on template-stripped Au (Au^{TS}) substrates was followed as from our previous study.[flowbox] Briefly, we incubated Au^{TS} (100 nm-thick) substrates in 3 mL of 50 µM solution (using extra-dry Toluene solvent) of thioacetate precursors of all the measured compounds overnight under N_2 atmosphere. This was followed by addition of 0.05 mL of 17 mM diazabicycloundec-7-ene (DBU) solution in toluene 90 min prior to the measurement inside a flowbox environment ($O_2 = 1 - 3\%$ and relative humidity $< 10\%$). The SAMs were then rinsed with 3 mL absolute Ethanol inside flowbox as well and left to dry for 15 min before starting the measurements.

The SAMs were characterized by water contact angle and X-ray photoelectron spec-

troscopy. SAMs of $CH_3(CH_2)_{17}SH$ on Au (on mica) were used as a reference.

S4 Atomic Force Microscopy

We used the ScanAsyst mode of the Bruker Multo-Mode AFM instrument to scan surface topology and measure root mean square (RMS) roughness of substrates with and without SAMs grown on them. Scanasyst analysis software by Bruker was used to analyze the data. We used the silicon nitride tips, purchased from Bruker, of the ScanAsyst-air probe series. The cantilever with resonant frequence of 40 kHz was chosen and the scans were recorded at 0.7 Hz frequency recording 512 samples per line. The surface morphology scans are shown in Figure S4a and b for two different scan sizes and the RMS roughness values are tabulated in Table S2.

Table S2: AFM roughness of measured samples.

	Au^{TS}	mOPPy1	mOPPy2	mOPPy3	mOPPy4	OPE3
500×500 nm	0.31	0.28	0.45	0.26	0.37	0.63
2×2 μm	0.39	0.45	0.54	0.45	0.50	0.76

As can be seen in Figure S4 and Table S2, compared to the bare Au^{TS}, the RMS roughness only varies slightly, suggesting a uniform passivation of the metal surface with only few impurities present on the surface, which we regard to environmental impurities or

impurities from surface. Unlike the scans for the bare Au^{TS} substrate, which show several flat islands on the polycrystalline gold surface, the SAM-passivated surfaces show no such features, albeit, a more amorphous morphology but with similar average roughness.

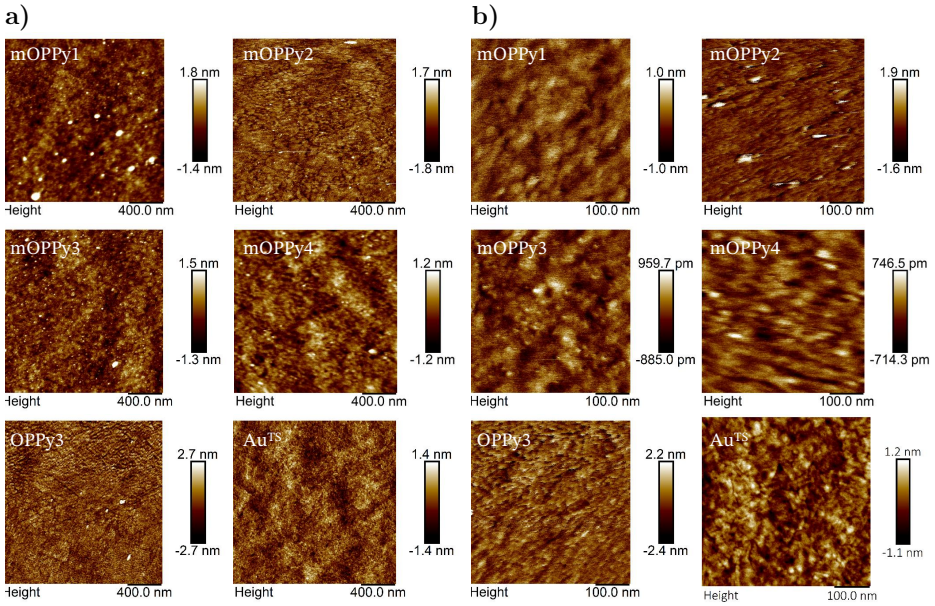

Figure S4: AFM surface scans of SAMs of molecules under study in this work along with that of a bare Au^{TS} substrate showing islands of atomically-flat gold atoms for different scan sizes: a) 500x500 nm and b) 2x2 μm. The root mean square roughness of all the substrates are shown in Table S2.

S5 Water Contact Angle Measurements

The water contact angles were measured using a home-built optical camera from Edmond, same as the one used for EGaIn measurements. MiliQ pure water was contacted by squeezing 1 µL drop out of a 10 µL syringe, which was lowered to wet the substrates. The captured

images were then analyzed using the imageJ software.[Rueden2017] Both left and right water contact angles of the drops were measured and averaged. Three to four different spots were measured per sample and two samples were used per molecule. The averaged values of contact angles were reported with standard deviations. We also measured freshly-stripped bare Au^{TS} substrate ($\approx 65°$)[Erb1968] and a polystyrene surface ($\approx 89°$)[Li2007] to establish the validity of our setup.

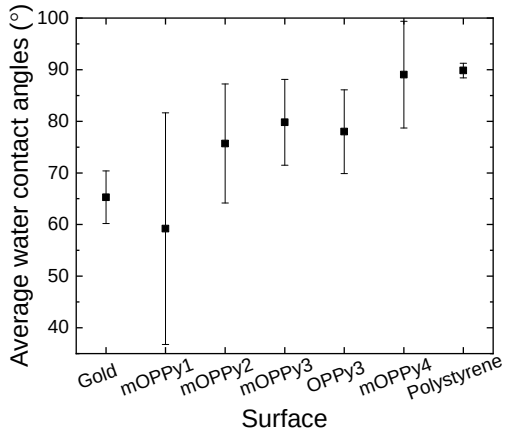

Figure S5: Average water contact angles of SAMs of molecule under study in this work on Au^{TS} substrates along with that of freshly-stripped bare Au^{TS} and polystyrene as controls.

S6 Ellipsometry Measurements

Measurements performed by Mike, have to add data but not sure if the thickness data is very useful/reliable, also considering we will get thickness data also from sumit. Ellipsometry data was acquired by measuring samples using a V-Vase Rotating analyzer and a HS-190

monochromator ellipsometer from J.A. Woollam Co. For every molecule two to three samples and for each sample two areas were measured. All measurements were performed at incident angles of 60°, 65° and 70° with respect to the surface normal and wavelengths ranged from 300 to 1700 nm. The data was fitted by to a two-layer model. Optical constants for the bottom Au layer were obtained by fitting data from a fresh prepared Au^{TS}. The top Cauchy layer was used to fit the thickness and the k-amplitude of the SABs. The coefficients in the real part of the complex refractive index in the cauchy model were chosen as $A_n = 1.55$ and $B_n = C_n = 0$. The data was fitted at 350 to 600 nm and 600 to 1400 nm. The combined average thickness and k-amplitude of the two regions are reported with standard deviation.

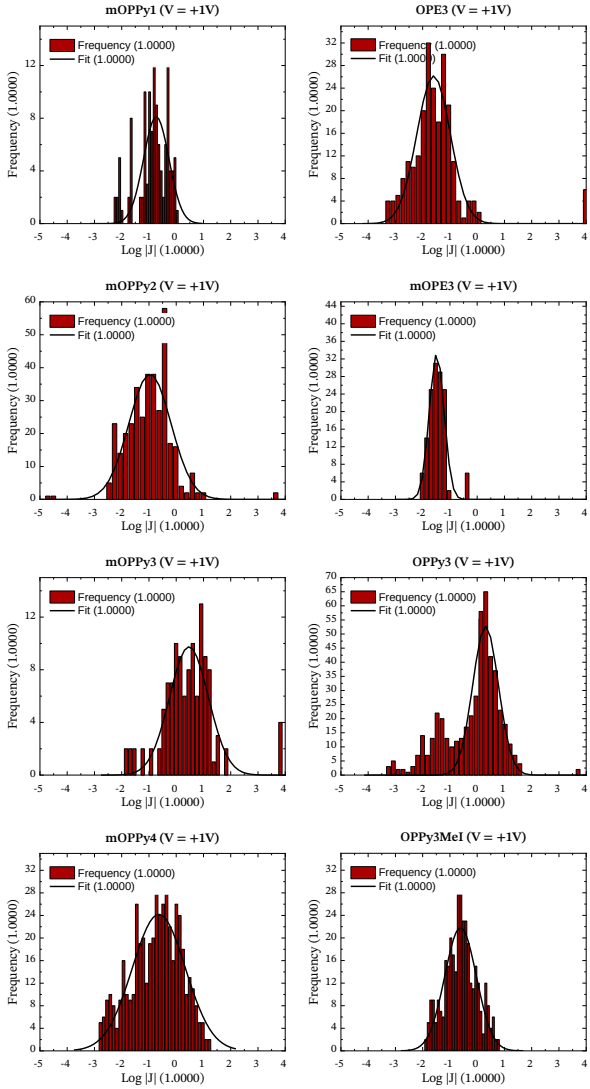

Figure S6: Histograms of $\log|J|$ for V = 1 V for the molecules under study in this work. The gaussian fitting is shown with black lines while the raw histograms from raw $J-V$ data are shown in red column bars.

S7 EGaIn Measurements and Data Analysis

The details of the EGaIn instrument are described in our previous publication.[flowbox] Regarding the data acquisition, we measured 3-4 substrates for each compound, with 10- 12 Au^{TS}/SAM//Ga_2O_3/EGaIn junctions per substrate, and 5 scans (*i.e.*, 10 traces) per junction. The junctions were first checked for shorts by applying a 0.5 V bias before contacting the EGaIn tip to the SAM. The scans were then ramped from 0 V $\rightarrow$ 1 V $\rightarrow -1$ V $\rightarrow$ 0 V (with steps of 0.05 V, at 0.1 s delay between each datum), exact numbers are tabulated in Table S3. A new EGaIn tip was prepared after every 6^{th} working junction *i.e.*, at least two new tips per substrate. A short was reported whenever the ohmic conductance was recorded in any one of the 5 scans during the measurement. We have reported the yield of working junctions also in Table S3. The data were acquired as described and then parsed in a "hands-off" manner using Scientific Python to produce histograms of J for each value of V and the associated Gaussian fits (using a least-squares fitting routine), as shown for V = 1 in Figure S6. The python code used for the analysis can be obtained from https://github.com/rchiechi/GaussFit. The data for OPE3 and mOPE3 were already presented elsewhere[flowbox, SLMpaper] and their values adjusted for the new series resistance of the new instrument by calibrating them using internal standards. The error bars are reported as the 95 % confidence intervals, from σ_{logJ} (standard deviation) taken from Gaussian fits, using the number of degrees of freedom as $N_{\text{junctions}} - 1$.

Table S3: Summary of number of measured working MEJs with EGaIn top electrode. The number of traces for every compound would be the number of junctions times 10. OPE3 and mOPE3 is taken from our previous work.[flowbox, SLMpaper]

Molecule	Yield of working junctions (%)	Num. of working EGaIn junctions
mOPPy1	90%	36
mOPPy2	87.8%	36
mOPPy3	88%	36
mOPPy4	85.7%	48
OPPy3	87.1%	54
OPPy3MeI	92.1%	35
OPE3[flowbox]	93%	20
mOPE3	52%	29

S7.1 Low-bias conductance

Low-bias conductance were obtained by computing the slope of EGaIn data (J vs. V) for the lowest 4 data points, *i.e.*, from $-0.1\,\mathrm{V}$ to $0.1\,\mathrm{V}$. This was done by fitting a linear equation to the linear $J-V$ data. The standard deviation of the slope from the linear fitting served as the error in the low-bias conductance values.

S7.2 Normalized Differential Conductance Heatmap

The raw $J-V$ curves were smoothed by the polynomial model and the derivative of the current density (J) relative to the voltage (dJ/dV) were computed individually from the individual curves in raw $J-V$ data. Normalized differential conductance (NDC) was calculated as NDC $= (dJ/dV)/(J/V)$. Then we constructed a 2D histogram of these NDC values by logarithmically binning them for each bias voltage and plotting them, resulting in

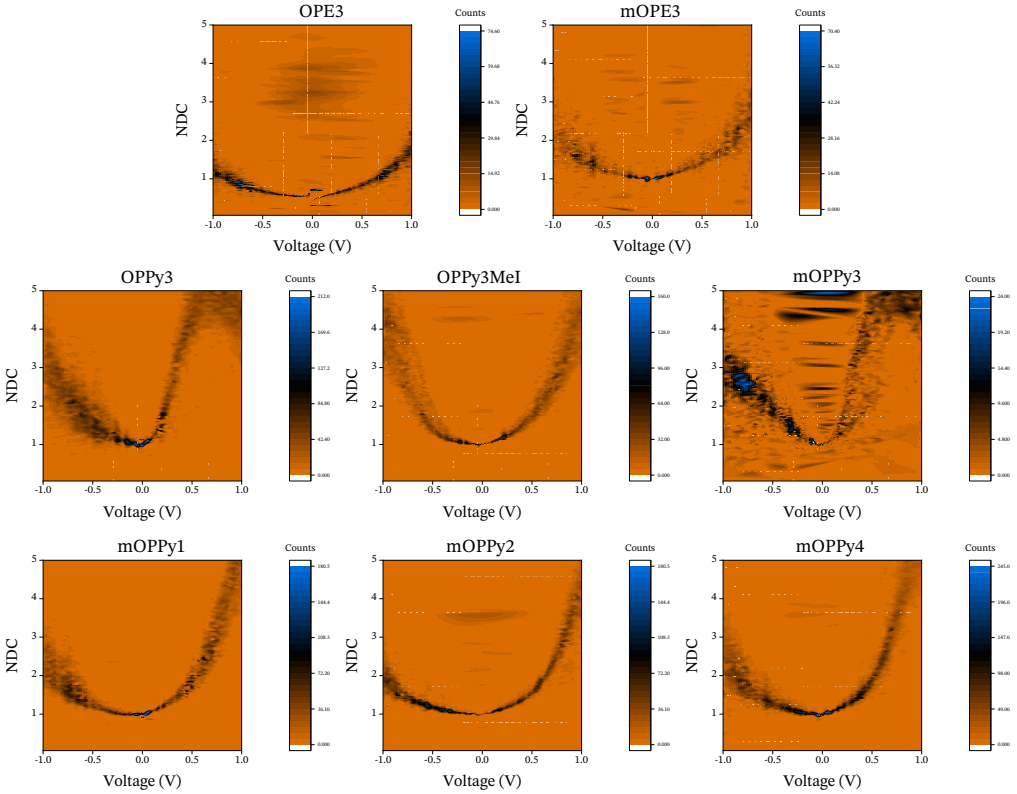

Figure S7: NDC heatmaps of molecules under study showing NDC on y-axis, voltage on x-axis and counts on the color scale.

a heatmap with the voltage on the x-axis, NDC on the y-axis and (in color scale) the number of counts on the z-axis. The heatmaps for all of the molecules under study and the controls are shown in Figure S7, while the gaussian means and error bars corresponding to the 95% confidence intervals are shown in Figure 2e and f in the main text.

In our previous work[Zhang2018] and also in other works, such as Han *et al.*,[Han2020] it was asserted that just like the density of states spectra from scanning tunneling microscopy

measurements, peaks in NDC can suggest the presence of energy levels in the tunneling barrier coming into resonance with the Fermi level of the electrodes. We report this for both OPPy3 and mOPPy3 as a clear peak is visible for $V > 0$. While the shapes of the NDCs for rest of the molecules are parabolic, except for mOPPy4 which shows a small peak very close to $V = 1$ and for OPPy3MeI which shows a peak at the edge of the bias window too at $V = -1$. These features are consistent with the peaks in the simulated transmission spectra of these molecules, as are discussed later in this article.

S7.3 Transition voltage spectroscopy

Transition voltages were calculated using the GaussFit python script described above. Every individual raw $J - V$ curves were re-plotted as Fowler-Nordheim plots ($\ln|J/V^2|$ vs. $1/V$) and the voltage corresponding to the minimum of the curve was extracted. A histogram was constructed of all the minimas from raw data for every molecule and a gaussian fitting was performed to yield the mean value of V_{trans} and standard deviation as error for both V ¿ 0 and V ¡ 0. The values are shown in Figure S8 with confidence intervals as the error bars and also tabulated in Table 1 in the main text.

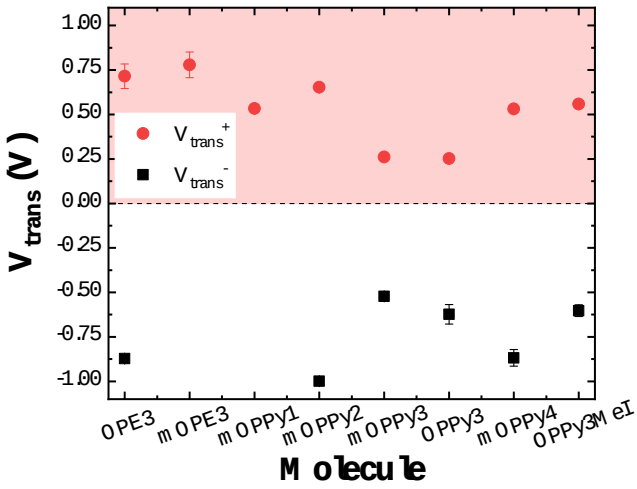

Figure S8: Transition voltage values plotted for negative ($V_{\text{trans}}{}^{-}$, black squares) and positive bias window ($V_{\text{trans}}{}^{+}$, red circles) for the molecules under study in this work.

S8 XPS Measurement

Sumit has data for mOPPy2. mOPPy4, mOPPyMeI that he will add. for OPPy3 and mOPPy3 has already been added to the SLM paper. He will also estimate the SAM thickness from the XPS data.

S8.1 Angle-resolved XPS thickness measurement

Angle-resolved XPS (ARXPS) measurement were performed using a VG Microtech spectrometer with a hemispherical electron analyzer (Clam 100), and a MgKα(1253.6 eV) X-ray source. Operation of the measurement and Data analysis are following the method stated in the experimental section in a previous paper.[Qiu2017] Here we only pointed out the different part from that paper. The Au 4f peaks and C 2p were acquired with the sample rotated under 0, 5, 10, 15, 20, 25, 30, 40 and 50 degrees with respect to the electron analyzer. An expression for the intensity of the peaks for different lengths of the path that through the overlayer:

$$[h!]I(\phi) = I_0 \exp(\frac{-L}{\phi}) = I_0 \exp(\frac{-d}{\lambda \cos(\phi)}) \tag{S1}$$

with L the length of the path through the layer, d the thickness of the layer, λ the

inelastic mean free path, ϕ the angle of rotation of the sample with respect to the analyzer, I_0 is the corrected peak intensity. The corrected peak intensity I^* are obtained by the $I^* = \gamma_1 \, I$ and can be used to determine the thickness of the layer. In the measurement, **C18SH** is used as the reference whose length is known as 20.9(2) Å.[Sch00] Then the λ value can be calculated. Next we can make a fit to the corrected intensities to find the thickness of the five Acene SAMs. Some of the samples indicated the presence of residual DBU from the in situ deprotection during the growth of the SAMs that increased the apparent thickness of the SAM slightly. These trace amounts of DBU do not impact the EGaIn measurements because they occur infrequently and randomly and, because we measure many junctions across many substrates, they show up as low-frequency outliers in the conductance histograms; however, they are over-represented in the AR-XPS because we measured fewer substrates and XPS is very sensitive to small amounts of impurities. We do not know the cause of the residual DBU, as it appears to be unique to the acene series.

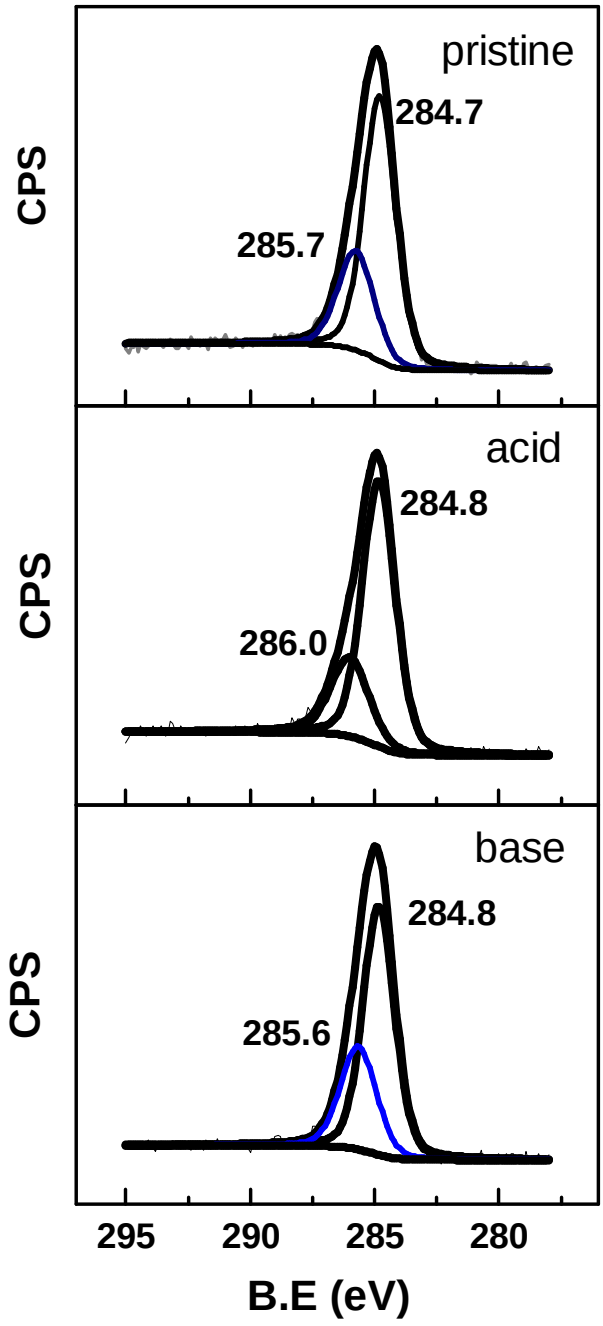

Figure S9: XXXX

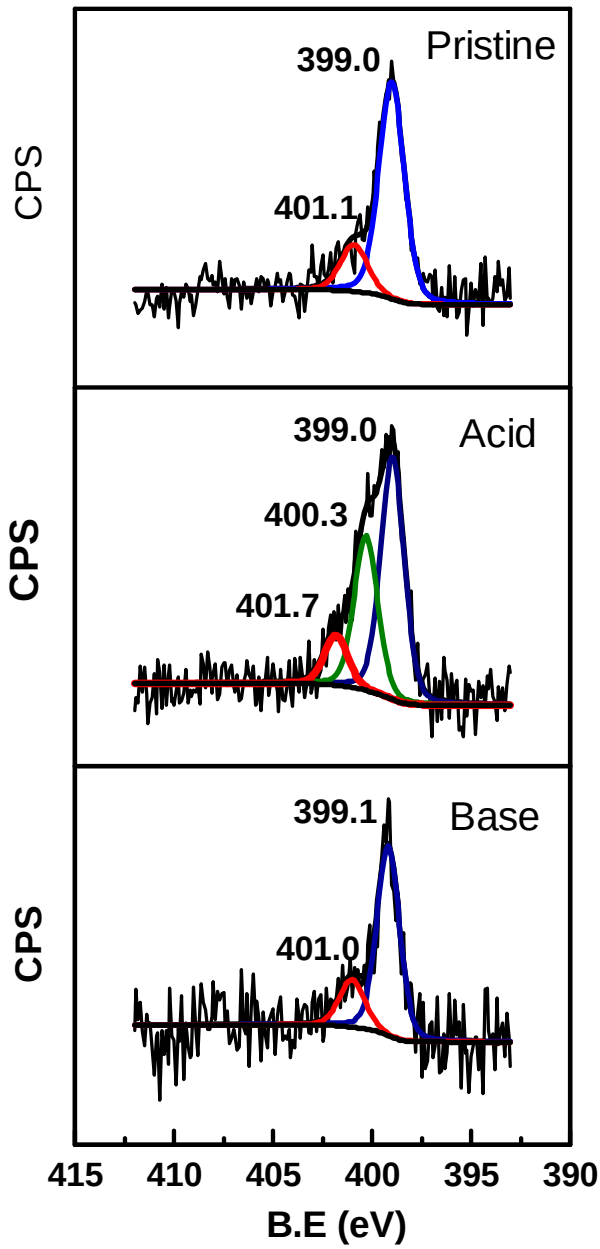

Figure S10: XXXX

S9 Computational results

The molecular orbitals at 0 V of OPPy2, OPPy3, OPPy4 and OPPy5 can be seen in Fig. S11. It illustrates how the HOMO(left side) is localized towards the S and the LUMO(right side) is localized towards the N. The top layer of the electrode are not a part of MO ist is purely there to show that the MO are calculated for the molecule in the junction. The MOs are calculated for the molecule in the junction by projecting the MO only on the molecule atoms.

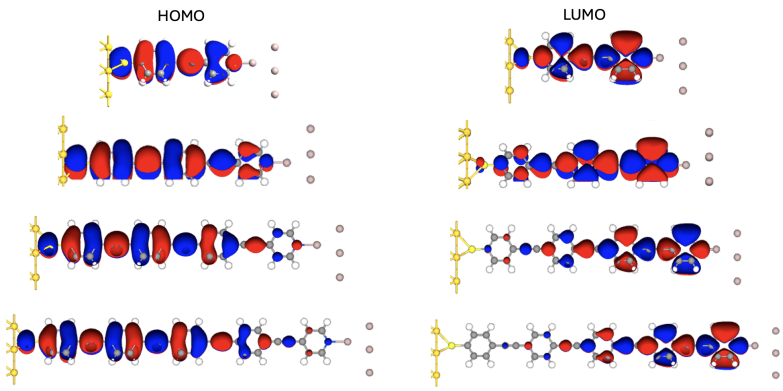

Figure S11: Illustration of the HOMO and LUMO at 0 V for OPPy2, OPPy3,OPPy4 and OPPy5, from top to bottom, respectively.

In Fig. S12 left, the HOMO and LUMO energies at 1 V, 0 V and −1 V are shown for OPPy2, OPPy3, OPPy4 and OPPy5. The bias is on the y axis and the energy in eV is on the x axis. The Fermi level is at 0 eV and is shown with a dotted black vertical line. The LUMO peak (triangles) move with bias as show in the main paper, whereas the HOMO peak

seem to be affected less by the bias.

In Fig. S12 right, the x and y axis are flipped (Energy on the yaxis and Bias on the xaxis) to show the HOMO-LUMO gaps. This aims to show how the HOMO-LUMO gap is changing with the bias. The HOMO-LUMO gap for the different molecules are more spread out at 1 V than at −1 V. This is consistent with the working principle of a MEJ, as mentioned in the main paper.

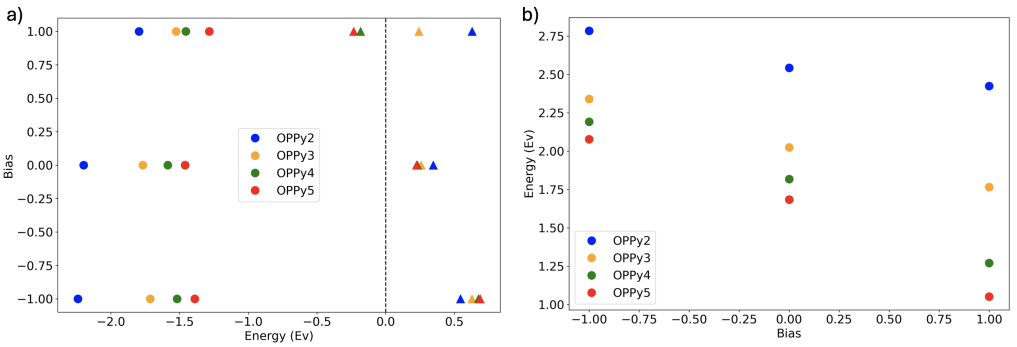

Figure S12: Illustration of HOMO and LUMO energies, as well as the energy gap, for OPPy2 (blue), OPPy3 (orange), OPPy4 (green), and OPPy5 (red). (a) HOMO and LUMO energies at −1 V, 0 V and +1 V, with energy (eV) on the y-axis and bias (V) on the x-axis. The black vertical dotted line indicates the Fermi energy. (b) HOMO-LUMO gaps plotted at −1 V, 0 V, and 1 V, here with energy (eV) on the y-axis and bias (V) on the x-axis.

When comparing the dipole moment and the current, it is essential to understand the direction of the current. At postive current (1 V), the current (defined as the flow of positive charge) flows from left to right, aligning with the Z direction, as shown in Fig. S13. This corresponds to the current flowing from the sulfur side of the molecules to the nitrogen side. The direction of an electric field between two plates is from positive to negative; therefore, to mimic the positive bias, the right plate (sulfur side) is set to 0 V, and the left plate (nitrogen

side) is set to $-1\,\mathrm{V}$. This results in an electric field from S to N, again aligning with the Z direction in Figure 3. The opposite holds for the negative bias across the junction. Here, the current flows opposite to the Z direction, from the nitrogen side of the molecule to the sulfur side. The corresponding electric field then has 0 V at the left plate and $+1\,\mathrm{V}$ at the right plate. It is important to note that in all cases, the movement of electrons will be opposite to the direction of the electric field and the current in the junction. Consequently, the entire picture can be "flipped" when discussing the movement of electrons.

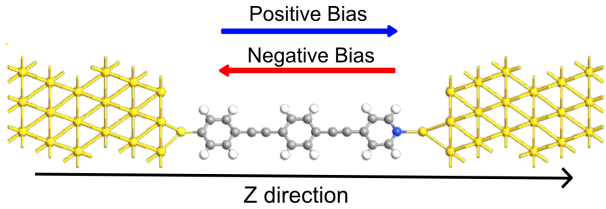

Figure S13: Illustration of the direction of positive and negative current across a junction.

S9.1 Au vs. Al top electrode

In the main paper, we highlight the importance of choosing the right electrodes when simulating experiments involving top electrodes other than Au. In Fig. S14, the two junctions compared in this section are shown. The top panel of Fig. S14 illustrates the Gold (Au)-molecule-Aluminium (Al) junction and the bottom panel shows the Gold (Au)-molecule-Gold (Au) junction, both with OPPy3 in the junction. From this point forward, these junctions will be referred to as Au-Al and Au-Au, respectively.

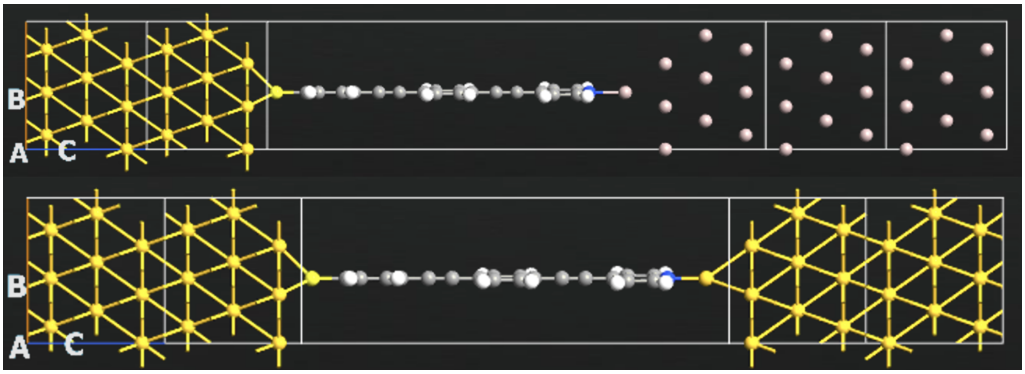

Figure S14: Illustration of the Au-Al junction (top) and the Au-Au junction (Bottom).

To investigate the influence of the top electrode, the IV curves for both the Au-Al and Au-Au junctions were calculated for all molecules, as shown in Fig. S15a,b. Rectification is observed for both top electrodes, though notable differences exist between the two junctions. The Au-Al junction exhibits higher current for OPPy2 and OPPy3 compared to the Au-Au junction. Additionally, OPPy2 rectifies in the opposite direction to the other molecules in the Au-Au junction, whereas it shows little to no rectification in the Au-Al junction. OPPy4

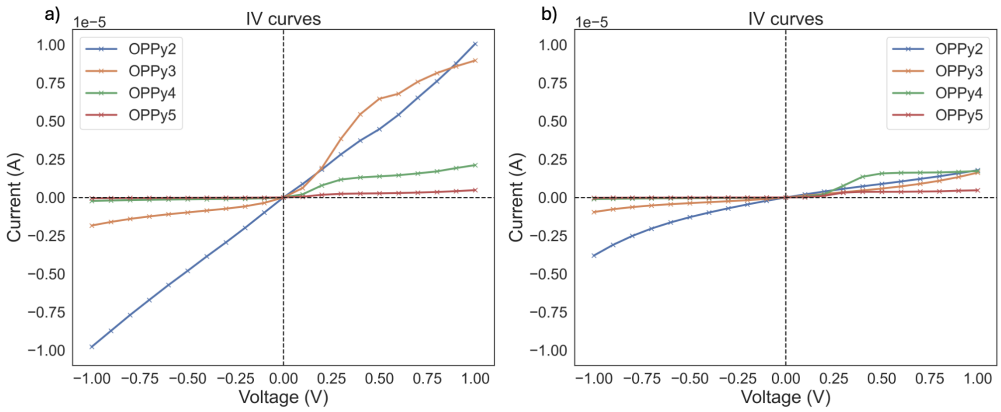

Figure S15: Calculated IV curves of OPPy2 (blue), OPPy3(orange), OPPy4(green) and OPPy5(red) for Au-Al junction (a) and the Au-Au junction (b).

and OPPy5 appear to be less affected by the choice of electrode; in both cases, they exhibit low current and rectify in the same direction.

Since the IV curves can be challenging to compare, we plotted the rectification ratio in Fig. S16. The rectification was calculated as $J+/J-$, where $J+$ is the forward bias (+1 V) and $J-$ is the reverse bias (−1 V). In Fig. S16a,b, the rectification is plotted as log(R) vs. voltage. Figure S16a shows the rectification of the molecules in the Au-Al junction, while Fig. S16b shows it for the Au-Au junction. As observed in the IV curves, OPPy2 rectifies in the opposite direction when the top electrode is Au, which is clearly illustrated in Fig. S16d. Here, the rectification at 0.1 V (triangle) and 1.0 V (circle) is shown for each molecule, with the black dotted line representing zero. When the rectification is negative, the molecule rectifies toward −1 V, meaning more current is observed at −1 V than at +1 V, and vice versa when the rectification is positive.

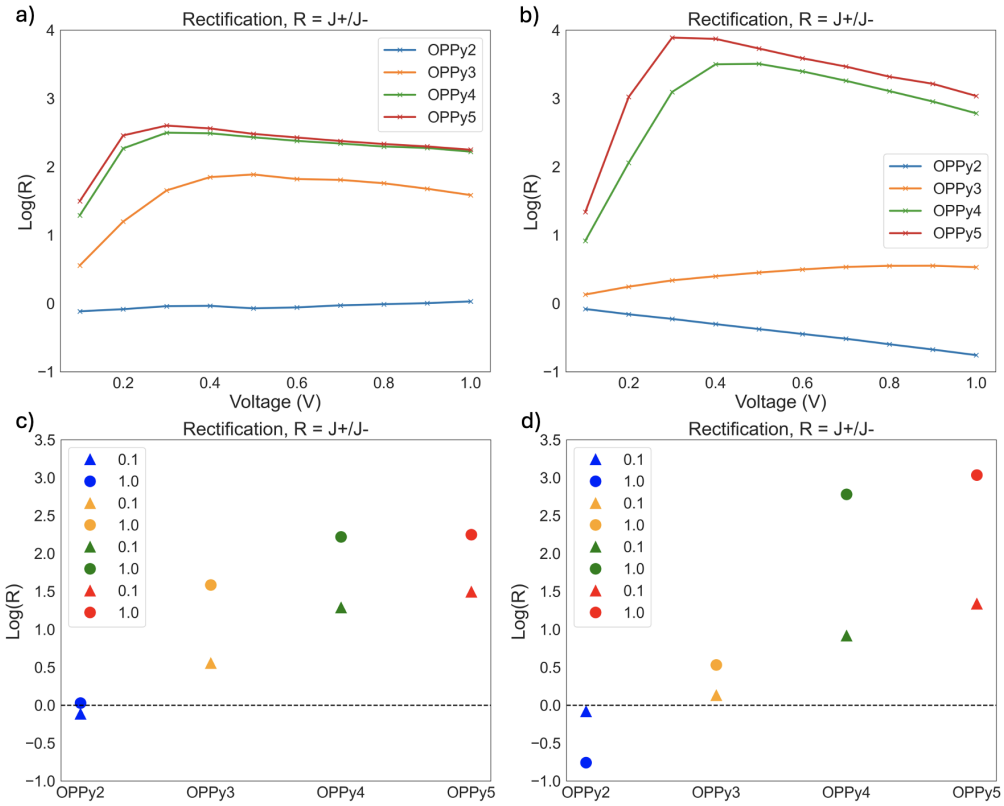

Figure S16: Illustration of the rectification ratio for Au-Al (a, c) and Au-Au (b, d) junctions for OPPy2 (blue), OPPy3 (orange), OPPy4 (green), and OPPy5 (red). The rectification (R) is calculated as $J+/J-$ and plotted as log(R) vs. voltage (V). Panels (a, b) show the rectification at each bias point, while panels (c, d) display the rectification at 0.11 V (triangle) and 1.0 V (circle) for each molecule.

Since the current is calculated from the transmission, it is useful to compare the change in transmission at ± 1 V for the two junctions. Fig. S17 shows the transmission for the Au-Al and Au-Au junctions at -1 V (Fig. S17a) and $+1$ V (Fig. S17b). At -1 V, the LUMO peak is located at approximately the same energy in both cases. However, at $+1$ V, the LUMO peak for the Au-Al junction shifts down in energy into the bias range, resulting in higher

current and greater rectification.

As mention in the main paper the choice of Al as the top electrode to simulate the EGaIn electrode is based on the similarity in their workfunction.[AlWF, EgainWF] We do note that in QuantumATK, when the electrodes are different, their Fermi levels are not initially aligned. In the calculations, the Fermi level of the right electrode is adjusted so that the Fermi levels align at zero bias. Therefore, we emphasize that when comparing results between junctions with different electrodes, they may be less comparable than one might expect.

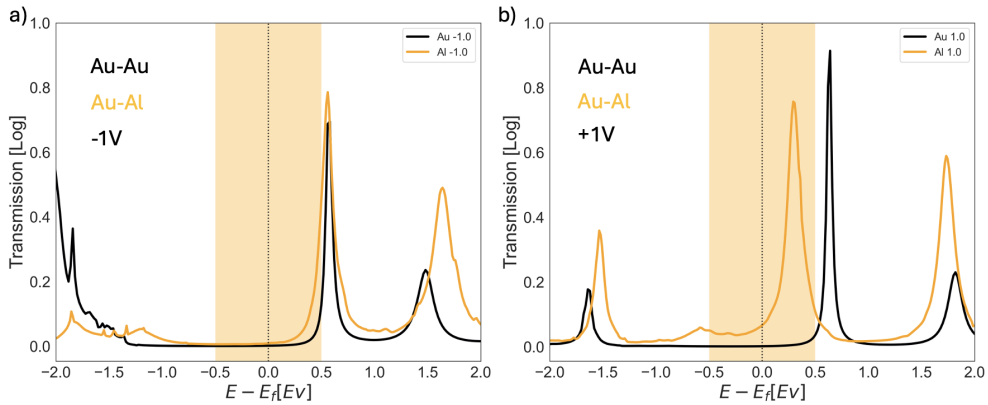

Figure S17: Comparison of the transmission for OPPy3 at $-1\,\mathrm{V}$(a) and $+1\,\mathrm{V}$(b) of the Au-Au(black) and Au-Al(orange) junction. The orange shade corresponds to the bias window.

These results demonstrate a difference between the two top electrodes, though we cannot quantify the extent of this difference. Overall, it remains an open question whether Au-Au junctions can be expected to exhibit qualitatively similar transport properties to Au-EGaIn junctions, or if these findings suggest otherwise. This may indicate the importance of using an alternative top electrode, such as Al, in theoretical calculations to better simulate

experiments involving EGaIn.

S9.2 Binding group choice

As mentioned in the main paper, the choice to use Au−S instead of Au−S−CH_2 was based on the simpler geometry and fewer degrees of freedom. In Fig. S18 and Fig. S19 a comparison of mOPPy3 and OPPy3 with the Al top electrode (Fig. S18) and Au top electrode (Fig. S19) are shown.

We observe qualitative agreement between the two different binding groups for Au-Al, though at 0 V and +1 V, the LUMO peaks appear at different energies. As mentioned in the main paper, the current is calculated from the area under the transmission curve within the bias window. Since the peaks fall within this window, we expect rectification in the same direction for both binding groups. In comparison, we performed the same calculations with the Au top electrode (Fig. S19). Here, the peaks at −1 V and 0 V are located at approximately the same energies. However, at +1 V, the peak for mOPPy3 shifts inside the bias range compared to OPPy3, indicating that rectification in this case would occur in the opposite direction of the experiments and the Al top electrode.

We note that the choice of binding group has an impact; however, we argue that this effect, especially for the Al top electrode, has minimal influence on the overall results.

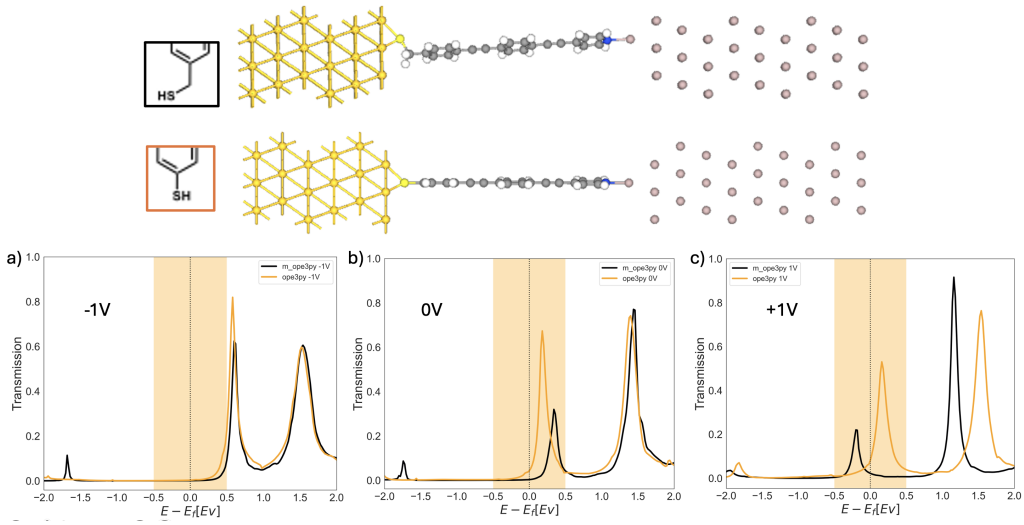

Figure S18: Comparison of mOPPy3 and OPPy3 with the Al top electrode. Top: Illustration of the two junctions. Bottom: transmisson of mOPPy3 (black) and OPPy3 (orange) at −1 V(a), 0 V(b) and +1 V(c).

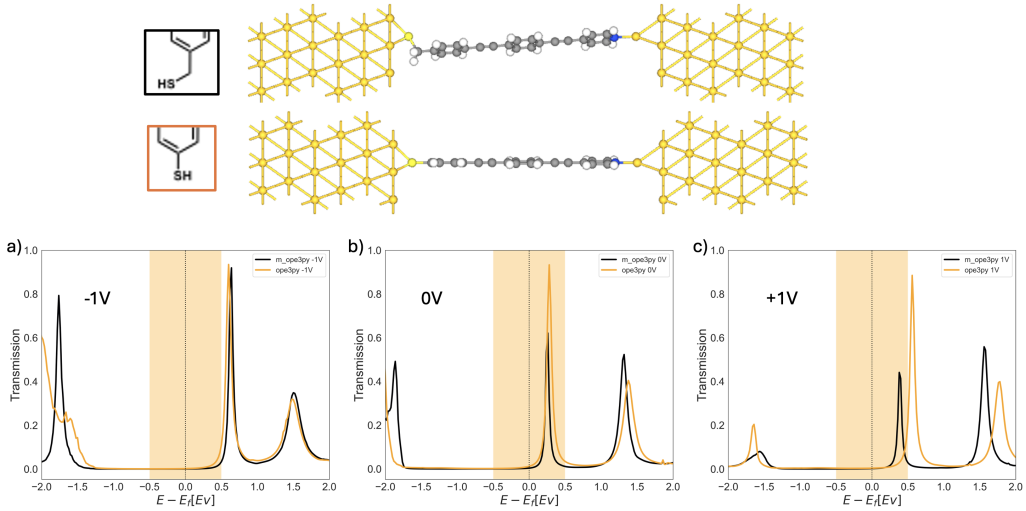

Figure S19: Comparison of mOPPy3 and OPPy3 with the Au top electrode. Top: Illustration of the two junctions. Bottom: transmisson of mOPPy3 (black) and OPPy3 (orange) at −1 V (a), 0 V (b) and +1 V (c).

S10 Calculation details

S10.1 Optimization, transmission and IV calculations

The calculations were conducted using Gaussian16 for gas phase optimization of the molecules and QuantumATK2022-S for transmission and IV and dipole calculations. All molecules were initially optimized in the gas phase, with S passivated by H, using the M062X functional and a 6-31+G(d,p) basis set with empirical dispersions (GD3).

The gas phase optimized molecule was placed at an FCC hollow site (with H removed from S) at a distance of 1.71 $\mathring{A}$ from the gold surface, resulting in a Au-S distance of 2.39Å.[ATK'171'SAu'dist, NAu'and'SAu'distance] from the Au electrode surface in an 3x3x2 Au-Al junction.

Both for the Au-molecule-Al and the Au-molecule-Au junction the an adatom was added to the right electrode at a distance of 2.3546 Å from the surface of the electrode corresponding to the Al-Al/Au-Au layer in the electrode. For the junction with Au-Al the adatom was positioned at 2.11 Å from the N. The distance between N and Al was chosen after optimization of an Al surface (with an adatom) and the molecule (with the S pasivated with H). For the Au-Au junction a similar optimization of the Au-N distance was carried out. The Au-N distance was found to be 1.99 after opimization.

All junction calculations were carried out with a Monkhorst-Pack grid of 4x4x134 with periodic boundary conditions. The transmission was calculated in a range from -3 to 3 in 301 steps with k-points set to 6x6. The transmission was computed in a range from -3 to 3 in 301 steps with k-points set to 4x4. The IV curves was calculated with the same seeting in a bias range from $-1\,\mathrm{V}$ to 1 V in steps of $0.11\,\mathrm{V}$. All calculations in ATK were calculated using GGA.PBE with double zeta polarization and grimmeDFTD3.

S10.2 Molecular orbtial and Dipole calculations

The molecular orbitals were calculated from the molecular junction at different bias chosing only the molecule in the junction. The choice of the HOMO and LUMO orbitals was based on the molecular energy spectrum.

For the dipole calcualtions, the molecules was added between two surfaces with S passivated with H and optimized in ATK using GGA.PBE with double zeta polarization and grimmeDFTD3 in three different fields, 0 V, 1 V or $-1\,\mathrm{V}$. After optimization the electron difference density was calculated for each molecule at each field. The electron difference density was then used for calculating the dipole moment following quantumATK – script available at ??.